Labor für Nuklearchemie
FH Aachen

FH AACHEN
UNIVERSITY OF APPLIED SCIENCES

The Structural-Chemical Performance of Aluminium and Chromium based UO_2 Advanced Technology Fuels

Masterarbeit

Studiengang Nuclear Applications

Focus Field Nuclear Chemistry

Fachbereich Chemie und Biotechnologie

FH Aachen - Campus Jülich

vorgelegt von

Pedro Foresti Jiménez

Matrikelnummer 3661240

Jülich, 10/ November 2025

Diese Arbeit wurde an der **FH Aachen** (in Kollaboration mit der **Forschungszentrum Jülich**) erstellt und wurde betreut von:

1. Prüfer: Prof. Dr. Christoph Langer

2. Prüfer: Dr. Gabriel Murphy

Eidesstattliche Erklärung

Die Arbeit ist von mir selbständig angefertigt und verfasst. Es sind keine anderen als die angegebenen Quellen oder Hilfsmittel verwendet worden.

(Datum, Ort)	(Pedro Foresti Jiménez)

Acknowledgements

This work has been performed with the means of the Forschungszentrum Jülich (FZJ), specifically the Institute of Fusion Energy and Nuclear Waste Management (IFN-2) in the Nuclear Waste Disposal Solid-State Chemistry group. Grateful for in-part funding support from Transient BMBF Project (02NUK088A). Special thanks to Prof. Dr. Dirk Bosbach and Prof. Dr. Giuseppe Modolo for the opportunity to do research at the FZJ, to my team leader and supervisor Dr. Gabriel Murphy and to the many colleagues at the IFN-2 who helped me: Dr. Martina Klinkenberg and Dr. Felix Brandt for the help with SEM and EBSD analysis; Dr. Philip Kegler for the help in pellet sintering and XRD measurements; Dr. Andrey Bukaemskiy and Mr. Daniil Shirokiy for the help in polishing and mechanical properties; Mr. Pascal Uhlemann for being my first contact on the institute, my desk neighbour and for the help with Rietveld refinements; Mr. Maximilian Henkes and Ms. Celina Erven for the help in the lab; Mr. Egor Ivashko, Mr. Kevin David Stucke and Ms. Mara McCleary for the partnership and company. I thank the FH Aachen for the opportunity to take part in the Master Nuclear Applications programme, providing me with knowledge of nuclear chemistry and technology which were essential for the work in the master thesis, specifically I thank my supervisor at the FH Aachen, Prof. Dr. phil. nat. Christoph Langer for the all the help and support whenever I needed it; Prof. Dr. rer. nat. Elisabeth Paulßen and Mr. Felix Schneider for the guidance in the field of Nuclear Chemistry; and all other lecturers at the FH Aachen for the excellent courses. I thank Ms. Ana Beatriz Manhães for the warm welcome to the master programme and Germany, Ms. Alina Kaulen, Ms. Freya Maybach, Mr. Marc Wild, Mr. Marcos Bazzoni and Ms. Sophia Krottenthaler for the partnership during the master.

Abstract

The want for carbon neutral sources and the pressure of historical nuclear accidents leads to a search for safer and more efficient nuclear fuels. Advanced Technology Fuels aim to achieve this with the use of doped UO_2 to achieve higher fission gas retention and improved pellet-cladding interaction, however, the knowledge about their behaviour pre- and post-irradiation is still not fully understood, particularly in the case of Al-doping. Therefore, this Master Thesis is devoted to understanding the chemical, microstructural and mechanical properties of Cr-, Al/Cr- and Al-doped UO_2 model materials to support their use as nuclear fuels but also provide potential insight into their behaviour as spent nuclear fuel materials. In this study, a synthesis method for these materials using co-precipitation and high temperature sintering with doping amounts of 500, 1000, 1500 and 2000 molar ppm allowing for their comparison is developed and their microstructural, mechanical and chemical properties are analysed. Cr-, Al/Cr- and Al-doped UO_2 ceramics with the doping amounts from 0 to 2000 molar ppm were produced and all found to be single phase consistent with the UO_2 $Fm\bar{3}m$ structure via powder x-ray diffraction measurements. Rietveld analysis was used to quantify the incorporation of dopant cations within the UO_2 lattice matrix. The analysis unveiled lattice contraction consistent with the relative size of the dopant cations Cr^{3+} and Al^{3+} in which the incorporation is correlated to grain growth. To examine this improved grain growth, electron microscopy via scanning electron microscopy with backscattered electrons and electron backscatter diffraction measurements were performed. These results indicated variable grain growth that is dependent upon the position of the pellets and the dopant used. In particular, it was observed for 2000 ppm Al- and Al/Cr-doped UO_2 a reduced grain size at the rim of the pellets. This reduced grain size at the rim is attributed to the higher volatility and lower solubility of Al_2O_3 compared to Cr_2O_3. The microhardness and fracture toughness of these materials were determined through Vicker's indentation combined with image analysis of the indent and cracks. It was found that Al-doped materials exhibited consistent microhardness and relatively higher fracture toughness than Al/Cr doped materials. In contrast Cr-doped materials presented variable fracture toughness and microhardness due to the materials not being at complete dopant saturation, unlike the Al/Cr and Al. Consequently, the mechanical properties highlight the importance of considering solubility of dopants and their relative amounts for addition in determining mechanical properties. Overall, the thesis provides key novel insights into the preparation, chemical behaviour, microstructural performance and mechanical stability of Cr-, Al/Cr- and Al-doped UO_2 model materials relevant to advanced next generation fresh and spent nuclear fuels.

Index

Abbreviations

ADOPT™	Advanced Doped Pellet Technology (Westinghouse, USA)
ADU	Ammonium Diuranate
ATF	Advanced Technology Fuels
AUC	Ammonium Uranyl Carbonate
AVR Jülich	Arbeitsgemeinschaft Versuchsreaktor Jülich
BSE	Backscattered Electrons
COCA	CObroyage CAdarache
EBSD	Electron Backscatter Diffraction
EDS	Energy Dispersive X-ray Spectroscopy
FGR	Fission Gas Release
FZJ	Forschungszentrum Jülich
GWd/t_{HM}	Gigawatt-day per ton of Heavy Metal
HALEU	High Assay Low-Enriched Uranium
HF	Hydrogen Fluoride
HFW	Horizontal Field Width
JAEA	Japan Atomic Energy Agency
LSC	Liquid Scintillation Counter
MIMAS	Micronized MASter blend
MOX fuel	Mixed Oxide fuels of UO_2 and PuO_2
PCI	Pellet-Cladding Interaction
PUREX	Plutonium-Uranium Recovery by Extraction
P-XRD	Powder X-Ray Diffraction
RBMK	Reaktor Bolshoy Moshchnosti Kanalnyy
SE	Secondary Electrons
SEM	Scanning Electron Microscopy
SNF	Spent Nuclear Fuel
TD	Theoretical Density
TRISO	Tristructural Isotropic fuel
UO_2	Uranium Dioxide

1. Introduction

1.1. Overview

The accelerated transition towards carbon neutrality, the recent challenges in energy-security, with the demand for reliable domestic base load sources has culminated in a perfect storm of energy technology uncertainty in which through this mist, modern nuclear energy technology has recently emerged as an attractive solution. Nuclear energy provides stable baseline production of power where it is capable of substituting fossil fuels in providing the baseload electricity to the grid. Moreover, as fossil fuel-based electricity generation is phased out, nuclear power plants have had modernizations to improve their manoeuvrability allowing them to more flexibly operate absorbing the innate variance of renewable power generation. This is especially true for countries with a large share of nuclear power or high intermittent renewables [1, 2].

The history of nuclear power generation is intimately related to the development of nuclear power for military purposes. The first artificial nuclear reactor, the Chicago Pile-1, was developed in the Manhattan Project during World War II with the objective of developing nuclear weapons and, following it, the B Reactor was the first large scale reactor for plutonium production for nuclear weapons [3]. The first full-scale nuclear reactor for electricity production exclusively for civilian purposes, the Shippingport Atomic Power Station, had its first core coming from a cancelled nuclear-powered aircraft carrier project. The Obninsk Nuclear Power Plant in Russia provided electricity to the grid, but its main purpose was to carry out nuclear experiments. The United Kingdom Calder Hall nuclear power station's main purpose was production of plutonium for nuclear weapons.

However, military focused nuclear reactors have different goals than civilian nuclear power plants, whose goals are safety, stable output and economic competitiveness. For plutonium production, reactors operate at low burnups to maximize the amount of fissile plutonium obtained and fuel must be replaced frequently. This motivates designs like the Reaktor Bolshoy Moshchnosti Kanalnyy (RBMK) Soviet Union reactor which can be refuelled without shutdown [4]. For nuclear propulsion the reactor's output must be quickly adaptable to the needs of the warship, requiring fast ramp up. To overcome the xenon poisoning transient in these cases, a higher reserve of reactivity is needed – leading to higher enrichments [5].

The blackout in May 2025 that affected most of Spain, Portugal and the south of France highlighted the importance of energy security. Diversifying the sources of energy available, reducing the dependence on energy from neighbouring countries and investing in a stronger grid infrastructure are ways to mitigate the risk of a blackout. Nuclear

energy can be a national source of stable energy [6]. Presently, nuclear energy represents around 9% of the world's electricity, the biggest producers are the USA, China, France, Russia and

South Korea [7]. New nuclear energy projects are being carried out for the most part in China, India, Turkey, South Korea and Russia [8, 9].

The Fukushima Daiichi accident had a strong impact on the decision-making regarding nuclear energy. Germany accelerated their planned phase out and Switzerland and Belgium decided to phase out nuclear power, though Belgium in 2025 reversed their decision [10-12]. France initially declared they would reduce nuclear usage, but ultimately maintained their energy strategy [13]. China continued developing nuclear power [14]. This accident also brought to light the need for safer nuclear fuel systems. The demand for improvement of the safety and security of nuclear power plants brought by the Fukushima Accident was manifold. A more thorough safety assessment, considering extreme natural hazards; a stronger peer review process; a prompt review of emergency preparedness and response plans; the need for strong independent national regulatory bodies and operating organizations with a focus on nuclear safety; a review of safety standards; and more effective communication and transparency [15].

The accident brought to focus the need for improvement of key fuel characteristics in normal operation and accident scenarios: the reduction of fuel wash-out, which is when fragments of fuel pellets or fuel grains are carried by the cooling water in the case of rod failure leading to an escalation of the primary coolant activity [16]; reduction of fission gas release (FGR), gaseous fission products diffuse through the fuel and escape it, leading to lower thermal conductivity and increased pressure in the rods [17]; finally the improvement of pellet-cladding interaction, which is the interaction between the fuel pellet and the cladding which can happen mechanically, in power ramp scenarios or through stress corrosion cracking due to the presence of some fission products like iodine [18].

On the other hand, improvements to fuel efficiency, leading to better economics, are also a focus of research. Here higher operating temperatures, leading to better thermal efficiency and higher burn-up, which is a measure of how much energy is extracted from a given mass of nuclear fuel usually given in units of gigawatt-days per ton of heavy metal (GWd/t_{HM}), leading to a longer time between fuel exchange are the goals. Another goal is the reduction of spent nuclear fuel (SNF) generated, which can be achieved using high assay low-enriched uranium (HALEU) to achieve higher burnup on fuels.

1.2. Current Generation Fuel and Spent Fuel

1.2.1. Uranium Dioxide – UO_2

Most of the world's nuclear power reactors today use fuels based on uranium dioxide (UO_2). It is a black crystalline ceramic compound that is stable under high temperature conditions, with a high melting point of 2865°C and extremely low solubility in water and.

UO_2 has a cubic fluorite structure in the space group $Fm\bar{3}m$ which is shown in Figure 1. It has lower thermal conductivity than uranium metal, uranium nitride and carbide as well as most uranium alloys, which can lead to localized overheating in the pellets and poor thermal transfer to heat exchanges *in operando*. The fabrication of UO_2 pellets is a well-known process, done on a large scale and already licensed by many nuclear authorities [19, 20].

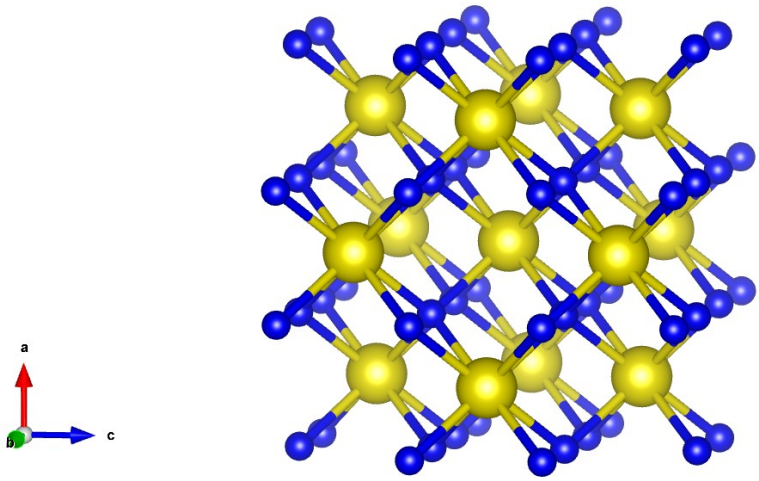

Figure 1 – Structural representation of UO_2 in its fluorite cubic structure with space group $Fm\bar{3}m$, where each uranium atom (yellow) is surrounded by 8 oxygen atoms (blue) [21].

UO_2 is produced in industry after the milling, conversion and enrichment steps of the nuclear fuel cycle, producing uranium hexafluoride UF_6, which is illustrated in Figure 2.

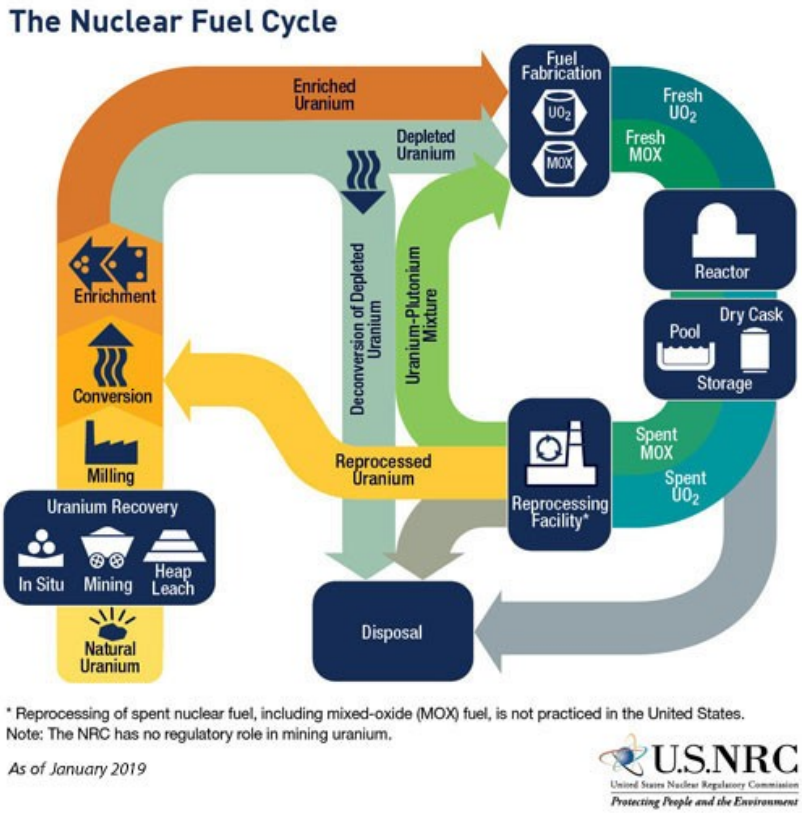

Figure 2 – Flow diagram of the nuclear fuel cycle including reprocessing of SNF [22].

The conversion of UF_6 into UO_2 can be carried out in a few different ways:

- Ammonium Uranyl Carbonate (AUC) wet process: UF_6 is first hydrolysed in water to UO_2F_2 then the solution pH is neutralized with ammonia gas and ammonium diuranate precipitates. This suspension is then heated to 40°C and 7 mols of ammonium carbonate per mol of uranium are added. The carbonate dissolves the ammonium diuranate through complex formation and then precipitates as the complex: $(NH_4)_4UO_2(CO_3)_3$, ammonium uranyl carbonate. The solids are washed with carbonate water to reduce the fluoride compounds content. The precipitate is then calcinated, then pyrohydrolysed at 500°C with steam to remove fluoride compounds and finally reduced to UO_2 using hydrogen [23].
- Ammonium Diuranate (ADU) wet process: UF_6 diluted with nitrogen gas is fed into a tank with deionized water together and a flow of ammonia gas. The UF_6 hydrolyses and then precipitates according to equations (1) and (2).

$$UF_6 + 2H_2O \rightarrow UO_2F_2 + 4HF \quad (1)$$

$$2UO_2F_2 + 8HF + 14NH_4OH \rightarrow (NH_4)_2U_2O_7 + 11H_2O + 12NH_4F \quad (2)$$

The suspension produced is filtered and washed with ammonium hydroxide to reduce the fluoride content. The solids are then introduced into a furnace with a nitrogen atmosphere and heated up. When the solids are dry, the nitrogen supply is turned off

and a mixture of ammonia and steam is introduced at 500-800°C. The steam pyrohydrolytically decomposes the fluoride compounds present while the ammonia reduces the intermediate U_3O_8 into UO_2 [23]. Direct UF_6 reduction dry process: In this process, UF_6 is first converted to uranyl fluoride by hydrolysis with steam. Then the UO_2F_2 is converted to UO_2 using a 50:50 mixture of steam and hydrogen [24]. After production, the UO_2 powder is ground, and an organic binder can be added. It is then pressed at 600-700 MPa into "green" pellets with a diameter of 10mm with a theoretical density (TD) around 50-60%. These pellets are then sintered in controlled oxygen potential conditions at around 1700°C for 4 hours to obtain UO_{2+x} with a slight hyperstoichiometry achieving a final TD around 95-98% [25-27].

SNF after a typical electricity production cycle in a nuclear power plant reaches a burn-up around 30-45 GWd/t_{HM}. Although a lot of energy is generated, the chemical composition of the fuel is not greatly modified, 95% of the uranium atoms are still present in spent fuel, with a reduced portion of the fissile ^{235}U to about 0.8%, some of the ^{238}U undergoing neutron capture forming plutonium isotopes and higher actinides, and some ^{236}U formed through neutron capture of ^{235}U. This process is graphically illustrated in Figure 3. A great deal of chemical complexity is brought about by the formed fission products which include a range of elements with mass number from 90 to 100 and from 130 to 150 and the products of their decay. Figure 4 provides this distribution arising from the fission of ^{235}U [28]. These fission products eventually decay into stable isotopes, some of the most important ones when considering interim disposal are ^{90}Sr and ^{137}Cs which have half-lives of around 30 years.

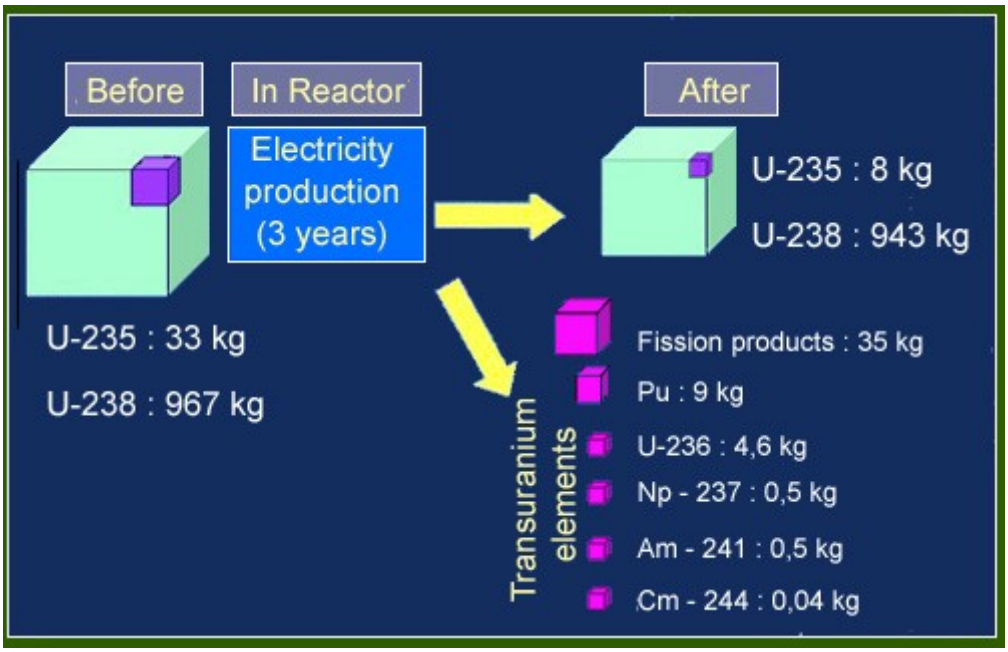

Figure 3 – Composition of SNF, based on 3.3% enriched UO_2, after 3 years of operation in a pressurized water reactor. A lot of different radionuclides are produced from the fission reactions, further decay and neutron capture reactions, however 95% of the fuel is still uranium [29].

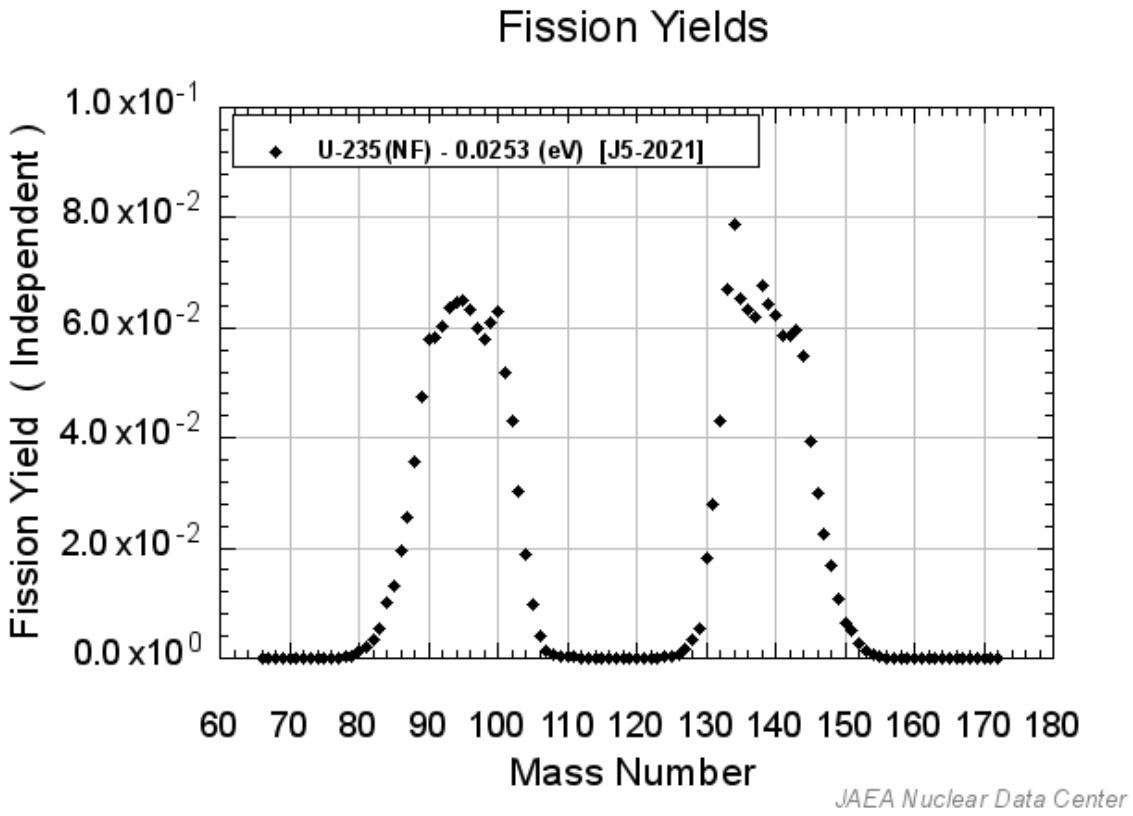

Figure 4 – Fission yield of the ^{235}U fission by thermal neutrons, the plot and data are derived from the JAEA Nuclear Data centre [28].

1.2.2. Mixed Oxide (MOX) Nuclear Fuel

In SNF, higher actinides are present due to neutron capture reaction. One important reaction that occurs is the neutron capture reaction on ^{238}U, followed by two successive beta decays, into ^{239}Pu.

$$^{238}U + n \rightarrow {}^{239}U \xrightarrow{\beta^-} {}^{239}Np \xrightarrow{\beta^-} {}^{239}Pu$$

This isotope of plutonium is of special interest as it is fissile. A reactor using 3% ^{235}U and 97% ^{238}U will contain after one cycle of operation around 1% ^{239}Pu and 1% ^{235}U [30]. Uranium and plutonium can be chemically separated from the spent fuel and then be used to produce mixed oxide fuel (MOX fuel), usually by mixing plutonium with natural, reprocessed or depleted uranium. This process is illustrated in Figure 2. Separating these radionuclides from spent fuel reduces the amount, the radiotoxicity and the lifetime of high-level nuclear waste. Moreover, this fuel can directly substitute the normal enriched UO_2 fuel, decreasing the need for mining, processing and enrichment of uranium.

The processing of MOX has often been achieved at the industry scale using methods including COCA, which stands for CObroyage CAdarache, and particularly MIMAS, which stands for Micronized MASter blend processes. MIMAS MOX fuel is produced by diluting a primary PuO_2 and UO_2 mixture (master blend) with UO_2 to reach the desired plutonium content, this leads to heterogeneity in the fuel, due to the low diffusivity of plutonium at sintering conditions, with plutonium rich regions near the concentration of the master blend. Although the fuel achieves an average burn-up of around 40 GWd/t_{HM}, localized high burn-up areas are formed in regions with a high concentration of plutonium, reaching 60-120 GWd/t_{HM} [31, 32]. Another process called COCA uses direct mixing by grinding UO_2 and PuO_2 powders together. This process achieves higher homogeneity [33]. The recycling of spent fuel and production of MOX in Europe is done by Orano, at their site at La Hague. MOX fuel has also not been commonly used outside of Europe (Belgium, Germany, France and Russia) and Japan. The United States have used plutonium fuel from dismantling nuclear weapons, but not from reprocessed fuel. Reprocessing spent fuel is intimately linked with nuclear weapons proliferation, so that technology is not widespread in Non-Proliferation Treaty countries.

The spent fuel generated from reactors operating with MOX is quite different, while in normal UO_2 fuel the fission events are more concentrated on the high burn-up rim, for MOX fission happens mostly in the concentrated plutonium particles, leaving the surface of the fuel pellet mostly unaffected. Another difference is that MOX fuel is more susceptible to low temperature oxidation and the formation of water soluble U(VI) species increases leaching [34].

1.3. Next Generation Fuels

More efficient nuclear fuels, reaching higher burn-ups, have become an attractive option following the contemporary difficulty in finding socially acceptable final disposal sites for nuclear fuel [35]. Higher burn-up fuel means more energy is extracted from the same starting amount of uranium, which means less waste generated both from the front end in mining, conversion, enrichment and fuel fabrication as well as on the back end with fuel storage and disposal. Competition with other carbon-free energy sources, like photovoltaic solar panels and wind turbines, motivates the nuclear industry sector to seek economic competitiveness.

1.3.1. Metallic and Intermetallic Fuels

The inclusion of nuclear reactors to power ships is motivated by the increased time before refuelling, in the case of military ships nuclear reactors add flexibility and stealth. Compared to nuclear power plants, naval propulsion reactors require more flexible operation, going through power cycles following the demand of the ship, and a sturdier construction considering the ship's movement and collision protection. The fuel of these reactors utilizes highly enriched uranium (93-97%) zirconium metal alloy with boron as burnable poison, in order to have a small size, a long core lifetime (in most cases the fuel lifetime is operational lifetime of the ship) and enough reactivity to offset the xenon poisoning reactor dead time [5, 36]. Research reactors also utilize fuels with high enrichment, though not as high as in military applications. To achieve the high neutron fluxes with lower enrichment and small sizes, high density materials like uranium silicide, U_2Si_3, and uranium alloys like UMo are used. They generally operate at lower temperatures since their goal is experiments, production of radioisotopes, education, materials testing and analysis.

1.3.2. TRISO

Tristructural isotropic (TRISO) fuel particles have been considered for the use in nuclear reactors with some known applications with the goal of high coolant temperatures or high burn-up performance. The centre of the particle contains the nuclear fuel, typically an oxide, carbide or oxycarbide of uranium, plutonium, thorium or other higher actinides. Then a layer of porous carbon to retain the recoiling fission fragments, fission gases and dimensional changes of the fuel. Next is a layer of pyrolytic carbon, followed by a layer of silicon carbide and finally another layer of pyrolytic carbon, Figure 5. The silicon carbide acts as the pressure vessel of the particle, resisting the pressure build up and being a diffusion barrier for fission products. The pyrolytic carbon are protective layers protecting the fuel kernel during the silicon carbide deposition process and protecting the silicon carbide during normal reactor operation [37]. This type of fuel was developed and tested

at the AVR Jülich reactor which operated from 1967 to 1988 at the Jülich Forschungszentrum GmbH, Germany [38].

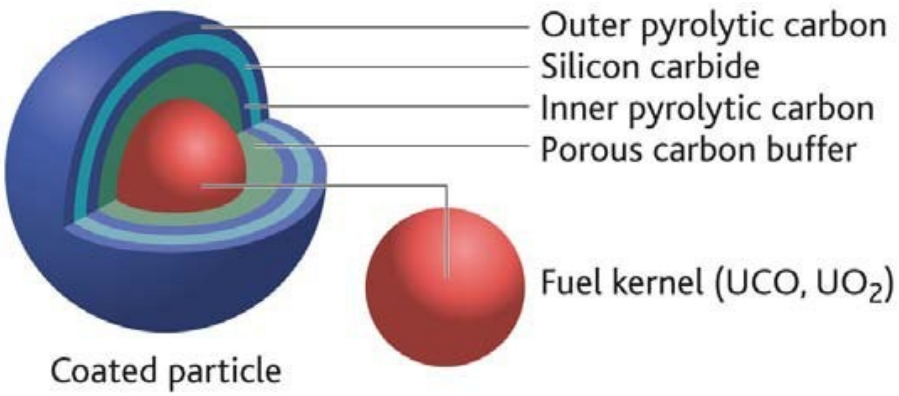

Figure 5 – Illustration of a TRISO particle [39].

1.3.3. Uranium Nitride

In the context of development of Generation IV nuclear reactors, new fuel types are proposed to improve the performance, safety and non-proliferation of fuels. One of the points for improvement for UO_2 is its low thermal conductivity. Uranium nitride fuels have been the subject of research, due to their higher thermal conductivity and a higher fissile density [40-42]. It also has good stability, is compatible with the PUREX reprocessing process and could achieve longer cycle times. However, the production of uranium nitride fuels is challenging: it is complicated by the pyrophoricity of the powder; the pellets are susceptible to oxidation and the need for highly enriched ^{15}N for its synthesis reaction due to the $^{14}N(n,p)^{14}C$ reaction which would otherwise increase the activity in spent fuel, requiring isotope separation and a stoichiometric addition process [43, 44].

Current research on the improvement of nuclear fuels can be divided into two branches: long-term development of entirely new fuel concepts to be applied in new reactor projects; and middle to short-term improvements on fuel types already in use, with a goal of faster licensing times and use on existing reactors.

Long-term development for new reactors includes fuels such as uranium nitride and uranium silicide which have higher fissile density and improved thermal conductivity. However, these concepts are still in earlier stages of research and have a long road until they can be licensed as commercial fuels and used in nuclear power plants for large scale electricity production.

1.3.4. Advanced Technology Nuclear Fuels

On the other hand, the development of fuel in the short-term focuses on minor changes and improvements to the fuels of current reactors, since the reactor configuration is

highly dependent on the type of fuel used. This makes them applicable to existing reactors, uses most of the same fuel fabrication installations which are already licensed and operating and aims to follow a more streamlined licensing process. Advanced Technology Fuels (ATF) aim to improve fuel safety and economics while still being applicable to existing nuclear reactors. ATF fuels comprise modifications of the currently most used UO_2-based fuel by co-sintering of small amounts of other materials, offering improved FGR, better plasticity and increased pellet density, Figure 6 [45].

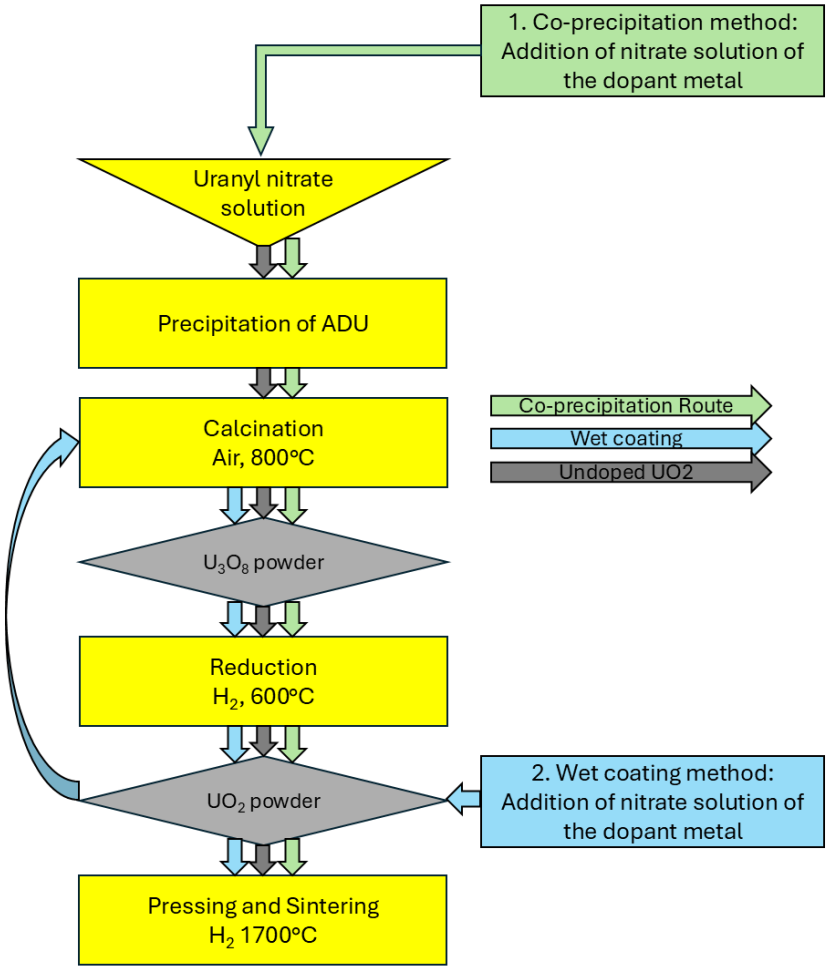

Figure 6 - Flow chart of the synthesis route to produce pure and doped UO_2 pellets. The commonly used process in industry is the wet coating method. In this work, the co-precipitation method is used [46].

1.4. Fission gas retention and large grain fuel

The release of fission gases from the fuel pellet to the cladding plenum is one of the key limitations of UO_2 fuels at high burnup and in accident conditions. The fission of ^{235}U produces gaseous fission products, such as the noble gases Krypton and Xenon which are always in gaseous form; Iodine and Bromine which can be gases when not incorporated into caesium salts; and Rubidium and Caesium which are only gases above 2150 K [47].

These gases are produced inside the fuel pellet, diffuse through the crystalline matrix to grain boundaries or pores, nucleate bubbles and, when a pathway of open porosity is

created, escape to the rod's plenum. The build-up of fission gases in the fuel rods increases the total pressure inside of them and dilutes the helium gas filling reducing the thermal conductivity. This in turn increases the temperature at the centre of the fuel pellet, triggering further gas release. Nonetheless, fuel rods are designed to withstand these effects over their lifetime in the reactor core [17]. Fuel pellets do not undergo fission at the same rate throughout their whole volume. Since thermal neutrons come from outside the fuel rod, the rim of the pellets experiences a higher neutron flux which leads to more fission events. At the same time, this region also has the lowest temperature due to being closer to the coolant. These effects combine to produce a region with high burnup, high defects and low thermal annealing of defects [48].

In the context of ATFs FGR is a critical factor, as the buildup of pressure in fuel rods in higher burnup and accident conditions is increased. The addition of dopants, including Cr, Al and Si, leads to an improved performance of the fuel due to increased grain sizes, as this creates a longer mean path of diffusion for fission gases to reach grain boundaries, Figure 7. Other advantages of these doped fuels are the increased plasticity, which gives better Pellet-Cladding Interaction (PCI) margins and increased density of the fuel.

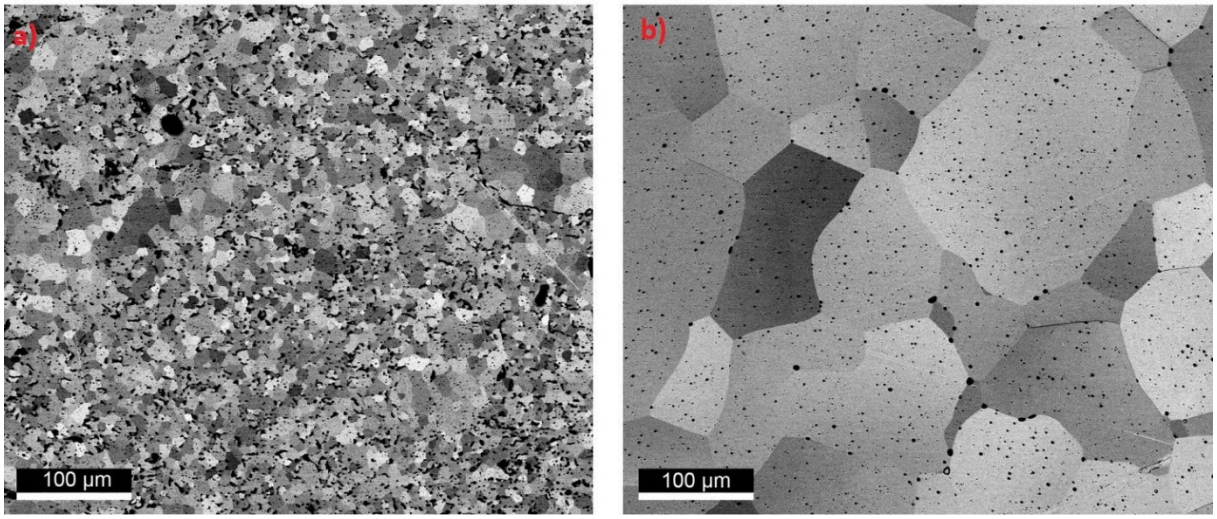

Figure 7 – Scanning Electron Microscopy of UO_2 fuel showing the difference in grain size between undoped (a) and 3500 ppm Cr-doped (b) UO_2 fuel, leading to an increased mean path of diffusion [49].

In industry, there are two main fuel vendors responsible for ATF doped fuel variants. The Framatome's PROtect blend is based on Cr doping whereas Westinghouse's ADOPT™ advanced fuels uses a eutectic mix of Al/Cr. In both cases, with the small amounts of Cr_2O_3 and Al_2O_3 added as dopants, the fuel is conferred a slightly higher density, larger average grains and better mechanical properties. These characteristics enable higher burnups, lower fission gas release, higher thermal stability, reduced pellet-cladding interaction and improved corrosion resistance [50]. These fuels have been licensed to work with different amounts of Al/Cr doping, the final amounts are held in confidence by the vendors [51].

These two fuels have already been used in reactors in the United States and in Europe and are going through licensing procedures for the fuel combined with new cladding solutions. Notable milestones of their development include Westinghouse's first batch production of higher enriched pellets and Framatome's first full-length rod operation at a high burnup of 60 GWd/t_{HM} [52, 53].

1.5. Current state

Research on modifications of UO_2 date back to the start of nuclear fuel development itself in the 1960s [54, 55]. The development of doped fuel to improve operational margins as well as mitigate accident consequences dates to before 1999 [56]. However, the Fukushima accident accelerated the timeline of implementation of these fuels, with government programs giving priority to its development [57].

Grain growth in UO_2 occurs during sintering due to enhanced ion diffusion through the grain boundary. The main variables for sintering processes are the temperature and oxygen potential (μ_{O2}). The equilibrium between the dopant ions dissolved into the main UO_2 matrix and their precipitates as eutectic phases is thought to contribute to the enhanced grain growth via formation of uranium vacancy defects that diffuse across grain boundaries and lead to grain growth [58].

While there has been a focus on understanding Cr-doped UO_2 fuel both looking at the application properties (density, fission gas diffusion, mechanical properties) and at the basic chemistry involved, the same cannot be said for Al and Al/Cr doped fuels. Moreover, while most of the early research has been focused on developing fuels, not as much focus has been given to understanding them as spent fuels in intermediate deposit and final repository conditions.

1.6. Chemical and Nuclear Design Considerations

Sintering conditions, temperature, time and oxygen potential are key factors in the resulting UO_2 pellet. Considering the Ellingham diagram of UO_2 shown in Figure 8, which shows the Gibbs free energy of formation of metal oxides (which is related to the oxygen partial pressure) as a function of temperature, the aim is to produce near stoichiometric UO_{2+x} with a slight hyperstoichiometry to improve sintering and density. With chromium doping, a slightly more oxidizing condition is used to improve grain growth and its incorporation [46]. These dopants have no function in the final fuel, on the contrary, their addition introduces neutron absorbers and dilutes the uranium, so their addition must be optimized for the maximum benefit of grain growth with the least addition of dopant. A maximum for the grain size as a function of initial Cr_2O_3 addition can be observed at around 700 wt. ppm and at 2500 wt. ppm in Figure 9 [59]. From testing of commercially used fuels, the doping amounts have been shown to be between 500 to 1600 ppm [60].

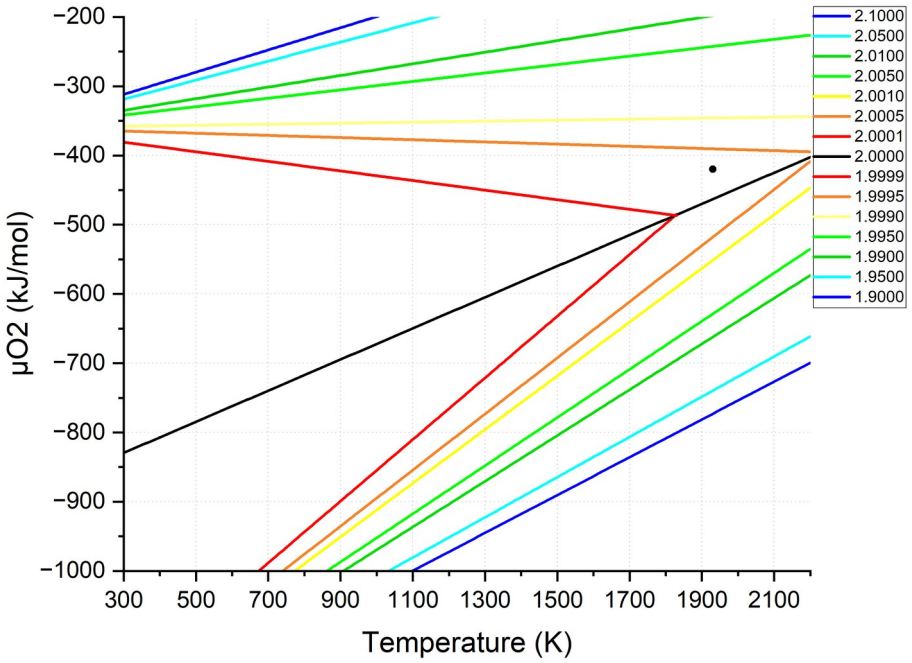

Figure 8 - The Ellingham diagram for UO_2 highlighting the conditions used to synthesize the material in the present investigation by the black circle, 1973 K (1700 °C) and μO2 of -420 kJ/mol [49].

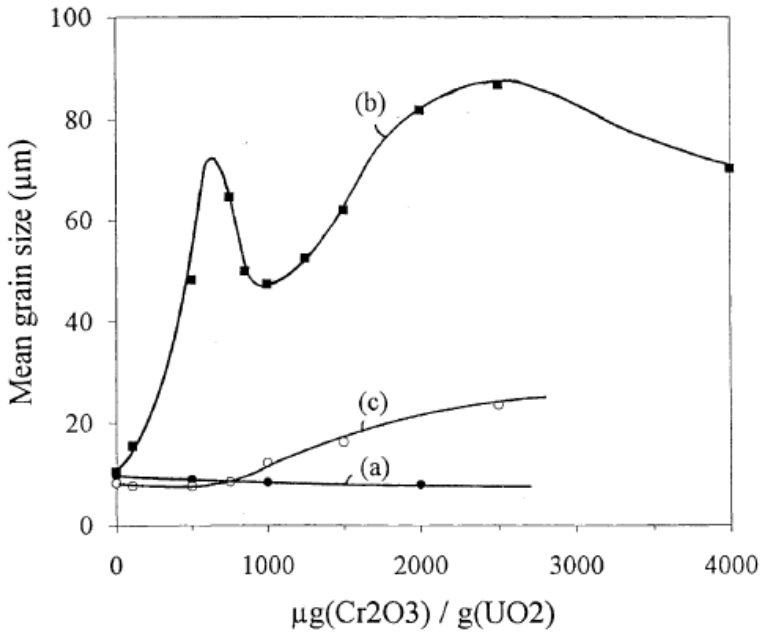

Figure 9 – Relationship between mean grain size and Cr_2O_3 content (after heat treatment). (a) H_2 + 0.05 vol.% H_2O, (b) H_2 + 1 vol.% H_2O and (c) H_2 + 5 vol.% H_2O [59].

In the case of Cr-doped UO_2, Cr is in equilibrium between UO_2 and other Cr phases at higher temperatures. In specific oxygen potential conditions and above certain temperatures a liquid CrO eutectic phase is present [61]. The eutectic composition is the ratio of two constituents where an eutectic transition is observed, that is, an homogeneous mixture of two phases has a single melting temperature which is lower than both of its constituent's and during the transition both phases coexist with the liquid

being formed [62]. The same behaviour is expected for aluminium doping with the possibility of a liquid eutectic phase, as shown in Figure 10. The solid solution of the dopant in the UO_2 matrix as well as the presence of a liquid phase at sintering temperatures provides a medium of contact between grains for uranium ions to solubilize and precipitate, reactivating the mechanism for grain growth, which depends on the mobility of ions [59].

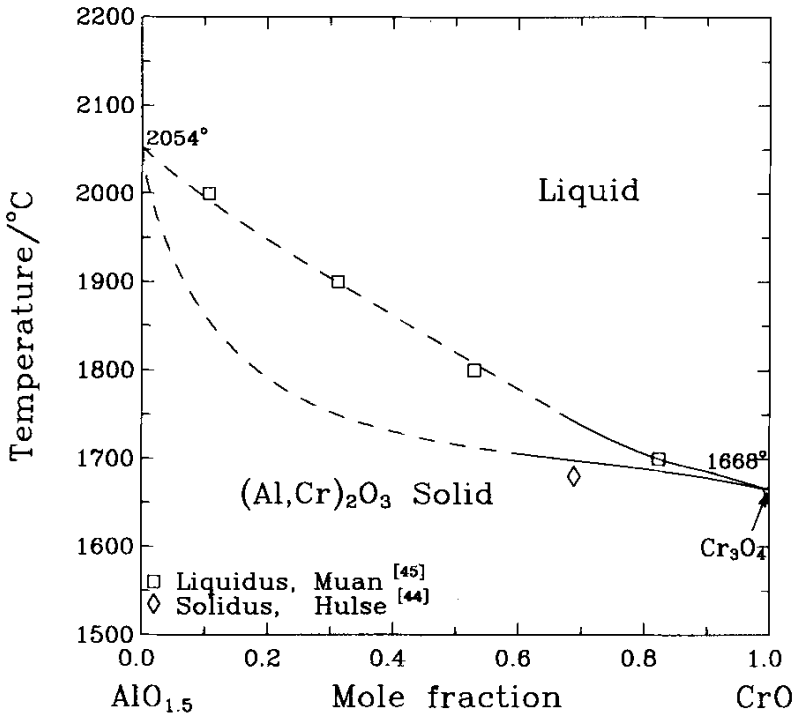

Figure 10 – Calculated CrO-Cr_2O_3-Al_2O_3 phase diagram in equilibrium with Cr [63].

The amount of dopant added to fuel should be enough for enhanced microstructural properties but limited and balanced due to the addition of poor and non-fissile neutron absorbing atoms. This means an addition of quantities slightly above the solubility limit, since the formation of a eutectic phase is desirable. The solubility of chromium at sintering temperatures of 1700 °C is about 700 wt. ppm of Cr_2O_3, which is equivalent to around 2480 molar ppm [59, 64]. The chemistry involved in these doped materials can be complex, with the formation of solid solutions in the UO_2 matrix introducing oxygen vacancy defects, a change of uranium oxidation number as well as secondary phases of metallic precipitates, oxides and eutectic liquids. Some dopants can be lost to volatilization during sintering, leading to void formation [65].

The use of aluminium as sole dopant in UO_2 has been seldom used, its effects alone provide a small increase of grain growth and its addition is quite limited by its low solubility of around 42 μgAl/gU, which is equivalent to around 420 molar ppm [66, 67]. A more interesting effect of aluminium as a dopant occurs in combination with chromium

with the possibility of forming a eutectic phase which aids grain growth, as shown in Figure 10. For this reason, it is used in part of industry made ADOPT™ nuclear fuels.

Other transition elements have been introduced as dopants. In Mn doped UO_2, the formation of a MnO secondary phase that is structurally similar to the main UO_2 phase can promote solubility of U^{+4} cations in this secondary phase, instead of the diffusion of these cations into neighbouring UO_2 crystals for grain growth [58]. Mn-doping also does not present a eutectic, which is an important factor in promoting enhanced grain growth. Vanadium doped UO_2 induces some grain growth, but to a lesser extent than chromium, moreover voids are formed in the structure due to the volatility of some vanadium oxides [68]. Systematically studying the structural and microstructural behaviour of aluminium and aluminium/chromium doped UO_2 when compared to chromium doping enables relative understanding to be obtained pertaining to the performance of these materials as fresh and SNF.

1.7. Overview and Project Objective

Considering the deployment of Cr-doped UO_2 and Al/Cr-doped UO_2 fuels in current power reactor units, it is pertinent to development model system materials that can replicate their structural and microstructural performance. This allows improved understanding for their behaviour within nuclear reactor environments and later as SNF for disposal. However, current literature has largely focused on the performance of Cr-doped UO_2 with some attention given to Al-doped UO_2, but there is extremely limited data available for the Al/Cr-doped UO_2 mixed varieties, despite their current deployment. Accordingly, this Thesis aims to bridge this gap between the 3 derived doped UO_2 forms by:

1) developing a method for the synthesis of Cr-doped UO_2, Al-doped UO_2 and Al/Cr-doped UO_2 ceramics yielding good quality materials allowing for comparison.

2) determining the dopant and structural-interaction chemistry of Al, Cr and Al/Cr with UO_2.

3) understanding the effect of specific dopants on microstructural performance.

4) elucidating the effects of the addition of these dopants on the mechanical properties of the pellets.

2. Material and Methods

2.1. Process Development

2.1.1. ADU Precipitation

The production of doped UO_2 pellets can be achieved in several different ways. In industry, doped UO_2 is generally produced via dry mixing of oxide powders before sintering. Other possible methods are the wet coating method, where a dopant nitrate solution is mixed to UO_2 powder before sintering and the co-precipitation method, where the dopant is added as a nitrate solution to the uranium nitrate at the start of the synthesis. Another very important factor in the synthesis is the control of oxygen potential during sintering, a slightly hyperstoichiometric UO_{2+x} yields better incorporation of the dopant and higher pellet densities [46]. However, near stoichiometric states are targeted for optimal neutronic properties for reactor usage.

In the present case, the synthesis of materials followed a co-precipitation route: dopants in the form of metal nitrates were added to a uranyl nitrate solution. This method has the advantage of achieving very good mixing of the dopant in the liquid phase, optimizes homogeneity of the final pellet product and being dust-free which is an advantage in nuclear applications. A further route established is that of "wet coating" involving the addition of a metal nitrate solution to a previously obtained UO_2 powder which is then subjected to the same thermal treatments [46].

2.1.2. Preparation of solutions

For the co-precipitation of doped ADU, a target final mass of 1.9 g of UO_2 per pellet sample was planned, so that the pellets would have around 1.5 g of UO_2, considering an 80% efficiency. Stock solutions of reagents used for the synthesis of all compounds were generated to ensure consistent source chemicals and additions.

A uranyl nitrate stock solution was prepared by adding 34.0517 g of $UO_2(NO_3)_2.6H_2O$ to a 50 mL volumetric flask, which was then filled with deionized water. The calculated concentration of the resulting solution was determined to be:

$$c_{UO_2(NO_3)_2} = \frac{34.0517\,g}{502.126\,\frac{g}{mol}\cdot 0.05\,L} = 1.356\,M \qquad (1)$$

An aluminium nitrate base solution was prepared by adding 0.1799 g of $Al(NO_3)_3.9H_2O$ from Merck to a 50 mL volumetric flask, which was then filled with deionized water. The calculated concentration of the resulting solution is:

$$c_{Al(NO_3)_3} = \frac{0.1799\,g}{375.129\,\frac{g}{mol}\cdot 0.05\,L} = 0.010\,M \quad (2)$$

A chromium nitrate stock solution was prepared by adding 0.2125 g of $Cr(NO_3)_3.9H_2O$ from Emsure to a 50 mL volumetric flask, which was then filled with deionized water. The calculated concentration of the resulting solution is:

$$c_{Cr(NO_3)_3} = \frac{0.2125\,g}{400.143\,\frac{g}{mol}\cdot 0.05\,L} = 0.011\,M \quad (3)$$

The effect of dopants is dependent on their concentration in the final product; to have a better comparison on the effect of different dopants, similar but controlled molar amounts of each dopant were used. However, in industry dopants are added according to mass ratios for simplicity of measurement and control. Samples were planned with 0 to 2000 molar ppm of dopant content in UO_2, with either pure Al-doping, a 50/50 split of Al/Cr-doping, or pure Cr-doping, Table 1.

Table 1 – Volumes of each base solution for the preparation of doped UO_2 samples.

Dopant	**Dopant (molar ppm)**	**Dopant (wt. ppm M_2O_3)**	**Dopant (wt. ppm M)**	**Volume $UO_2(NO_3)_2$ solution (mL)**	**Volume $Al(NO_3)_3$ solution (µL)**	**Volume $Cr(NO_3)_3$ solution (µL)**
Undoped	0	0	0	5.19	0	0
Al	500	94	50	5.19	367	0
Al	1000	189	100	5.18	734	0
Al	1500	284	150	5.18	1100	0
Al	2000	378	200	5.18	1465	0
Al/Cr	250/250	47/70	25/48	5.19	183	166
Al/Cr	500/500	94/141	50/96	5.18	367	331
Al/Cr	750/750	142/211	75/145	5.18	550	497
Al/Cr	1000/1000	189/282	100/193	5.18	734	662
Cr	500	141	109	5.19	0	331
Cr	1000	282	219	5.18	0	662
Cr	1500	423	328	5.18	0	994
Cr	2000	564	438	5.18	0	1325

Samples were prepared by adding the uranyl nitrate solution and the dopant solutions to 50 mL centrifuge vials. Then the vials were filled up to the 45 mL mark and 4.78 mL of a 25% ammonium hydroxide solution was added, a 300% stoichiometric excess to shift the chemical equilibrium and precipitate all the uranium as ammonium diuranate. The vials were closed, shaken well and left overnight.

The next day, the vials were centrifuged using a Thermo Heraeus Multifuge 3S-R for 20 min at 4000 rpm and cooled to 15 °C. After centrifuging, the supernatant liquid was discarded as waste. The solids were washed 3 times by adding around 10 mL of water, stirring with a spatula and centrifuging again. The process of ADU precipitation can be described by the equation (6):

$$2UO_2(NO_3)_2 + 6NH_3 + 3H_2O \rightarrow (NH_4)_2U_2O_7 + 4NH_4NO_3 \quad (4)$$

2.1.3. Drying and Calcination

After the washing steps, the solids were transferred to platinum crucibles, placed inside a crystallizing dish covered with a watch glass and placed inside a Thermo Heraeus T12 D-63450 drying oven set at 90 °C and left overnight.

After drying, the crucibles were transferred to the Carbolite CWF-1300 calcinating oven with heating up at a rate of 150 °C/h up to 800 °C, a dwell time of 8 h, followed by cooling down to room temperature at 150 °C/h. The crucibles were then removed from the oven, the U_3O_8 product was transferred to LSC vials.

2.1.4. Reduction, Pressing and Sintering

The first step after calcination was to grind the U_3O_8 samples, this was done by transferring the solids to an agate mortar and pestle and grinding the solids with acetone, to prevent the spread of contamination. The resulting powder was then transferred back to the LSC vials.

For the reduction of the U_3O_8 to UO_2, the powders were transferred to alumina crucibles and placed in a tube furnace (ENTECH ESTF 50-18-SP-VK, Ängelholm, Sweden), Figure 11. The reducing gas was a mixture of 4% H_2 in Argon with a flow rate of around 860 mL/min. The temperature program consisted of heating at a rate of 4 °C/min up to 600 °C, a dwell time of 5 h, followed by cooling down to room temperature at 6 °C/min.

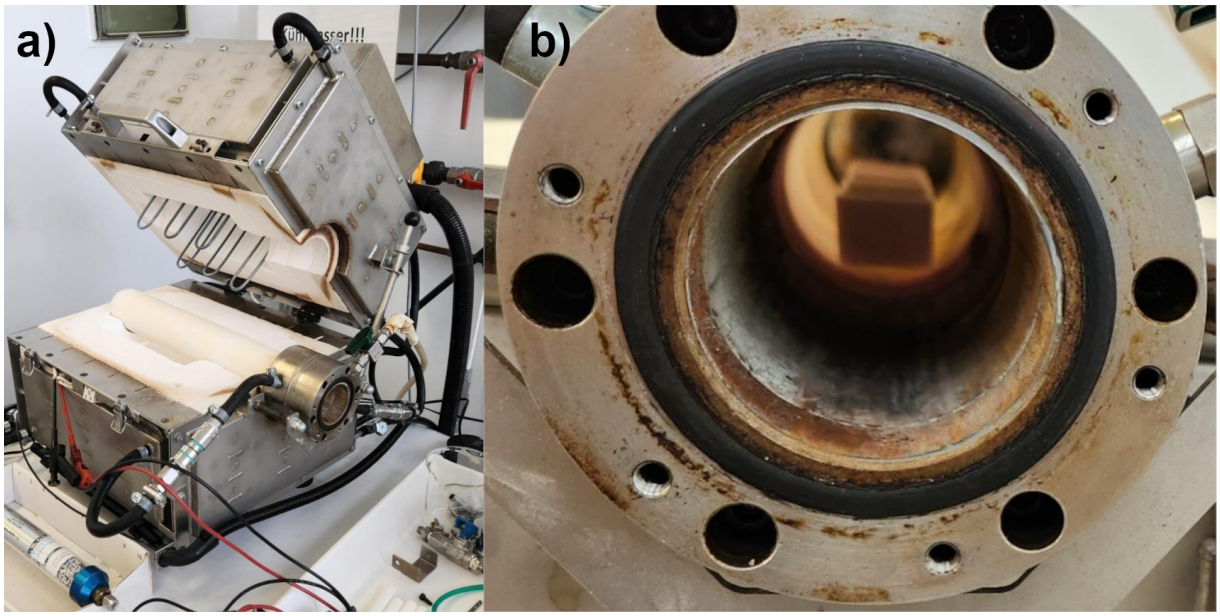

Figure 11 – a) tube furnace used for reduction of U_3O_8 and sintering of pellets with 6 heating elements and temperature measurement thermocouple; b) inside view of the tube with the alumina crucibles placed inside the furnace.

After reduction, each powder was ground up again and, for each of them, separated into two 1.5 mL Eppendorf vials, one containing around 1 g of powder and the second with the rest.

Each powder was then pressed into pellets, called "green pellets" as they have not yet been sintered. Pressing was done with a tungsten carbide piston of an uniaxial press (Hahn & Kolb, MP12, Stuttgart, Germany) without adding binder or lubricant, Figure 12, with 574 MPa pressing pressure for 7 seconds [27]. The green pellets' height and weight were measured after pressing, to calculate the green density.

$$\rho_g = \frac{m_g}{\left(\frac{\pi D^2 h}{4}\right)} \tag{5}$$

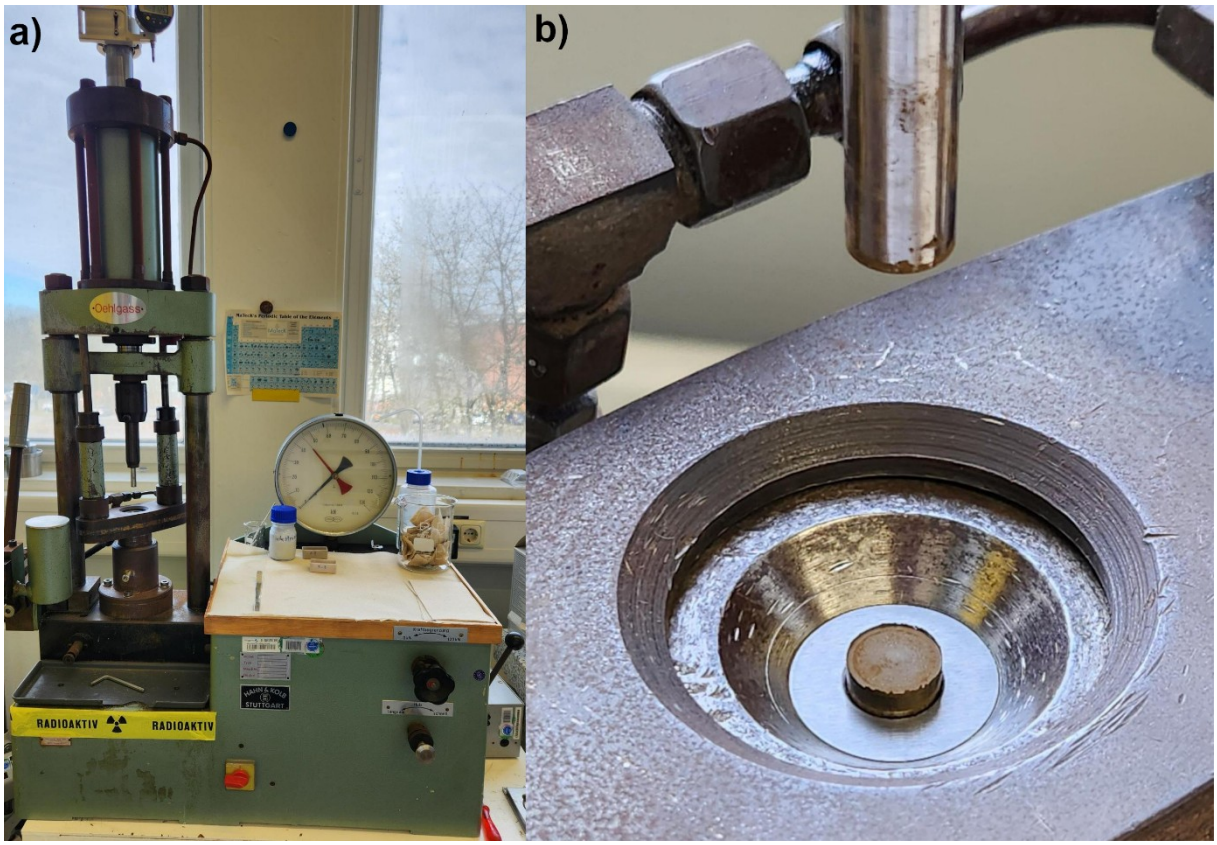

Figure 12 – a) uniaxial press with tungsten carbide piston – Hahn & Kolb, MP12, Stuttgart, Germany; b) green pellet obtained after the pressing procedure.

The obtained green pellets were transferred to alumina crucibles and sintered in the tube furnace (ENTECH ESTF 50-18-SP-VK, Ängelholm, Sweden). The atmosphere consisted of 4% H_2 in Ar (HYTEC) at 818 mL/min and 1% O_2 in Ar (Crystal) at 10.9 mL/min in order to achieve an ideal oxygen partial pressure for sintering of -420 kJ/mol. The temperature program consisted of heating at a rate of 4 °C/min to 800 °C, then heating at a rate of 6 °C/min to 1700 °C, a dwell time of 10 h, followed by cooling at 6 °C/min to room temperature.

The chemical thermal process of converting ADU to U_3O_8 and finally to UO_2 is provided below, in three steps, loss of ammonia and water (8), thermal reduction to U_3O_8 (9) and finally reduction with hydrogen to UO_2 (10).

$$(NH_4)_2U_2O_{7(s)} \xrightarrow{\Delta} 2UO_3 + 2NH_3 + H_2O \quad (6)$$

$$3UO_3 \xrightarrow{\Delta} U_3O_8 + 1/2O_2 \quad (7)$$

$$U_3O_8 + 2H_2 \xrightarrow{\Delta} 3UO_2 + 2H_2O \quad (8)$$

2.2. Structural Chemistry

The amount of dopant incorporated into the UO_2 matrix results in the occurrence of Cr^{+3} and an oxygen defect around it, regardless of Cr metal or Cr_2O_3 precipitates [49]. The

substitution of the uranium ion for the chromium ion, with a much smaller ionic radius, in the lattice structure should result in a contraction of the crystal lattice, following Vegard's Law [69]. The degree of lattice contraction is consequently a result of the ionic radius, and the amount of dopant present within the lattice. This means that precisely measuring the change in lattice parameter of UO_2 for each dopant addition provides a probe for its inclusion in the structure. Many factors can affect how much of the dopant ends up on the UO_2 structure: solubility limits, volatilization during sintering and method of addition. Accordingly, only listing the amount of dopant added at the start is not sufficient to understand their effects on the final pellet. Subsequently, for synthesized final pellet materials, X-ray powder diffraction (P-XRD) measurements were performed on samples to examine the effect of doping on the UO_2 matrix.

P-XRD is a scientific technique which uses the diffraction of X-rays over a range of angles of incidence on the crystalline materials to obtain information on their long-range structure. When these X-rays reach the material, the X-ray beam can be reflected off the surface or enter the crystal lattice and be diffracted by the crystal lattice, Figure 13. The X-rays can interfere constructively only when the path-length difference $2d\,sin\theta$ is equal to an integer multiple of the wavelength, producing a diffraction maximum according to Bragg's Law [70].

$$2d\,sin\theta = n\lambda \tag{9}$$

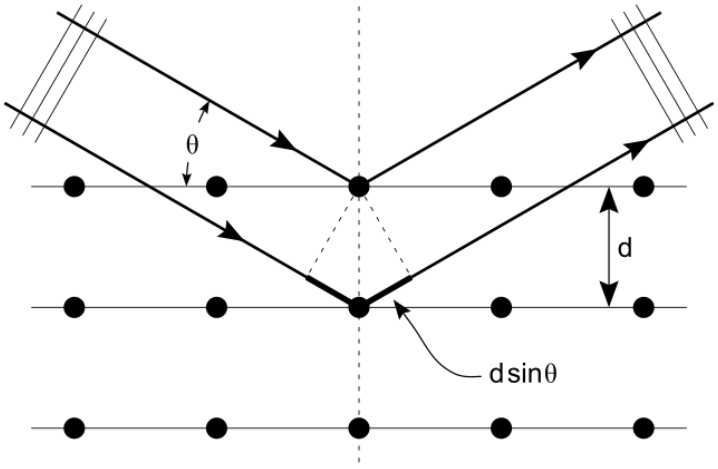

Figure 13 – Bragg diffraction on a cubic crystal lattice. Plane waves incident on a crystal lattice at angle θ are partially reflected by successive crystal planes of spacing d. The superposed reflected waves interfere constructively if the Bragg condition is fulfilled.

Specific to P-XRD, the sample in the form of powder contains crystals in every possible orientation, therefore each plane will be represented in the signal. Samples are often rotated during the measurement to guarantee this randomness. The scattered radiation collected on the detector produces solid diffraction rings around the beam. The angle between the beam and these rings is called the scattering angle and is denoted *2θ*. Data is presented as a diffractogram in which the intensity of the signal measured is plotted

against the scattering angle *2θ* or the length of the reciprocal lattice vector *q*. The latter variable has the advantage of being independent of the wavelength of the beam, making it easier to compare data.

$$q = \frac{4\pi}{\lambda} sin\theta \tag{10}$$

Analysis of the diffraction peaks can be used to determine the lattice parameters of a sample, as the position of the peaks is independent of atomic positions in the cell and is entirely determined by the size and shape of the unit cell. However, in the case of UO_2, the presence of overlapping $K\alpha_2$ peaks and of minor oxidized phases produced in the contact of the ground sample with air results in a more complex diffraction pattern that cannot be solved simply by peak indexing. To deconvolute the more complex diffractogram, the Rietveld Method is used [71, 72]. This method is a full pattern analysis technique, where a model theoretical diffraction pattern is compared to observed data and a least squares approach is used to minimize the difference between them by adjusting the model's parameters. With a good fit of the model on the observed data reliable information about the material can be extracted.

The change in the crystallographic properties, specially the lattice parameter, of the UO_2 matrix was determined through the analysis of the powder x-ray diffraction data using the Rietveld method in the program GSAS-II [73]. Since the dopants are added in parts per million amounts, their effect on the UO_2 lattice parameter can be described as a weighted mean of the lattice parameters of the two constituents in solid solution, the Vegard's Law.

$$a_{A_{1-x}B_x} = (1-x)\,a_A + x\,a_B \tag{11}$$

Samples were prepared by breaking off a small part of the small pellets produced and grinding on an agate mortar and pestle in acetone to prevent the spread of contamination. After grinding, a 100 µL pipette was used to transfer a small amount of the solid suspension onto a P-XRD zero-background single silicon crystal sample holder, creating a thin layer of powder on its surface after the acetone dried off. The samples were measured in a D4 Endeavour Diffractometer from Bruker AXS GmbH, Figure 14, in the 2θ range from 10° to 130° in increments of 0.02°, measurement time of 10 s per angle and a fixed slit of 1°.

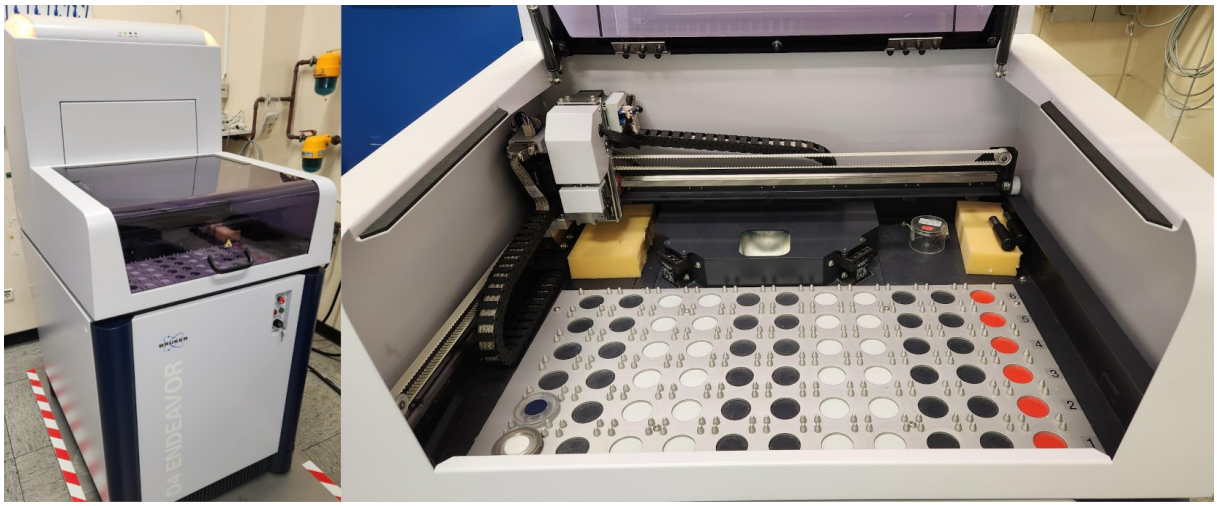

Figure 14 – D4 Endeavour Powder X-Ray Diffractometer from Bruker AXS GmbH, used for the P-XRD analysis of the UO_2 pellets.

2.3. Electron Microscopy and Microstructural Properties

As mentioned previously, a key feature of chromium doped UO_2 fuels is their increased grain size which leads to better fission gas retention. To evaluate this characteristic, as well as the sintering quality, voids, inclusions and precipitate phases, Scanning Electron Microscopy (SEM) with energy dispersive X-ray spectroscopy (EDS) measurements were conducted on select samples. On each pellet, representative regions were selected for Electron Backscatter Diffraction (EBSD).

To prepare these samples for the analysis, a polishing procedure was performed: pellets were fixed on plastic holders and CarbiMet™ silicon carbide abrasive paper of decreasing grain sizes P400, P800 and P1200 were used for the first step of polishing to create an even surface. The samples were thoroughly cleaned with water and isopropanol after each step of sanding.

The next step was to transfer the samples to Struers RotoPol-22 rotating polishing disc with a Struers RotoForce-4 rotating pressure head, Figure 15. The rotating polishing disc was set up at 150 rpm counterclockwise while the rotating head pressed the samples against and rotated in the opposite direction. Polishing solution was added to the disc during the polishing time to keep it always wet. Polishing in this machine was done according to Table 2, thoroughly cleaning the samples when changing polishing solution to remove any particles.

Figure 15 – Struers RotoPol-22 and RotoForce-4 setup for machine polishing.

Table 2 – Machine polishing steps to obtain a suitable surface for SEM analysis.

Polishing Solution	Downwards force (N)	time (min)
3µm Struers water-based diamond suspension	40	15
3µm Struers water-based diamond suspension	20	10
1µm Struers water-based diamond suspension	40	15
1µm Struers water-based diamond suspension	20	10
1µm Struers water-based diamond suspension	5	5
0.25µm Struers OP-S amorphous SiO_2 solution	15	10
0.25µm Struers OP-S amorphous SiO_2 solution	5	15

The samples were then removed from the holders and cleaned. The last polishing step was a 45 min manual finger polish on the polishing disc using the same OP-S solution and light pressure. A 10 min ultrasound bath was used in the last cleaning step to remove the leftover polishing solution. The result from polishing can be seen in Figure 16.

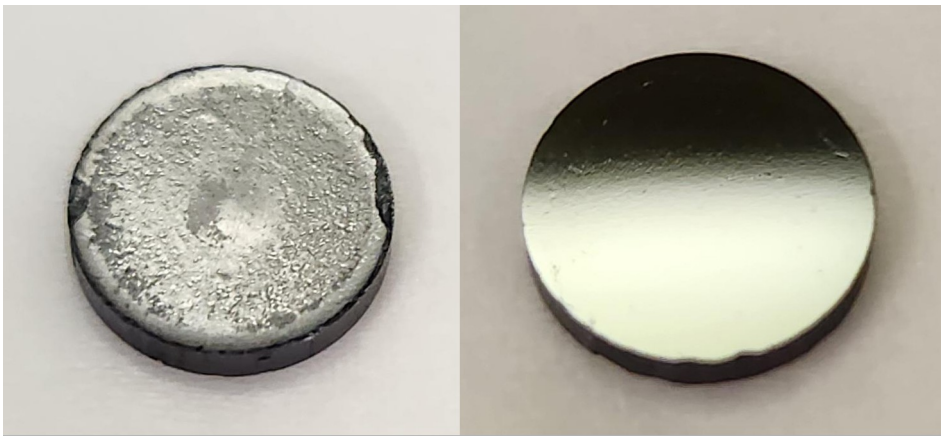

Figure 16 – Overview of the results of polishing, on the left an unpolished pellet surface, on the right a pellet after polishing with a mirror-like surface.

Electron microscopy is a technique that can extend the resolution limitations of optical microscopy allowing the micro to nano length scale to be observed using electron scattering. Several techniques and derivatives of electron microscopy have been developed, but in this dissertation, SEM was used and only this will be discussed here. SEM uses electrons obtained from a LaB_6 single crystal which are conveyed to a sample through a series of optics and apertures to create a relatively coherent beam. As the electron beam bombards a sample, two predominant scattering processes occur, the first is the back scattering of electrons (BSE) from the sample. This process is essentially ballistic, where the electron collides with an atomic nucleus and is scattered backwards towards the initial electron source where a detector is placed for measurement. Since electrons interact with atoms via their surrounding electron cloud, the collisional interaction will depend on the number of electrons present in the cloud of the nuclei and, by extension, the composition of the atom. This enables morphological features of a sample to be discerned based on element composition. BSE interactions are largely an elastic scattering process, but when high energy electrons collide with atoms, they can impart their energy on them, causing the displacement of a core electron from that atom. This displaced electron, known as a secondary electron (SE) is the second scattering process that can occur, these two interactions are illustrated in Figure 17. The SE can be guided to a detector using a potential difference. Whereas SE interactions are essentially a surface scattering process, BSE can be generated beneath the upper layers of a sample. The generated BSE need to travel towards edges and corners of the sample before they can escape it.

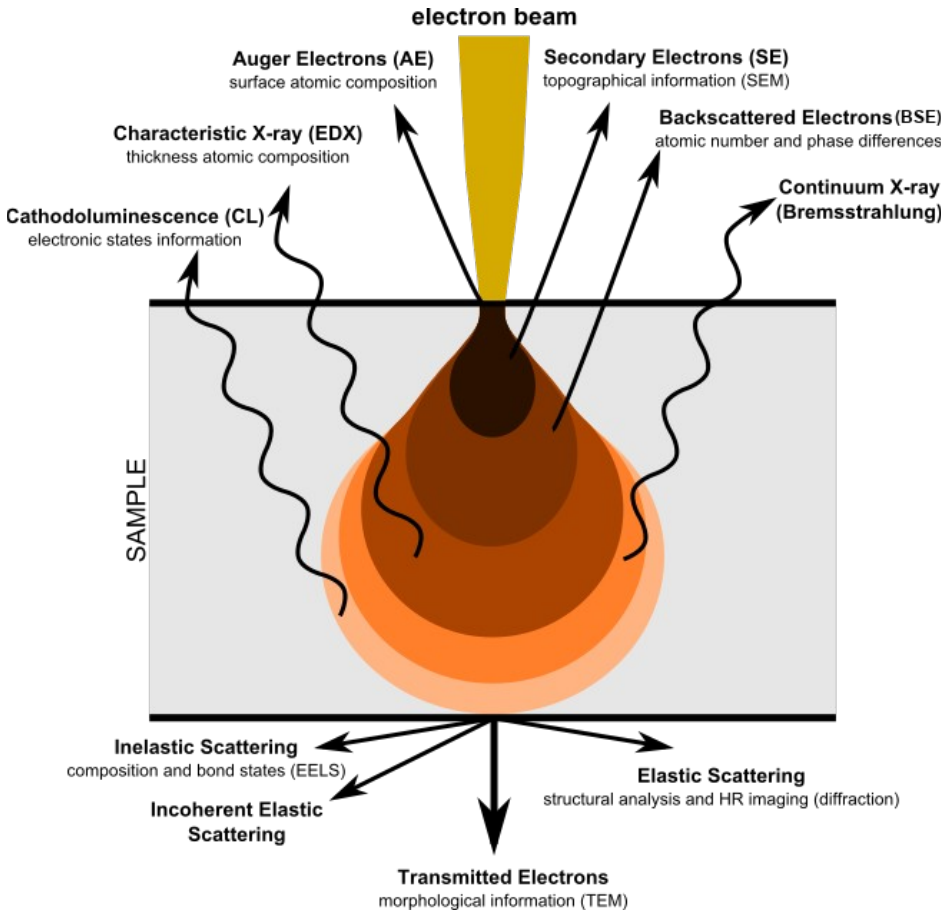

Figure 17 – Illustration of the phenomena that occur from the interaction of highly energetic electrons with matter, also depicting the pear shape interaction volume which is typically observed in this type of interactions [74].

Electron Backscatter Diffraction (EBSD) is another SEM technique that is used to study the crystallographic structure of materials. This technique is carried out in a SEM with an EBSD detector, the incident beam of electrons hit a tilted sample. The backscattered electrons leaving the sample interact with the atoms, are diffracted and lose energy, leaving the sample at various scattering angles before reaching the phosphor screen of the detector, forming Kikuchi Patterns. From these patterns, grain structure, grain orientation and phase can be obtained at the micro-scale. By mapping out the grain orientation information over an area of the sample, it is possible to determine the contours of grains as the positions where grain orientation changes significantly. Statistical analysis of grain size can be obtained from these maps.

The polished samples were glued with conductive silver onto aluminium stubs to direct the flow of electrons from the SEM out of the sample. Overview maps of the samples were collected on the Helios 5UC (Thermo scientific, Netherlands) device shown in Figure 18, SE images were collected with an Everhat Thornley Detector and BSE images with a Concentric Backscatter Detector. A high-voltage of 5 kV and a beam-current of 1.6 nA at a working distance of 4 mm was used. A tile set of the whole surface of the pellet was built using Maps 3.29 software (Thermoscientific, Netherlands) with 35 x 52 tiles with a

horizontal field width (HFW) of 300 µm per tile and image resolution of 1536 x 1024 pixels and dwell time of 1 µs.

Figure 18 – Helios 5UC Dual Beam (Thermoscientific, Netherlands) for focused ion beam scanning electron microscopy (FIB-SEM) for materials science.

EBSD measurements were performed on the same device with an Octane Elite super detector (EDAX, Ametek, USA) using EDAX APEX EBSD software. A high-voltage of 20 kV and beam current of 1.6 nA at a working distance of 9 mm was used. Images had a HFW of 300 µm and samples were tilted 70° and Dynamic Focus was used. EBSD maps were acquired using tilt correction and an image resolution of 1024 x 800, a dwell time of 43.3 µs. EBSD mapping was performed with a step size of 0.6 µm with 202872 points with binning of 4 x 4 and exposure of 50 ms. The phase was defined as UO_2. Grain distribution analysis was performed with the OIM Analysis software version 9 (Gatan/EDAX, USA).

2.4. Mechanical Properties

The mechanical properties of uranium dioxide pellets are a very important characteristic of nuclear fuel. As a ceramic, UO_2 exhibits many of the positive characteristics generally associated with them: high melting point, hardness, durability, corrosion and chemical resistance as well as high density. These characteristics have strong implications on the fuel geometry, neutron economy, behaviour under irradiation, containment of fission products and behaviour in accident conditions. One drawback of ceramics is their brittleness, leading to cracks in the material. The fracture toughness, which is a critical

stress intensity factor related to how cracks propagate through the material, is a measure of the material's brittleness [75].

Measuring the density of green pellets (ρ_g) was done by the geometrical method. The weight of each pellet (m_g) was measured on a scale, the height (h) was measured with a micrometre DIGIMATIC INDICATOR from Mitutoyo (ID-N112) with an accuracy of 0.003 mm and the diameter (D) of 1 cm was given by the size of the pressing die.

$$\rho_G = \frac{4 \cdot m_g}{h \cdot \pi D^2} \tag{14}$$

For the sintered pellets, the standard and modified Archimedes method were used, by measuring the difference in the measured mass of the pellets outside of a liquid and submerged. The standard method is only able to measure closed porosity, to measure the open porosity of the pellets, a modified Archimedes method is used, a second measurement is made with a thin coating of paraffin on the pellets.

After sintering, the thin edges of the pellets were broken off with a metal spatula and density measurements with a modified Archimedes method were performed. Firstly, the mass of the pellets was measured – m_1. Then their mass was measured in a scale submerged in water 3 times to get a stable value – m_2, Figure 19. After that, the pellets were coated by immersion in liquid hot paraffin followed by the removal of the excess and weighed – m_3. Finally, their mass with the paraffin coating was measured again in a scale submerged in water 3 times to get a stable value – m_4. The relationship for determination of densities for closed and open porosity, respectively ρ_{s1} and ρ_{s2} are given by equations (15) and (16), where ρ_w is the density of the water:

$$\rho_{s1} = \rho_w \frac{m_1}{m_1 - m_2}, \tag{12}$$

$$\rho_{s2} = \rho_w \frac{m_1}{m_3 - m_4} \tag{13}$$

Open porosity, P_{open}, closed porosity, P_{closed} and total porosity, P_{total}, are calculated according to the equations (17), (18) and (19) respectively:

$$P_{open} = \frac{\rho_{s1}}{TD} - \frac{\rho_{s2}}{TD} \tag{14}$$

$$P_{closed} = 1 - \frac{\rho_{s1}}{TD} \tag{15}$$

$$P_{total} = P_{open} + P_{closed} \tag{16}$$

Figure 19 – Archimedes setup with suspended scale in water on a Mettler-Toledo XP205-DeltaRange Scale with a Mettler-Toledo Density Accessory Kit

Next, the pellets' properties under stress were investigated: hardness and fracture toughness through a Vicker's indentation and analysis of the material under an optical microscope. The pellets were fixed onto a glass plate with resin for the measurement in the MHT-10 Microhardness Tester using a pressure of 400 N, a slope of 10 N/s and a dwell time of 10 s. Images were obtained with a Carl Zeiss Axiotech 100HD optical microscope with W-PI 10x/23 eyepiece lens and EC Epiplan-NEOFLUAR 50x/0.8 HD DIC objective lens and an Axiocam 208 colour digital camera, Figure .

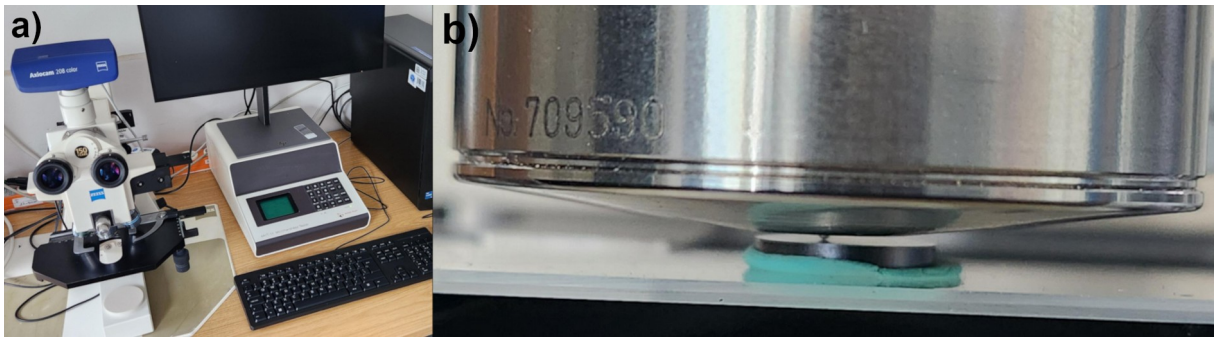

Figure 20 – Microhardness measurement setup with optical microscope a) overview, b) Vicker's indentation of a UO_2 pellet with MHT-10 microhardness tester.

3. Process Development

3.1. Introduction

Although methods for Cr-doped UO_2 and Al-doped UO_2 ceramics are proposed in literature individually [46, 65, 67], no systematic method has been proposed for the comparison of these dopants added individually and combined to UO_2. Information on commercial ADOPT™ fuel is held under confidentiality [51]. In this chapter, the step by step synthesis of Al, Al/Cr and Cr doped UO_2 materials using the co-precipitation method followed by the standard UO_2 pellet fabrication method of drying, calcination, pressing and sintering based on successful results of this institute with Cr-doped UO_2 is presented and the quality of the product is evaluated regarding yields, losses, a qualitative analysis of the techniques, dopant incorporation and the solid phases present. Doped UO_2 pellets were produced successfully and a qualitative P-XRD analysis demonstrated the presence of a single UO_2 phase in the $Fm\bar{3}m$ space group and signs of dopant incorporation.

3.2. Synthesis and Characterisation

The prepared 1.356 M uranyl nitrate solution was clear and yellow, the 0.010 M aluminium nitrate solution was clear and colourless, and the 0.011 M chromium nitrate solution was clear and with a slight tint of purple. The solutions were added to vials to produce the planned mixed solutions with molar concentrations of 0 ppm, 500 ppm, 1000 ppm, 1500 ppm and 2000 ppm of Al, Al/Cr and Cr. The resulting solutions were indistinguishable from the original uranyl nitrate solution and between each other, due to the very low amount of dopant solutions added. The dilution turned the solution into a more faded yellow. The addition of the ammonium hydroxide solution immediately produced a fine cloudy yellow precipitate which was slow to separate from the liquid. After centrifuging, the precipitate separated quite well from the aqueous phase. The discarded liquid was clear and colourless. After the three washing and centrifugation steps, the solids collected at the bottom of the centrifuge tubes can be seen in Figure 21. The details of the specific synthesis steps used are provided in Chapter 2.

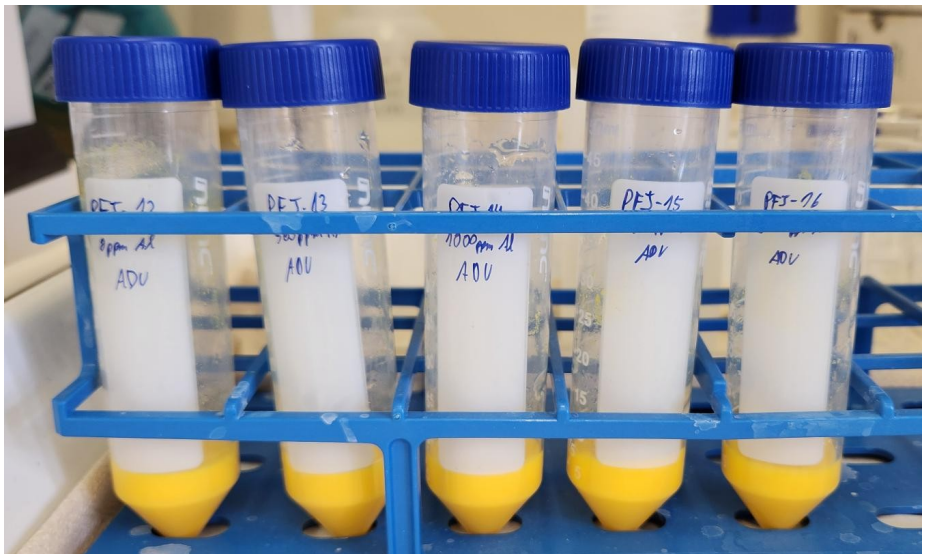

Figure 21 – ADU samples of different dopant compositions after centrifugation, from left to right 0 ppm, 500 ppm, 1000 ppm, 1500 ppm and 2000 ppm of Al.

The drying of the wet solids represented a loss of about 75% of the weight as water. After calcination of the dry ADU, the black U_3O_8 particles which can be seen in Figure 22 were obtained. These were then ground to a fine powder before transferring to alumina crucibles for reduction in H_2, each reduction batch included three alumina crucibles side by side in the oven.

Figure 22 – Platinum crucibles after calcination of samples (a), LSC vials containing U_3O_8 samples (b).

Before pressing, the UO_2 powder was again ground to reduce particle size and improve pressing performance. The pressing of green pellets was quite successful with no breaks or other problems, Figure 23. Sintering was performed in batches, with five pellets in each alumina crucible and two crucibles at each time in the oven. The rough edges left over from pressing were broken off.

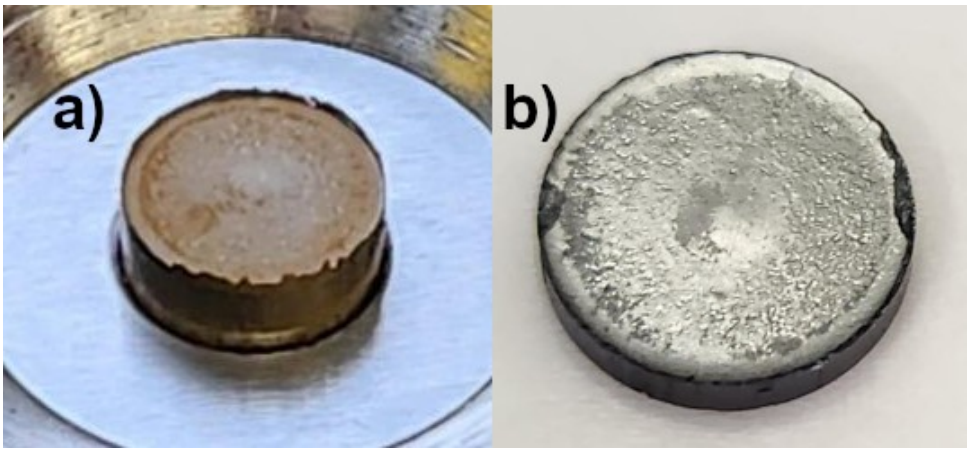

Figure 23 – Green UO_2 pellet after pressing, the image is of lower quality as the picture was taken from afar (a) and sintered UO_2 pellet (b).

3.2.1. Results of processing

Yields were determined for each synthesis step and are listed in Table 3. These steps were the added volumes of uranyl nitrate to the solutions, the mass of dried ADU after precipitation, the U_3O_8 after calcination, UO_2 after reduction, UO_2 green pellets after pressing and the UO_2 sintered pellets. The highest single loss was when transferring the wet ADU from the centrifuge tubes to the platinum crucibles, at almost 4% relative mass loss. The subsequent steps of solid transfer and synthesis generally yielded relative losses of about one percentage point. Each P-XRD sample represents a loss of around 20 mg of uranium, which is 1% of the total. The polishing of samples results in the loss of around 200 mg of uranium per pellet, which is 12% of the total starting uranium mass.

Table 3 – Synthesis yields at each step of the process; values calculated for one pellet as an average of all pellets produced.

	$UO_2(NO_3)_2$	Dry $(NH_4)_2U_2O_7$	U_3O_8	UO_2 powder	UO_2 green pellet	UO_2 sintered pellet
Mass of compound (g)	2.769	2.108	1.878	1.784	1.765	1.742
Mass of Uranium (g)	1.673	1.608	1.592	1.572	1.555	1.536
Relative yield (%)	100.0%	96.1%	95.2%	94.0%	93.0%	91.8%

3.3. Phase Identification

As described in 2.2, P-XRD measurements were performed on the samples in the 2θ range from 10° to 130° in increments of 0.02°, measurement time of 10 s per angle and a fixed slit of 1°. Raw diffraction patterns of all measured compositions are provided for Al-doping in Figure 24, for Al/Cr doping in Figure 25 and for Cr-doping in Figure 26. Extremely subtle peak shifting could be observed towards lower 2θ with increasing dopant content, consistent with literature [76]. The incorporation of the small Al^{3+} and Cr^{3+} cations within the UO_2 lattice will involve a lattice contraction to account for the substitution with the large U^{4+} cation [77, 78]. This shift in peak positions can be subtly observed in Figure 27. The observation of shifting to lower 2θ is consistent and evidence for lattice incorporation for Al^{3+} and Cr^{3+}, indicating successful synthesis. However, proper quantification could not be achieved for these, particularly the relative rate of contraction when comparing the two dopants and when co-doped.

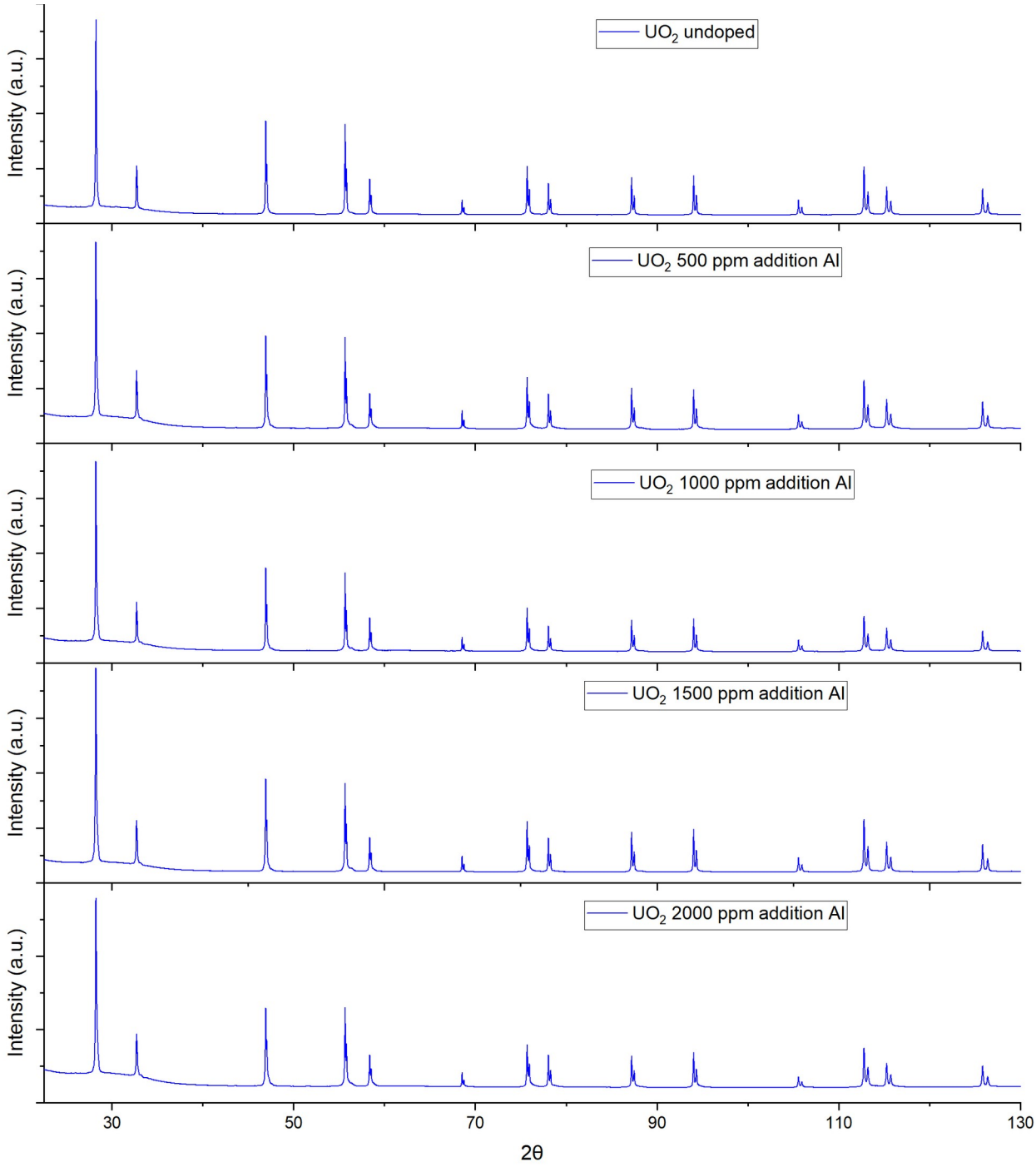

Figure 24 – Raw P-XRD data obtained for the samples of UO_2 aluminium doping: (a) 0 ppm, (b) 500 ppm, (c) 1000 ppm, (d) 1500 ppm and (e) 2000 ppm in the 2θ range of 25 – 130 °.

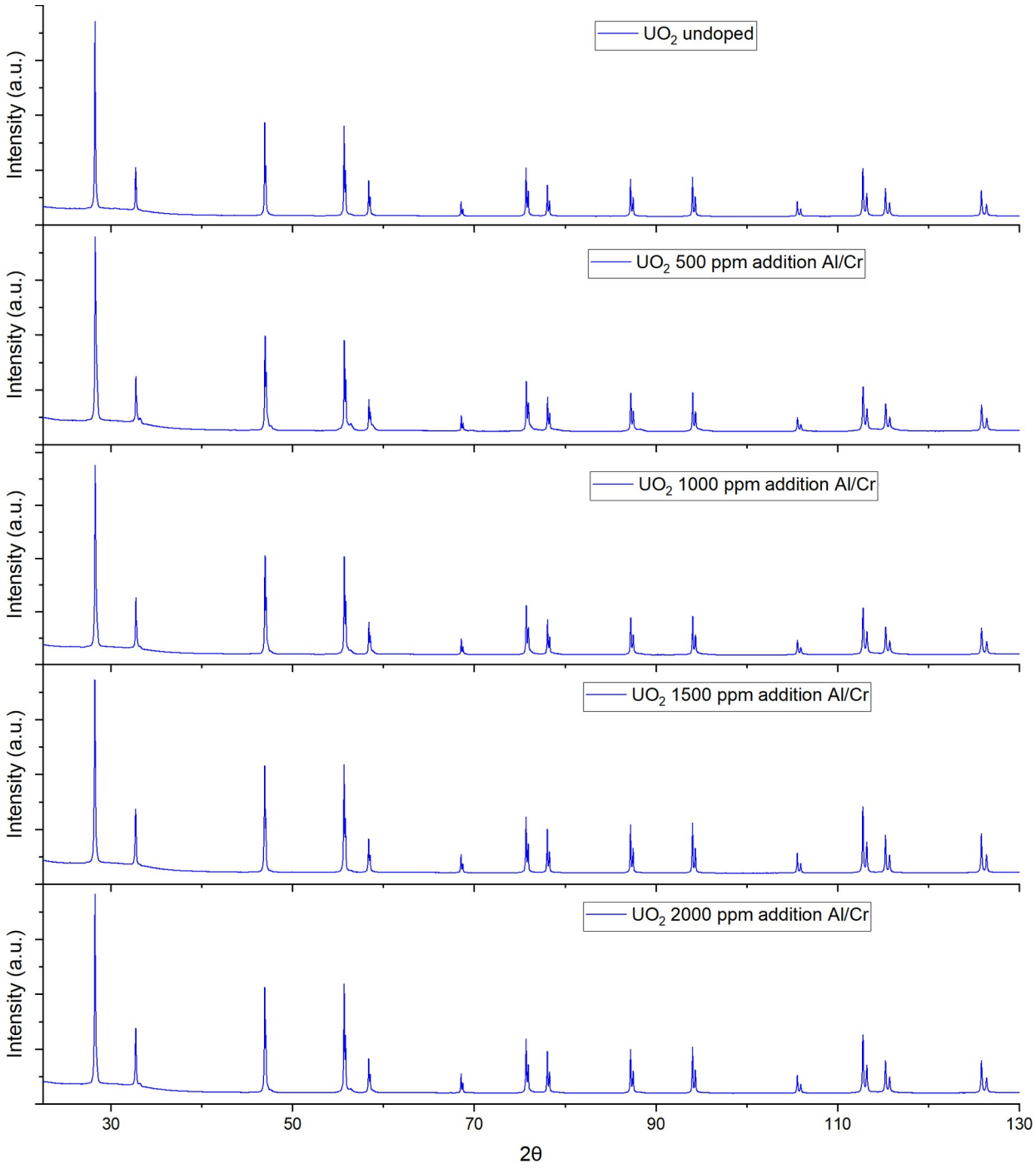

Figure 25 - Raw P-XRD data obtained for the samples of UO_2 aluminium/chromium doping: (a) 0 ppm, (b) 500 ppm, (c) 1000 ppm, (d) 1500 ppm and (e) 2000 ppm in the 2θ range of 25 – 130 °.

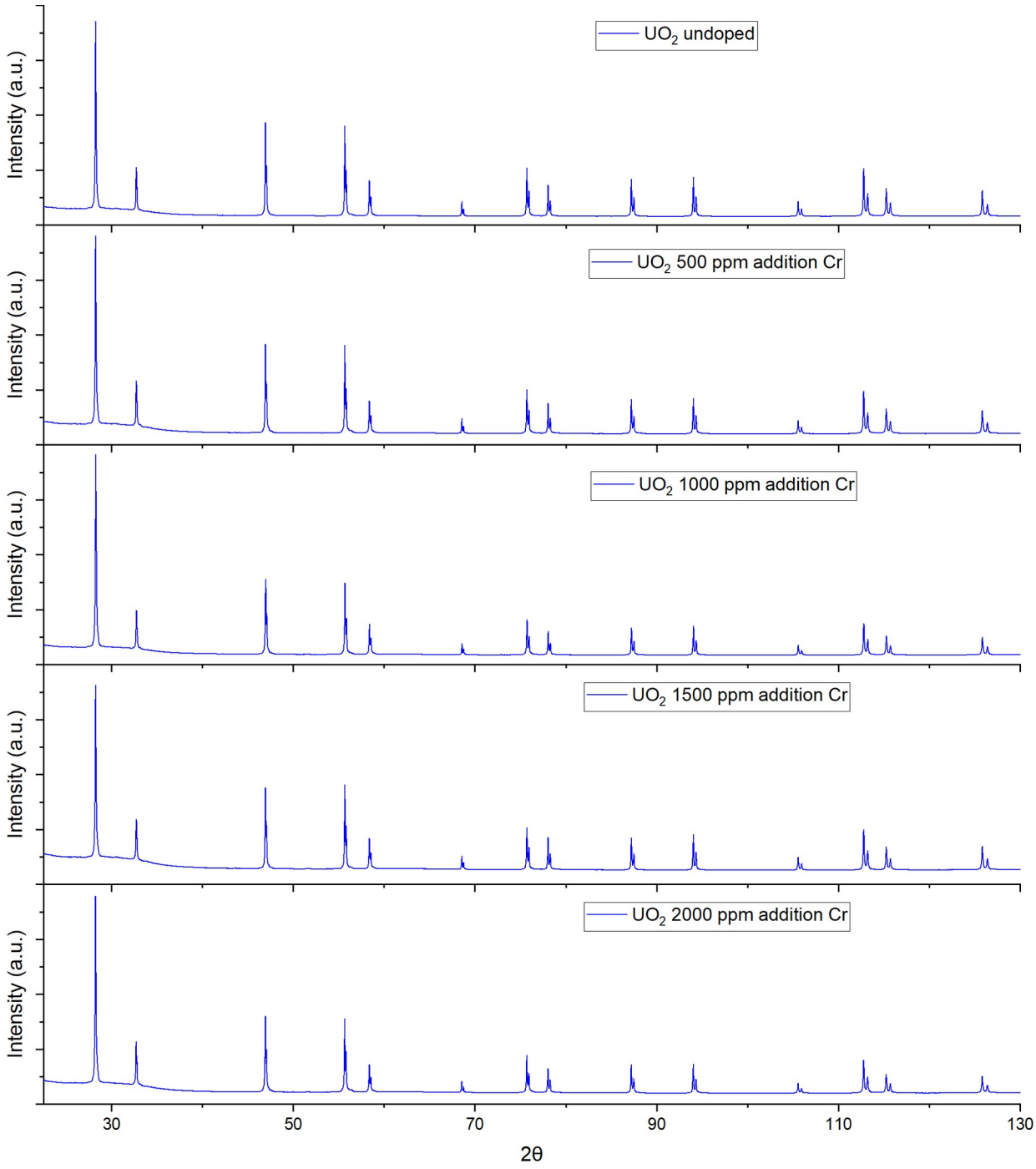

Figure 26 - Raw P-XRD data obtained for the samples of UO_2 chromium doping: (a) 0 ppm, (b) 500 ppm, (c) 1000 ppm, (d) 1500 ppm and (e) 2000 ppm. in the 2θ range of 25 – 130 °.

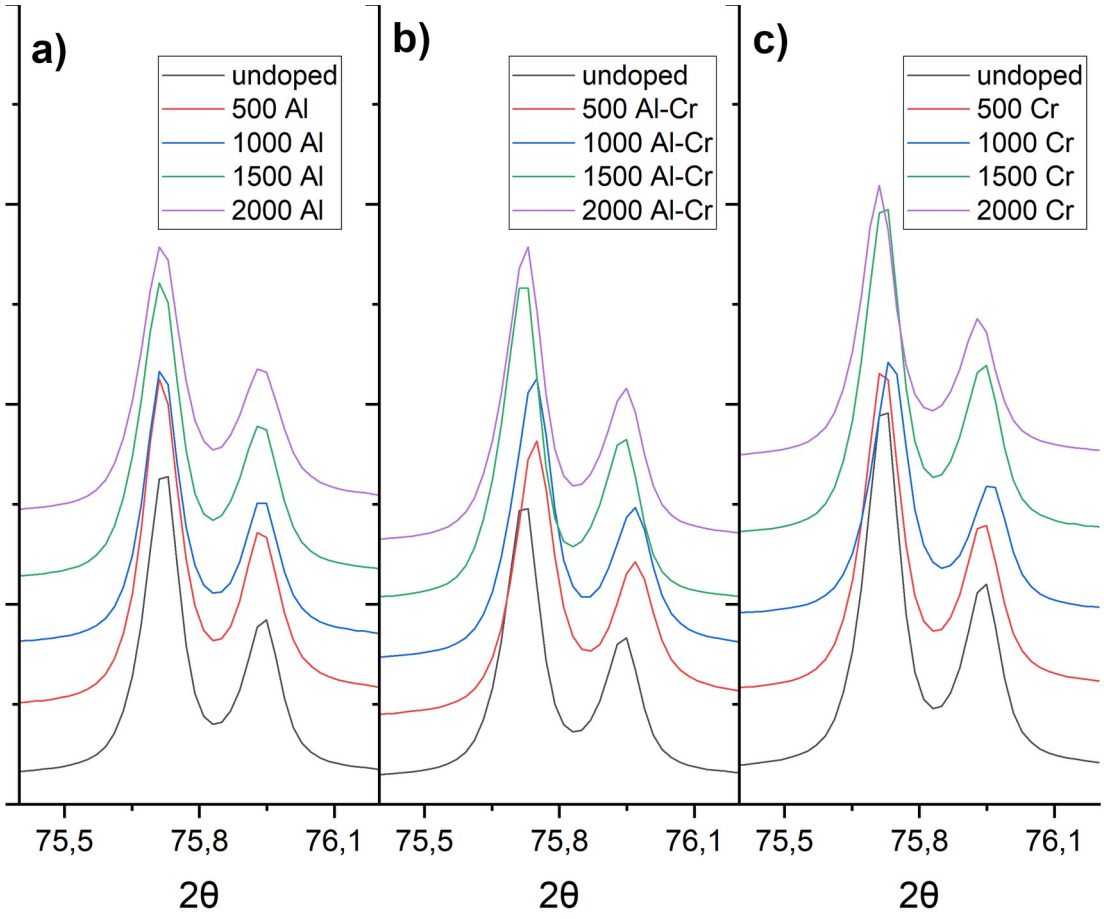

Figure 27 – Magnified detail from the measured P-XRD patterns of the UO_2 doped with (a) Al, (b) Al/Cr and (c) Cr showing peak shifting between 74.4 to 76.2 °. P-XRD spectra vertically normalized and offset for comparison.

3.4. Discussion

From the P-XRD analysis results, the synthesis method successfully produced UO_2 pellets doped with Al, Al/Cr and Cr with high yields. The results are consistent with previous results with Cr-doped UO_2 [46]. The samples doped with Al and Al/Cr show lattice contraction compatible with its incorporation into UO_2. A better quantification of the incorporation of each dopant is achieved through Rietveld refinement in the next chapter.

The co-precipitation method used to achieve Al/Cr doping differs from the one used in Westinghouse's ADOPT fuel which uses dry mixing of oxides. The utilized method is better suited for laboratory work by limiting the handling of dry radioactive powders and the use of ball milling. Finally, in the sintering step at high temperatures, diffusion processes dominate any heterogeneity produced in previous steps, producing homogeneous materials. The pellets produced were a single phase UO_2 material without any secondary metal or oxide phases.

To summarise, a successful synthesis method for the comparison of Al, Al/Cr and Cr-doped UO_2 has been developed. The resulting materials will be more thoroughly analysed in the following chapters.

4. Structural Chemistry

4.1. Introduction

It has been previously shown that the uptake of trace dopants within UO_2 including Cr can be monitored via precise P-XRD measurement and analysis. Accordingly, in order to determine the relative uptake of Al, Al/Cr and Cr within UO_2 materials detailed P-XRD measurements of them and subsequent Rietveld refinement were performed and described in this chapter. By performing these measurements and analysis, a relative rate of incorporation is established in addition to relative solubility between the investigated dopants.

4.2. Structural characterisation

As described in Chapter 3, Rietveld refinements were performed against all collected diffractograms. A starting model based on the UO_2 fluorite structure in space group $Fm-\bar{3}m$ was used consistently. For refinement analysis, lattice parameters of the fluorite models were refined together with the instrument parameters, scale factor and also the background using a model based on a Chebyschev-1 function. Due to the grinding process in P-XRD sample separation being performed in air, partial oxidation of the sample was observed. To account for this in the refinements, additional UO_2 based models were introduced and the phase fraction refined. This effect has been previously often described for regular UO_2 and it is established to be not related to Al/Cr doping but rather fine powder oxidation prior to P-XRD measurement [76, 79, 80]. Due to the low amount of Al/Cr expected in the UO_2 lattice as previously found [49], the Rietveld refinements did not include Al/Cr in the atomic parameters. The refinement plots are provided for Al doping in Figure 28, for Al/Cr doping in Figure 29 and for Cr doping in Figure 30 together with tabulated values of the lattice and statistical fitting parameters in in Table 4.

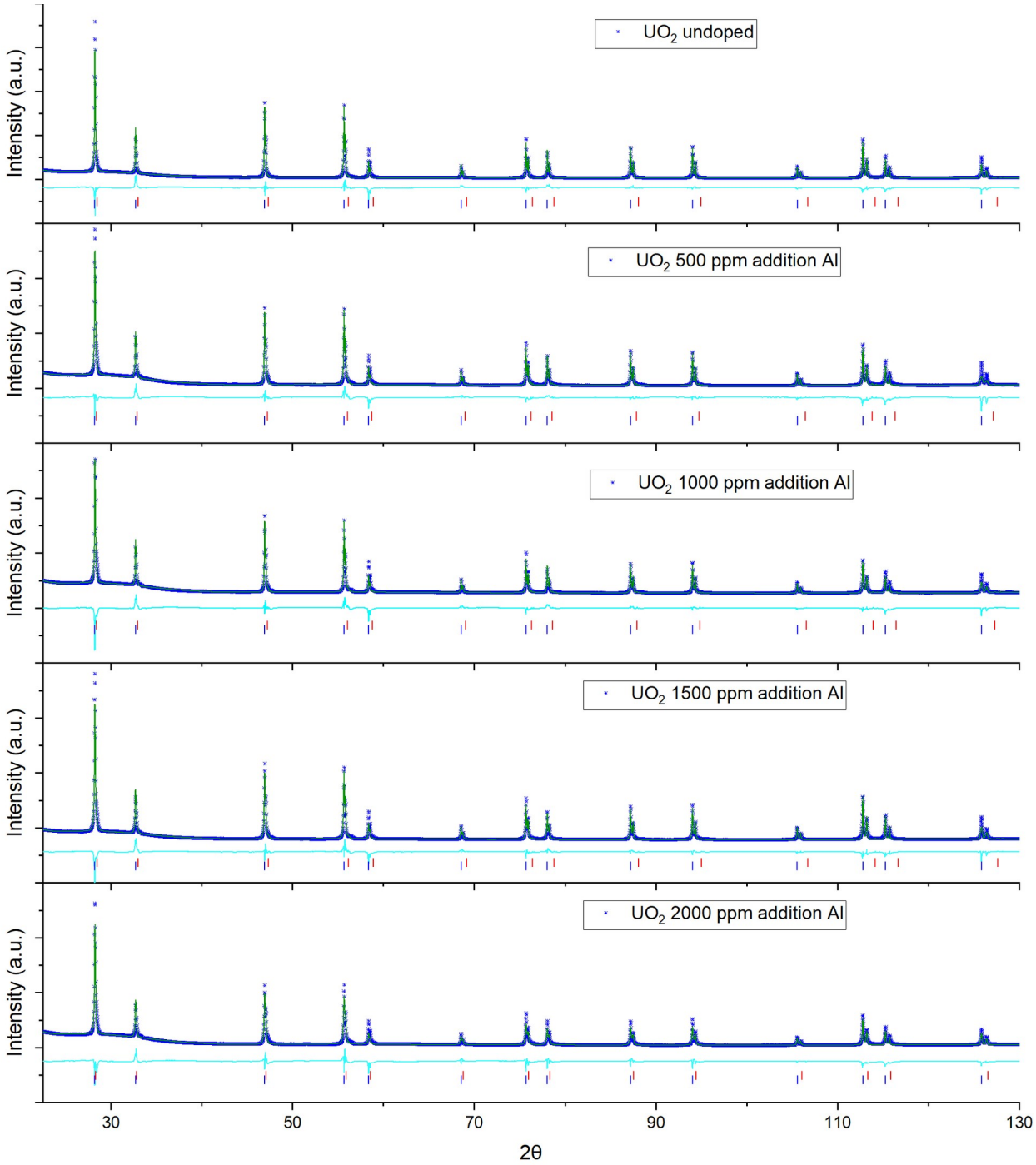

Figure 28 – Rietveld profiles of Al-doped UO_2 samples (a) 0 ppm, (b) 500 ppm, (c) 1000 ppm, (d) 1500 ppm and (e) 2000 ppm. The green upper and cyan lower lines, blue markers and vertical red and blue markers respectively represent the refined model, difference curve, raw data and allowed reflections according to the major fluorite UO_2 phase and minor oxidized UO_2 phase both in space group $Fm\bar{3}m$.

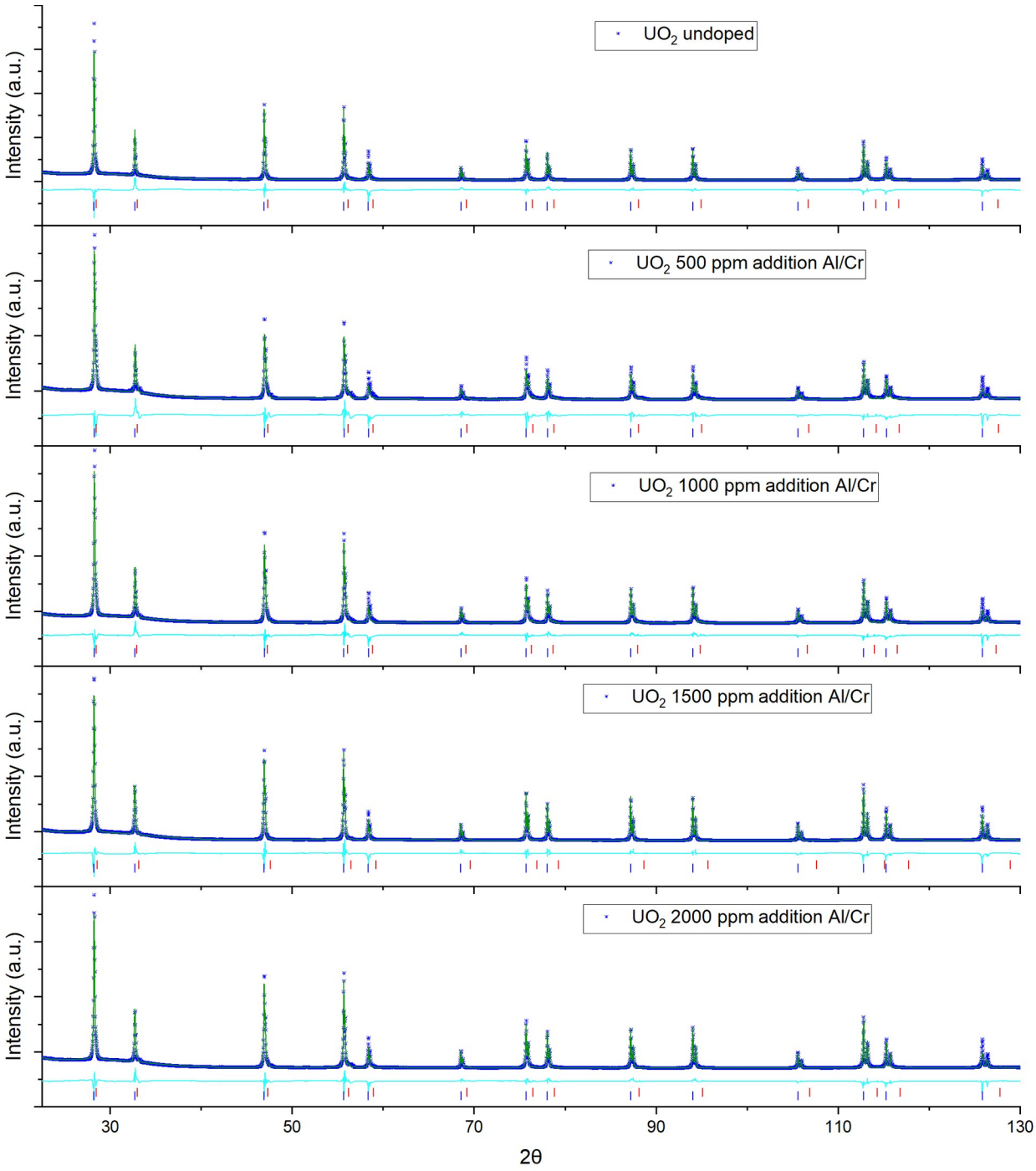

Figure 29 – Rietveld profiles of Al/Cr doped UO_2 samples (a) 0 ppm, (b) 500 ppm, (c) 1000 ppm, (d) 1500 ppm and (e) 2000 ppm. The green upper and cyan lower lines, blue markers and vertical red and blue markers respectively represent the refined model, difference curve, raw data and allowed reflections according to the major fluorite UO_2 phase and minor oxidized UO_2 phase both in space group $Fm\bar{3}m$.

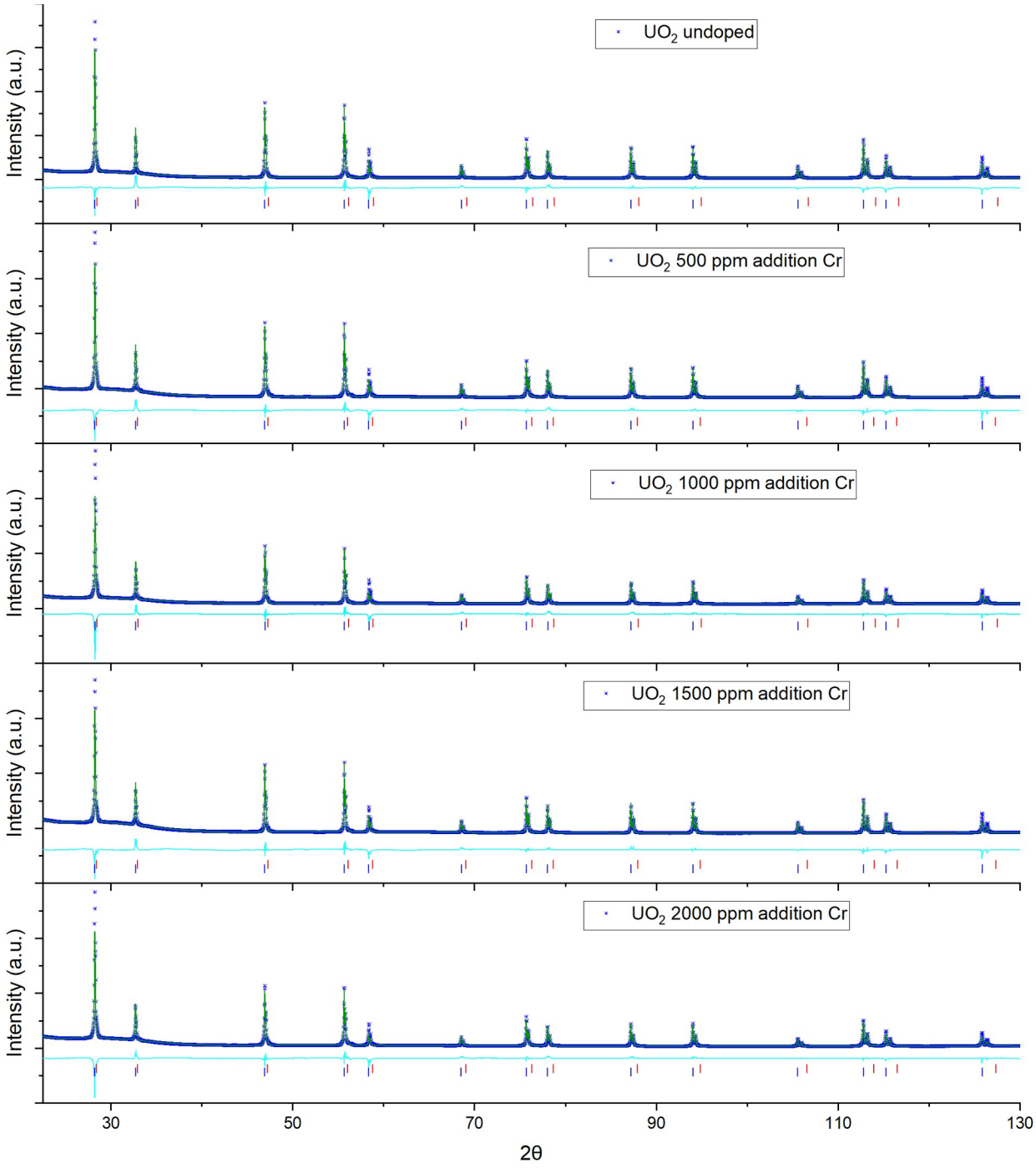

Figure 30 – Rietveld profiles of Cr doped UO_2 samples (a) 0 ppm, (b) 500 ppm, (c) 1000 ppm, (d) 1500 ppm and (e) 2000 ppm. The green upper and cyan lower lines, blue markers and vertical red and blue markers respectively represent the refined model, difference curve, raw data and allowed reflections according to the major fluorite UO_2 phase and minor oxidized UO_2 phase both in space group $Fm\bar{3}m$.

From the refinements, the lattice parameters for the main UO_2 phase were obtained. They are presented in Table 4, according to the type of dopant and amount. To better visualize the contraction of the unit cell with the addition of dopant, a graph of the normalized lattice parameter with respect to the undoped UO_2 is presented in Figure 31. For the series of Cr-doped samples, the decrease in the lattice parameter is less pronounced than for the samples with aluminium doping, which is consistent with its bigger ionic radius. At high doping amounts with Al and with Al/Cr, a saturation value

appears to be reached due to the solubility limit, this behaviour is indicated by the arrows in Figure 31.

Table 4 – Lattice parameters of the main UO_2 phase obtained for each of the samples from the Rietveld refinement model and statistical fitting values of the Rietveld refinement.

Doping amount (molar ppm)	Lattice Parameters (Å)			Statistical fitting values – wR and R		
	Al-doped	Al/Cr-doped	Cr-doped	Al-doped	Al/Cr-doped	Cr-doped
0	5.47121(5)	5.47121(5)	5.47121(5)	11.00% 7.82%	11.00% 7.82%	11.00% 7.82%
500	5.47102(2)	5.47108(3)	5.47117(2)	10.97% 7.29%	13.31% 9.04%	9.94% 7.07%
1000	5.47099(3)	5.47092(3)	5.47115(2)	11.22% 7.80%	11.18% 7.85%	11.64% 8.00%
1500	5.47077(2)	5.47085(2)	5.47101(3)	11.67% 8.12%	9.54% 6.78%	8.62% 6.06%
2000	5.47087(4)	5.47091(2)	5.47098(4)	11.55% 8.01%	10.26% 7.27%	9.75% 6.92%

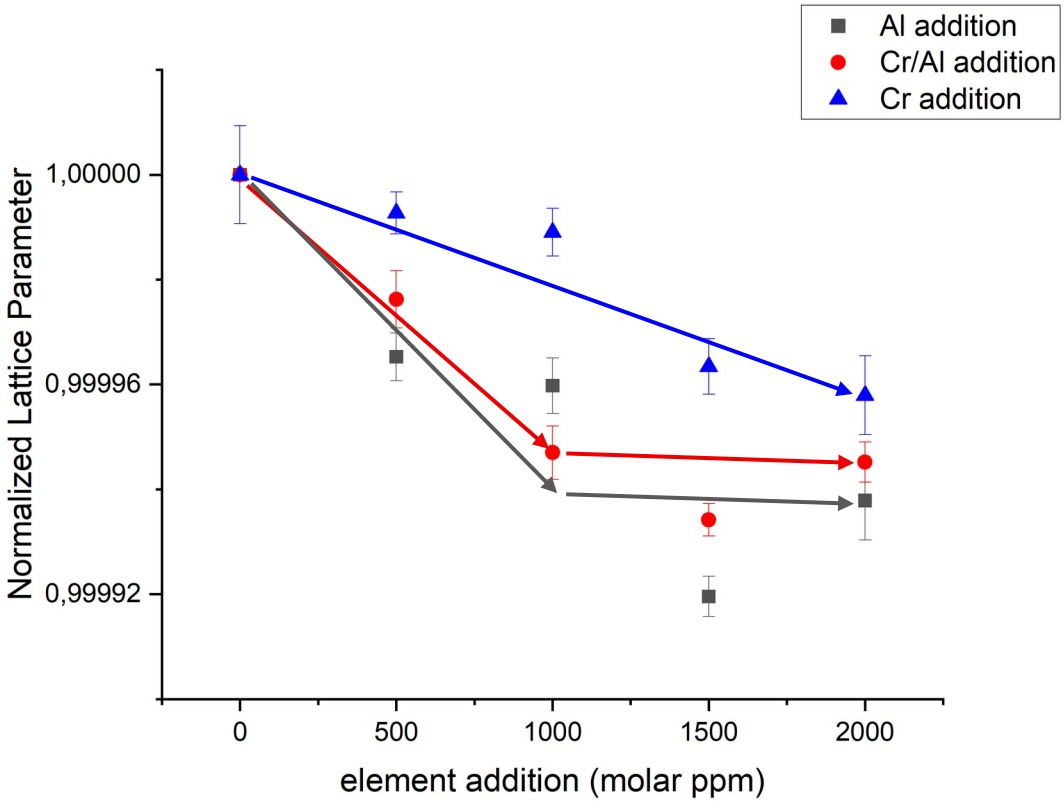

Figure 31 – Normalized lattice parameter as a function of the amount of added dopant shown in molar ppm amounts added for Al (black), Al/Cr (red) and Cr (blue). The arrows show the difference in lattice parameter change, for Cr a near linear change up to 2000 ppm is observed, for Al and Al/Cr the lattice parameter decreases linearly up to a point, then increases again indicating a saturation.

4.3. Discussion

The resulting P-XRD patterns present very subtle peak shifting, consistent with a contraction of the unit cell. However, looking at individual shifts in peak positions to determine the lattice parameters is complicated due to broad peaks, $K_{\alpha 2}$ reflections and measuring trace amounts of incorporated dopants [76]. A sharper XRD pattern such as one obtained by synchrotron XRD could provide a clearer picture of these shifts. In our case, the Rietveld refinement technique was able to provide fitting lattice parameters, despite the lower quality data.

The incorporation of dopant cations Al^{3+} and Cr^{3+}, which have smaller ionic radii than U^{4+}, into the UO_2 fluorite matrix leads to a contraction of the unit cell [76]. The contractions observed are consistent with the ionic radii of the different dopants [77, 78], a smaller contraction for Cr-doped UO_2, a bigger contraction for Al-doped UO_2. For the Al/Cr-doped UO_2, even though the formation of a eutectic is expected, a proportion of both Al and Cr enter the UO_2 in solid solution even though there is a solubility difference between the ions. This results in the shown contraction that is in-between the ones for each single dopant case.

The solubility of chromium at sintering temperatures of 1700 °C is about 700 wt. ppm of Cr_2O_3, which is equivalent to around 2500 molar ppm [59, 64], while the solubility of aluminium is around 42 µgAl/gU, which is equivalent to around 370 molar ppm [66, 67]. So, in the case of our Al- and Al/Cr-doped UO_2 materials, the solubility of Al is well exceeded, even when considering the potential losses due to volatility, while in the case of the Cr-doped UO_2 we are below its solubility limit.

Generally, two competing effects contribute to the formation energy of solid solutions, endothermic deviation from ideal behaviour related to cation size differences and partial stabilization of the system due to the exothermic formation of defect clusters [81]. In redox-active hosts, the redox enthalpy, in this case, the enthalpy of oxidation must be accounted for. Computational work considering both charge compensating mechanisms, however, is scarce. The stability of solid solutions of type $U_{1-x}M_xO_2$ relative to constituent oxides has been shown to increase with increasing size of the trivalent metal, which explains the general high solubility of e.g. lanthanide elements in the UO_2 matrix [82, 83]. With increasing cation radius of the trivalent dopant, an increasing preference for higher oxygen coordination has also been established. This has been shown for La and Y substituted UO_2, where computational data shows a decreasing formation enthalpy with increasing dopant radius [82]. In the Y-substituted systems, structures with an enhanced number of vacancies around the Y^{3+} ions are found to be favoured energetically, while the opposite is found for La-substituted systems [83]. The different charge compensation mechanisms for larger and smaller lanthanide cations also appear to depend on the

cation size of the dopant. For lanthanide substituted UO_2, charge compensation via the oxidation of U^{+4} to U^{+5} is well-established [84, 85]. As the energetics of solid solution formation and associated charge compensation mechanisms are very complex and warrant detailed studies, we can only rationalize the charge compensation mechanism in the Cr^{3+}-doped UO_2 structure considering the differences between dopant and host cation radii. Cr^{3+} with a coordination number of six, has a cation radius of 0.615 Å and Al^{3+} with a coordination number of six has a cation radius of 0.530 Å. Uranium in oxidation states +IV and +V are significantly larger, with radii of 0.86 and 0.79 Å [86], respectively, for the same coordination. In solids where the aliovalent dopant is smaller than the host cation (such as Cr^{3+} in UO_2), the dopant shows a tendency to attract oxygen vacancies, thereby reducing its coordination number. Moreover, the introduction of charge compensating oxygen vacancies, which are slightly larger than the oxygen anions in the lattice, partly compensate for the lattice contraction observed for small dopants [87]. If on the other hand oxidation of U^{4+} to U^{5+} for charge compensation is considered, the redox reaction would result in further contraction of the UO_2 lattice. This would be considered unfavourable due to the increased lattice energy deviation from ideal behaviour. The formation of Cr^{3+} and oxygen vacancies is further supported by recent studies [49].

To summarise, the effects of Al, Al/Cr and Cr doping on the microstructure of UO_2 have been studied, their rate of incorporation and effects are explained with reference to literature.

5. Microstructural Properties

5.1. Introduction

The grain growth in doped UO_2, as described in the introduction, is dependent upon the ability to form eutectics as well as on the lattice incorporation of dopants. It has already been shown that variable incorporation has been found due to differences in size between the Al and Cr cations. Subsequently, to determine the effect of dopants upon the microstructure and particularly grain growth of Cr, Al/Cr and Al materials, this chapter presents SEM images of six chosen samples, due to time constraints. An exemplary Cr-doped UO_2, with the highest doping of 2000 ppm, as a reference for the other dopants. Two Al-doped UO_2 at 1000 ppm and 2000 ppm to observe the effect of Al and three different Al/Cr-doped UO_2, at 500, 1000 and 2000 ppm, as it is the focus of this research.

In this chapter, microstructural analysis via focused ion beam scanning electron microscopy using detectors for SE, BSE and EBSD of UO_2 samples doped with Al, Al/Cr and Cr are described. Overview map and enhanced zoom images of each sample are analysed and EBSD data is evaluated to determine the grain size distribution. The subsequent identified variability in microstructural behaviour and performance is discussed in relation to the chemistry of the dopants under sintering conditions. Details of material preparation and electron microscopy measurement are provided in 2.3.

5.2. Scanning Electron Microscopy

5.2.1. Cr-doped UO_2

Looking at the overview map for the 2000 ppm Cr-doped UO_2 pellet, which can be seen in Figure 32, the overall impression is of a homogeneous pellet with small grains.

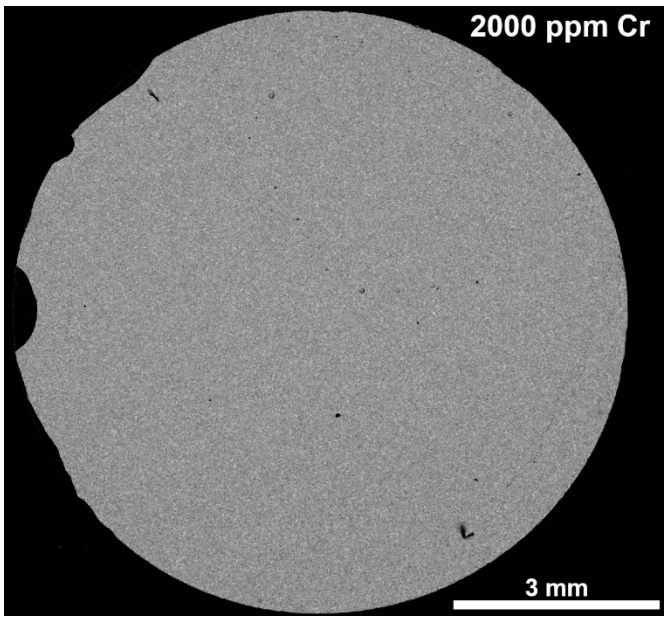

Figure 32 – SEM-SE Overview map of a 2000 ppm Cr-doped UO_2 pellet. The Image is constructed by stitching together 35 x 52 tiles of 300 µm HFW. The dark rounded spots on the left of the pellet are caused by the silver paint used to provide electrical contact between the pellet and the sample holder.

A closer look at the 2000 ppm Cr-doped UO_2 pellet, shown in Figure 33, reveals a structure with small pores and small grains. No clear difference is observed between the images at centre, mid-radius and rim.

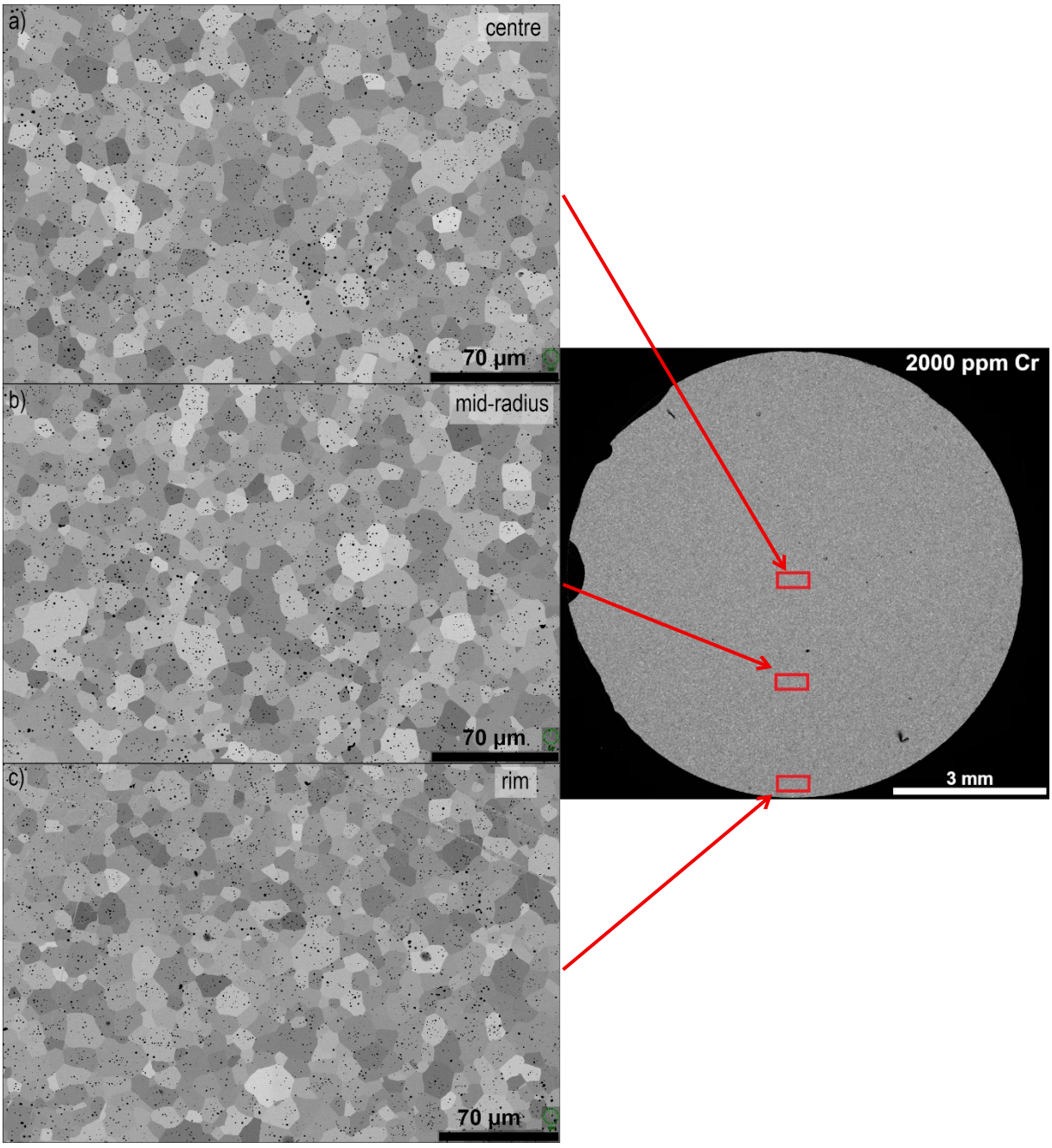

Figure 33 – SEM-SE images of 2000 ppm Cr-doped UO_2 with a window width of 300 µm at the (a) centre of the pellet, (b) mid-radius and (c) rim. The green circle at the bottom left of each image shows the alignment, which was the same for all images. The overview image of the pellet is shown as a reference of where the enhanced zoom images were taken.

5.2.2. Al-doped UO_2

Observing at the overview maps for the 1000 ppm and 2000 ppm Al doped UO_2 samples provided in Figure 34, the pellets appear largely homogeneous, free of cracks or superficial damage. The shaded regions for the pellet with the higher dopant content are residuals leftover from the polishing process.

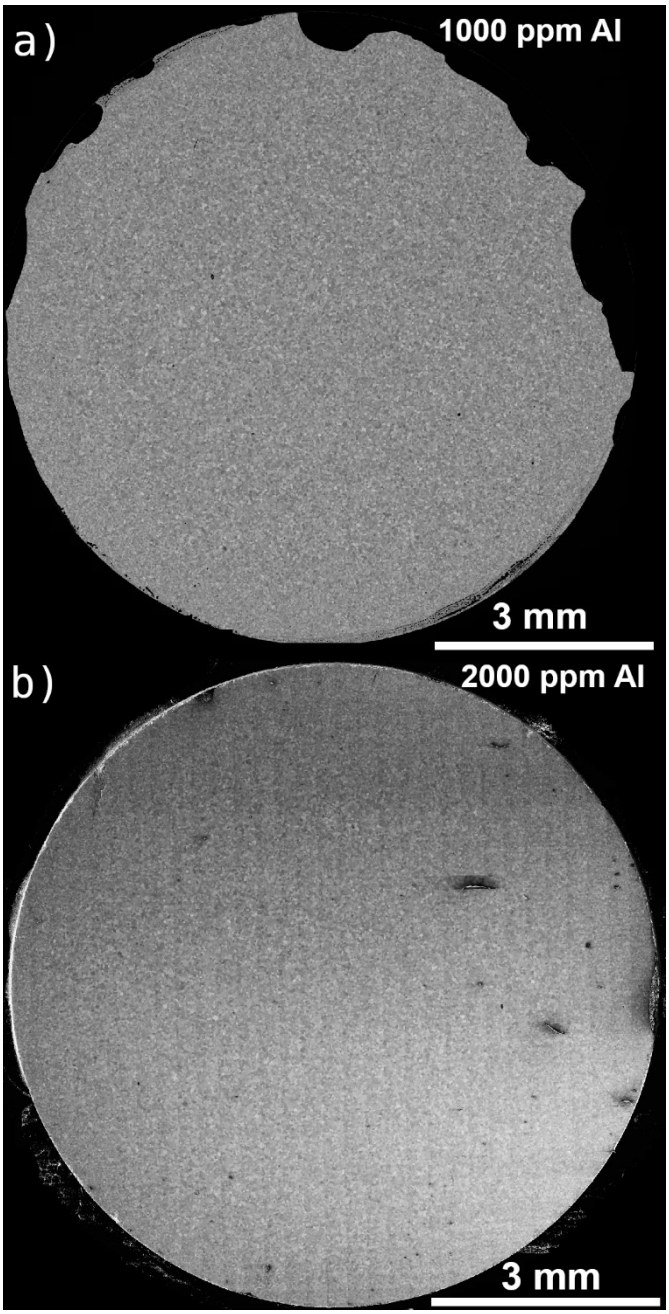

Figure 34 – SEM overview maps of UO_2 pellets doped with Al with (a) 1000 ppm and (b) 2000 ppm. Images are constructed by stitching together 35 x 52 tiles of individual 300 µm HFW. The dark rounded spots around the pellet (a) are caused by the silver paint used to provide electrical contact between the pellet and the sample holder.

Further inspection of the 1000 ppm Al-doped UO_2 pellet at higher magnification, shown in Figure 35, reveals that the material possesses some small pores and a consistent grain size along its radius. Notably, when comparing to regular UO_2 that has an average grain size of 1-5 um (as shown in Figure 7 of Chapter 1), the 1000 ppm doped pellet has an improved grain size.

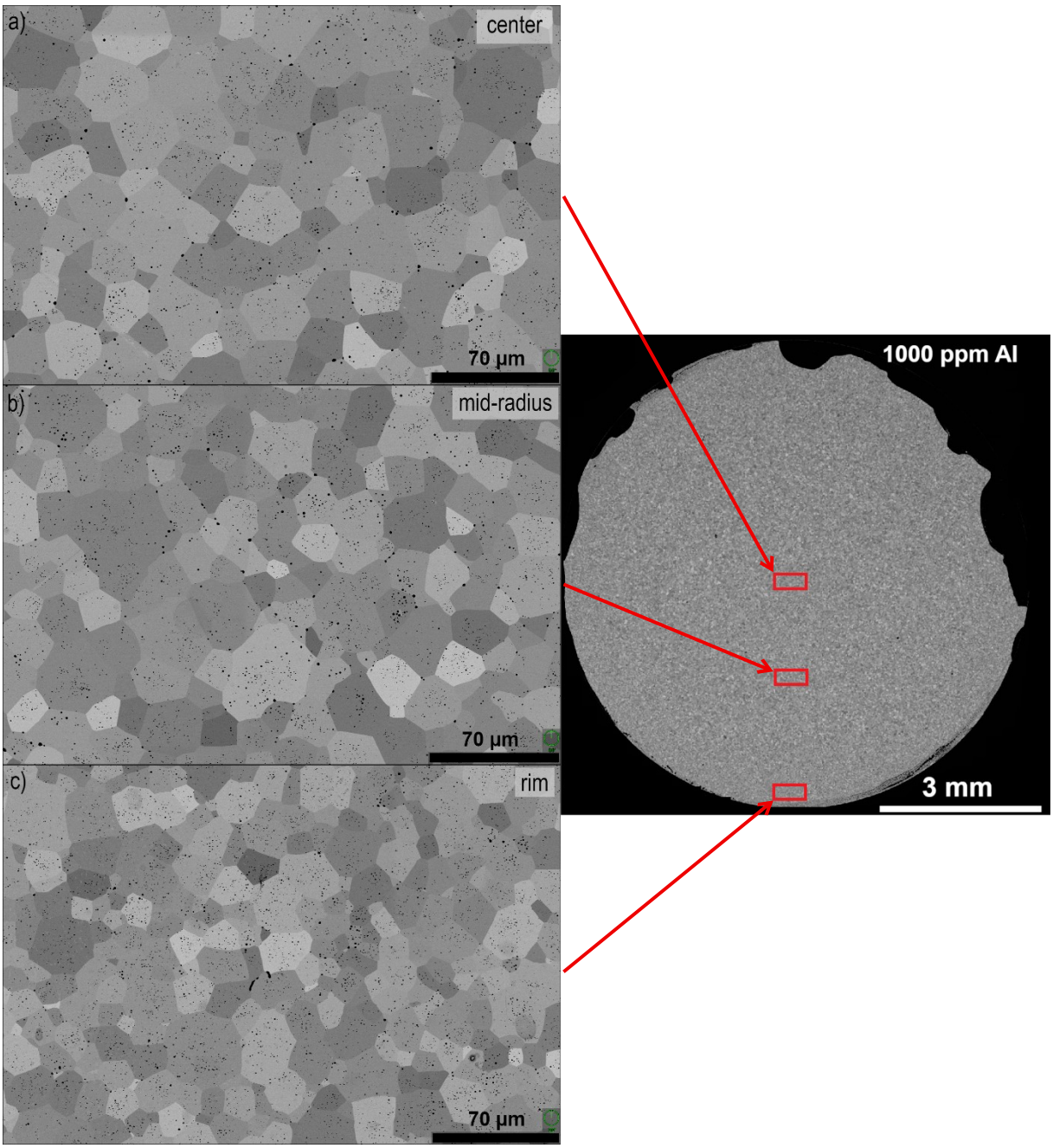

Figure 35 – SEM-SE images of the 1000ppm Al-doped UO_2 pellet with a window width of 300 µm at (a) centre of the pellet, (b) mid-radius and (c) rim. The green circle at the bottom left of each image shows the alignment, which was the same for all images. The overview image of the pellet is shown as a reference of where the enhanced zoom images were taken.

Examination of the 2000 ppm Al-doped UO_2 pellet at higher magnification, shown in Figure 36, in comparison to the 1000 ppm Al-doped UO_2, highlights a non-linear distribution of grain size behaviour when comparing between the centre and rim pellet regions. In particularly at the rim, a clear reduction in the grain size closer is observed. Despite the apparent reduction in grain size towards the rim of the pellet, the 2000 ppm doped Al-UO_2 centre region does appear to possess improved grain growth, more so then the 1000 ppm doped Al-UO_2 sample in comparison.

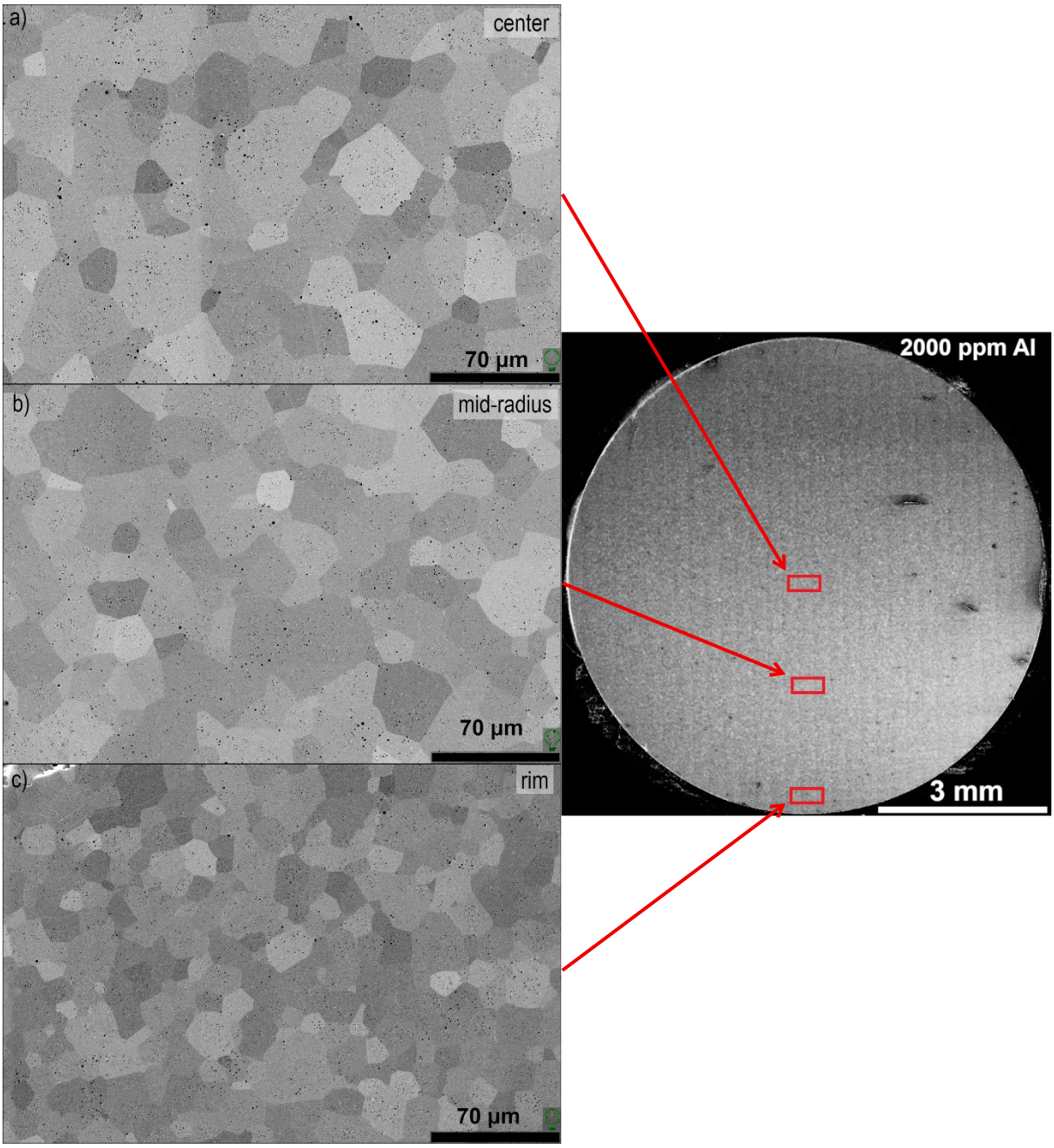

Figure 36 – SEM-BSE images of 2000 ppm Al-doped UO_2 pellet with a window width of 300 µm at (a) centre of the pellet, (b) mid-radius and (c) rim. The green circle at the bottom left of each image shows the alignment, which was the same for all images. The overview image of the pellet is shown as a reference of where the enhanced zoom images were taken.

5.2.3. Al/Cr-doped UO_2

Looking at the overview maps for the 500, 1000 and 2000 ppm Al/Cr doped UO_2 pellets, Figure 37, it can be immediately seen that there is a general trend of increasing dopant appears to result in more cracking and less homogeneity. At 500 ppm addition, no cracking is observed, at 1000 ppm some radial cracks appear and at 2000 ppm addition radial and circular cracks can be seen.

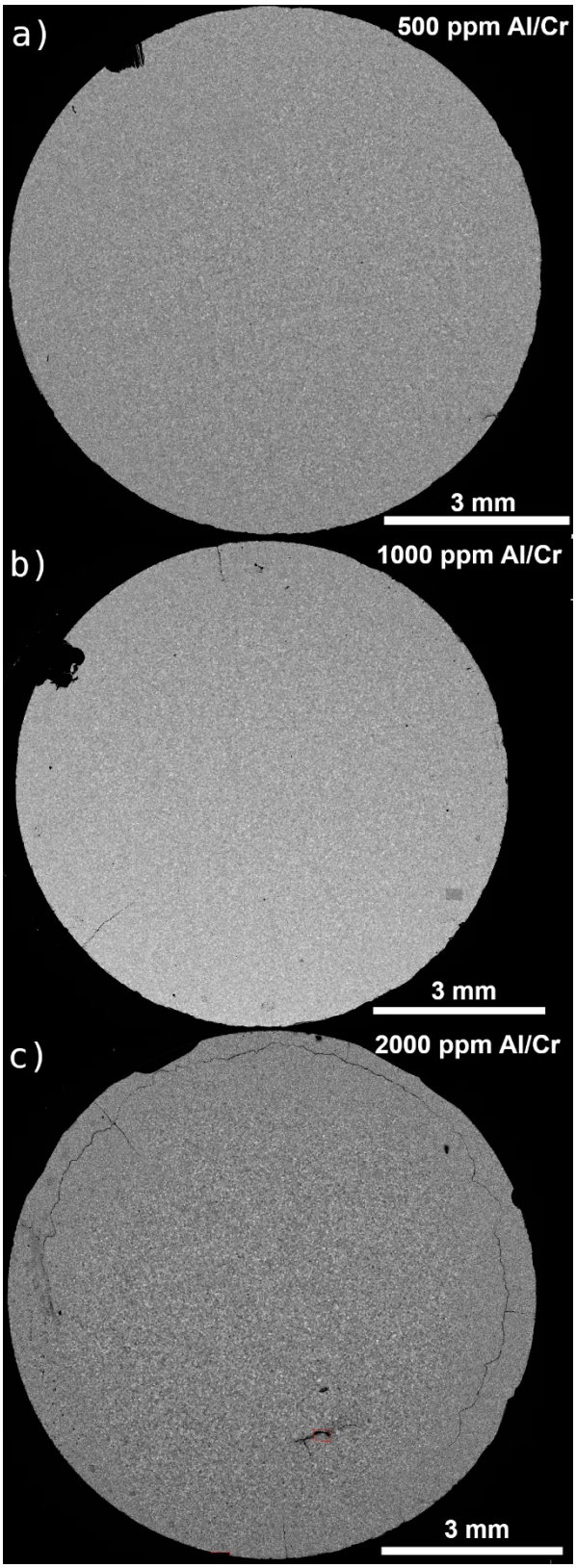

Figure 37 – SEM-SE overview maps of a UO_2 pellet doped with Al/Cr with (a) 500 ppm, (b) 1000 ppm and (c) 2000 ppm. Images are constructed by stitching together 35 x 52 tiles of 300 µm HFW. The dark rounded spots on the borders of the pellets are caused by the silver paint used to provide electrical contact between the pellet and the sample holder.

Observing the 500 ppm Al/Cr-doped UO_2 pellet at higher resolution, as shown in Figure 38, reveals smaller grains and a more porous structure than the pellets doped with Al. No difference is observed at the rim. In this case, the amount of dopant is so small that its properties are not much different from the undoped UO_2 material, this amount of added dopant also does not give improved densities as seen in Chapter 6.

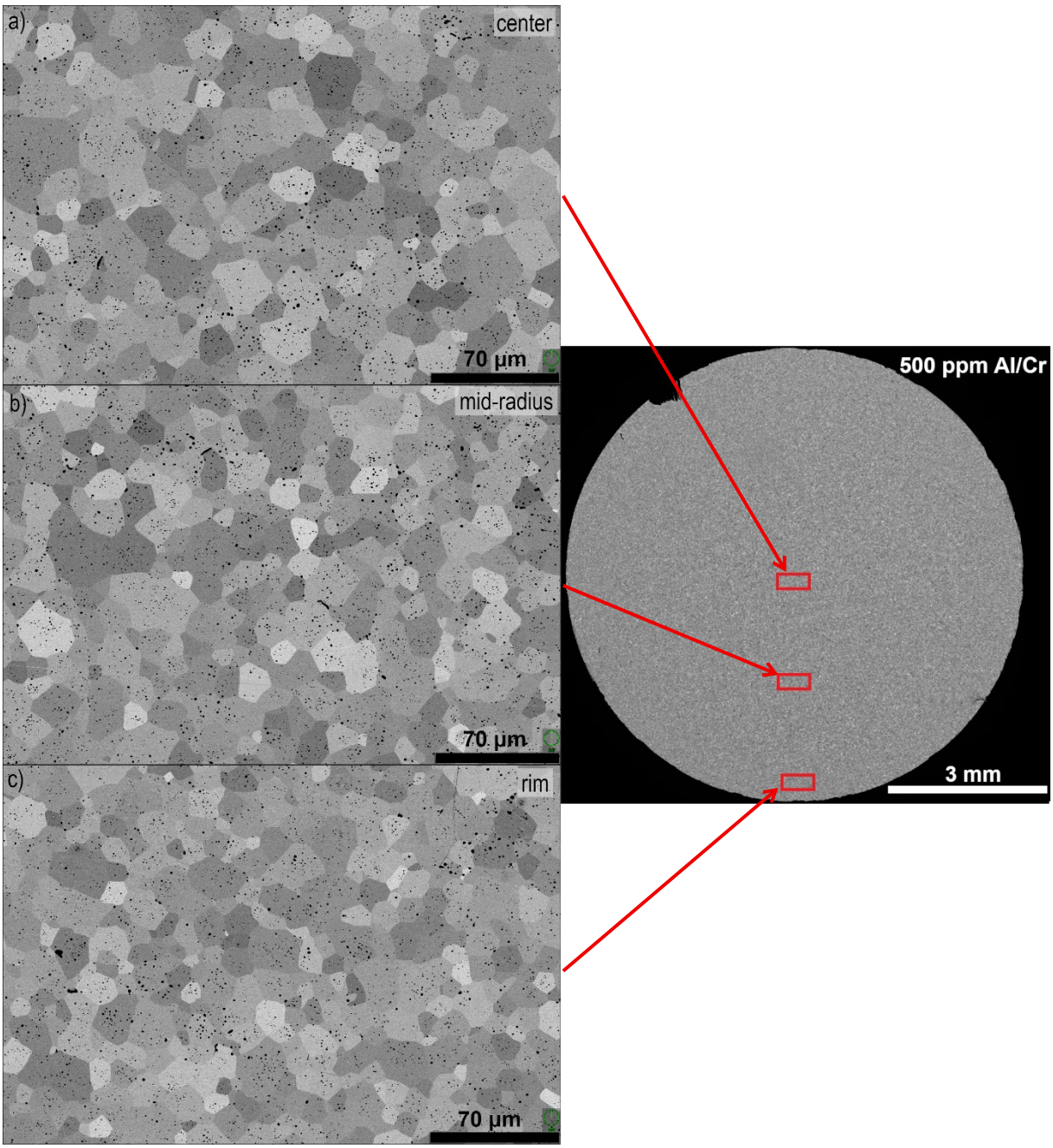

Figure 38 – SEM-SE images of 500 ppm Al/Cr-doped UO_2 pellet with a window width of 300 µm at the (a) centre of the pellet, (b) mid-radius and (c) rim. The green circle at the bottom left of each image shows the alignment, which was the same for all images. The overview image of the pellet is shown as a reference of where the enhanced zoom images were taken.

Inspecting the microstructure of the 1000 ppm Al/Cr-doped UO_2 pellet, shown in Figure 39, reveals an inhomogeneous grain size distribution along its radius, with slightly larger grains in the centre and mid-radius, when compared to its rim. This pellet appears less porous than the pellet doped with 500 ppm of Al/Cr which is consistent with its higher density. Grain sizes seem comparable to the 2000 ppm Cr-doped and the 1000 ppm Al-doped UO_2 samples.

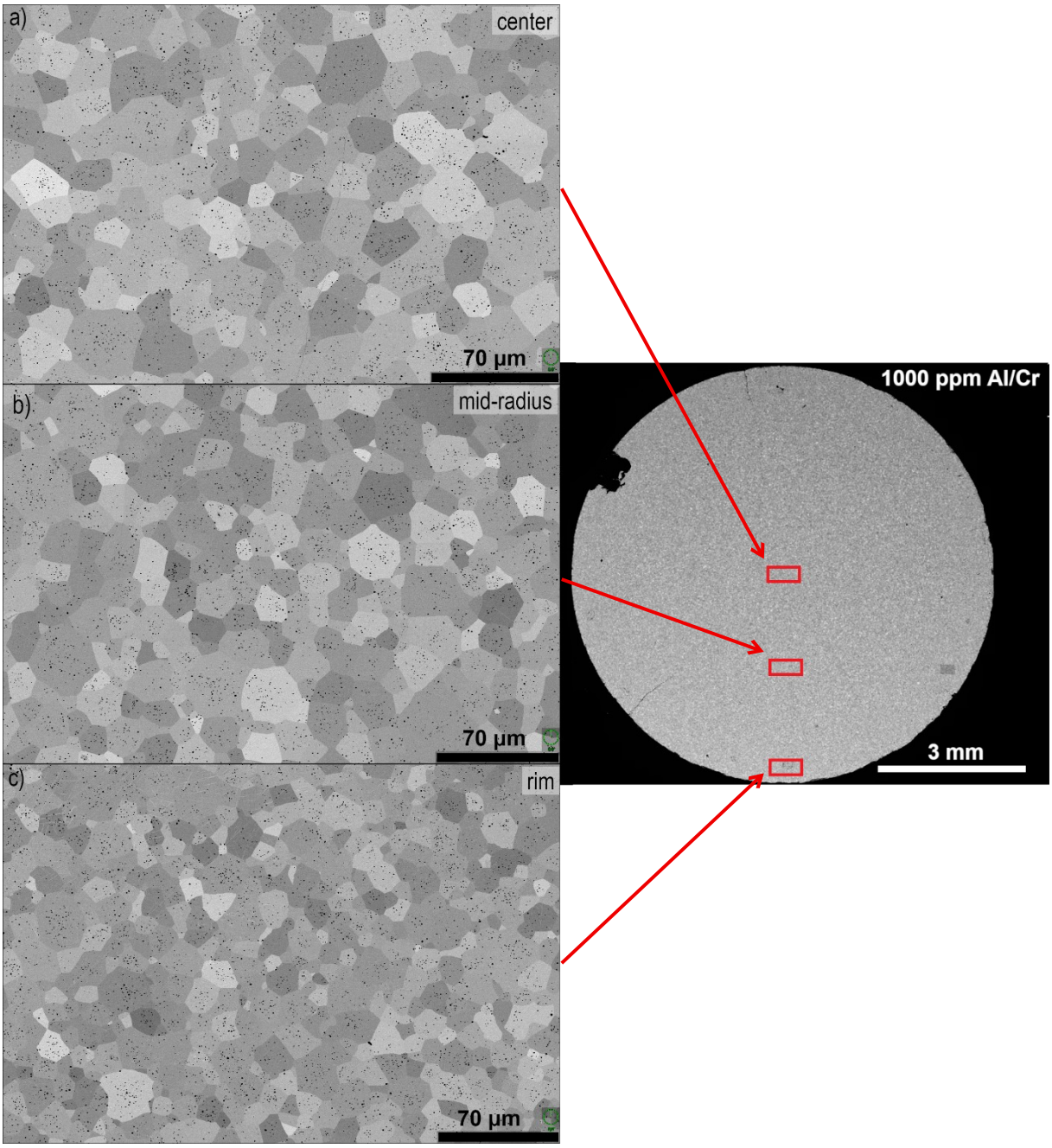

Figure 39 –SEM-SE images of 1000 ppm Al/Cr-doped UO_2 pellet with a window width of 300 µm at the (a) centre of the pellet, (b) mid-radius and (c) rim. The green circle at the bottom left of each image shows the alignment, which was the same for all images. The overview image of the pellet is shown as a reference of where the enhanced zoom images were taken.

A closer inspection of the 2000 ppm Al/Cr-doped UO_2 pellet, shown in Figure 40, reveals larger grains in the centre and mid-radius compared to the 1000 ppm Al/Cr addition. However, grains are much smaller at the rim and around the radial and circular cracks. This effect at the rim is even stronger than for the 2000 ppm Al-doped UO_2 pellet, likely due to the presence of cracks aiding in the volatilization of aluminium. This apparent difference at the rim motivated choosing three different measurement areas for EBSD to quantitatively evaluate the grain size.

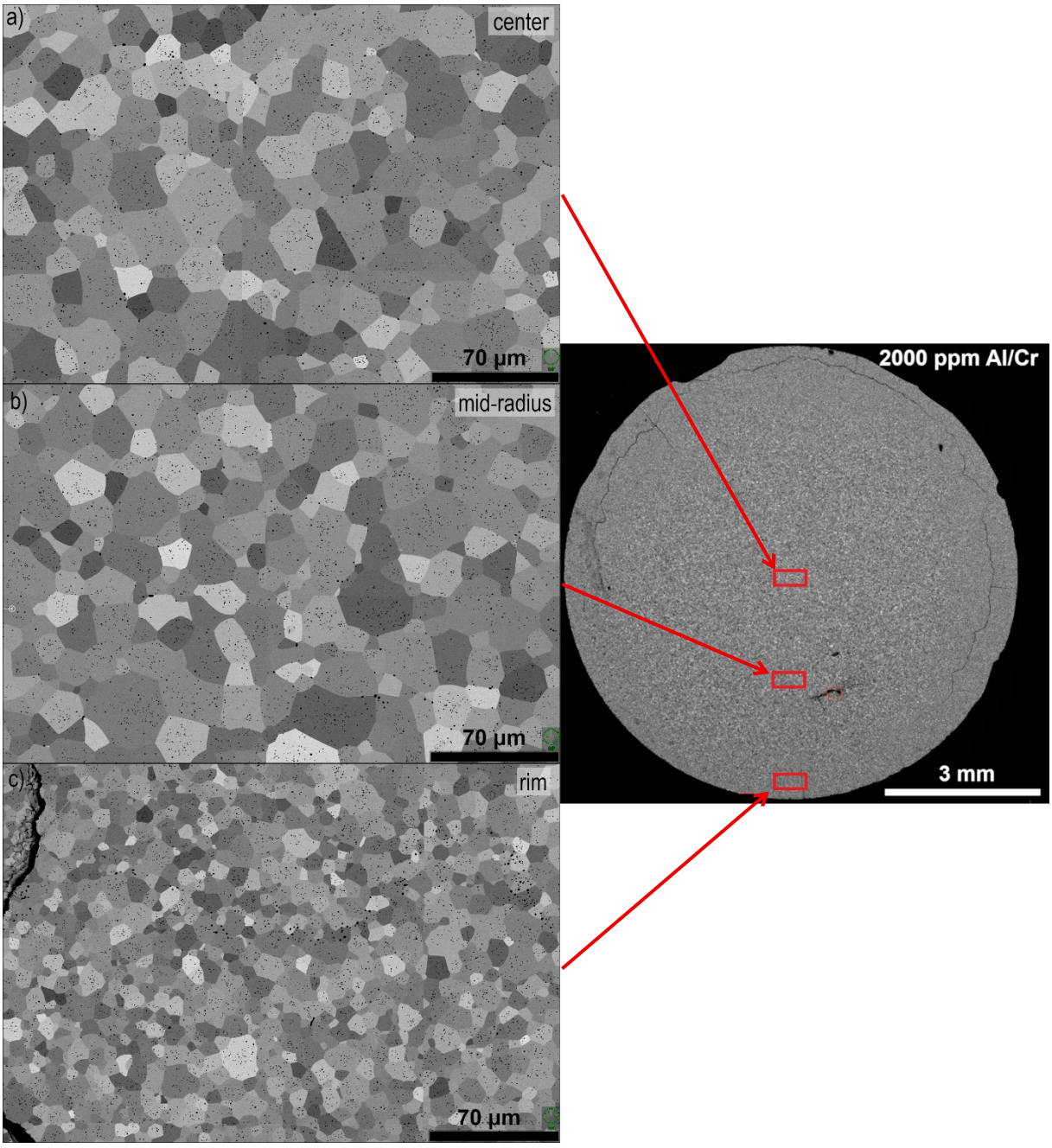

Figure 40 – SEM-SE images of 2000 ppm Al/Cr-doped UO_2 pellets with a window width of 300 µm at the (a) centre of the pellet, (b) mid-radius and (c) rim. The green circle at the bottom left of each image shows the alignment, which was the same for all images. The overview image of the pellet is shown as a reference of where the enhanced zoom images were taken.

5.3. EBSD Analysis

To better quantify the effects seen from the SEM images, EBSD maps were taken of the regions of interest of the samples analysed in the SEM. Regions were chosen according to the results of the SEM images, when differences were observed between rim, mid-radius and centre, EBSD maps of those regions were made. If the sample appeared homogeneous, only a map on the rim was made.

5.3.1. Cr-doped UO_2

Since the size of the grains for the 2000 ppm Cr-doped UO_2 pellet appeared similar irrespective of the position on the pellet, an EBSD map was made only at the rim, which is closer to the detector and so easier to measure. The obtained EBSD map based on crystal orientation for the 2000 ppm Cr-doped UO_2 sample, shown in Figure 41, shows a sample with grains larger than those found on undoped UO_2.

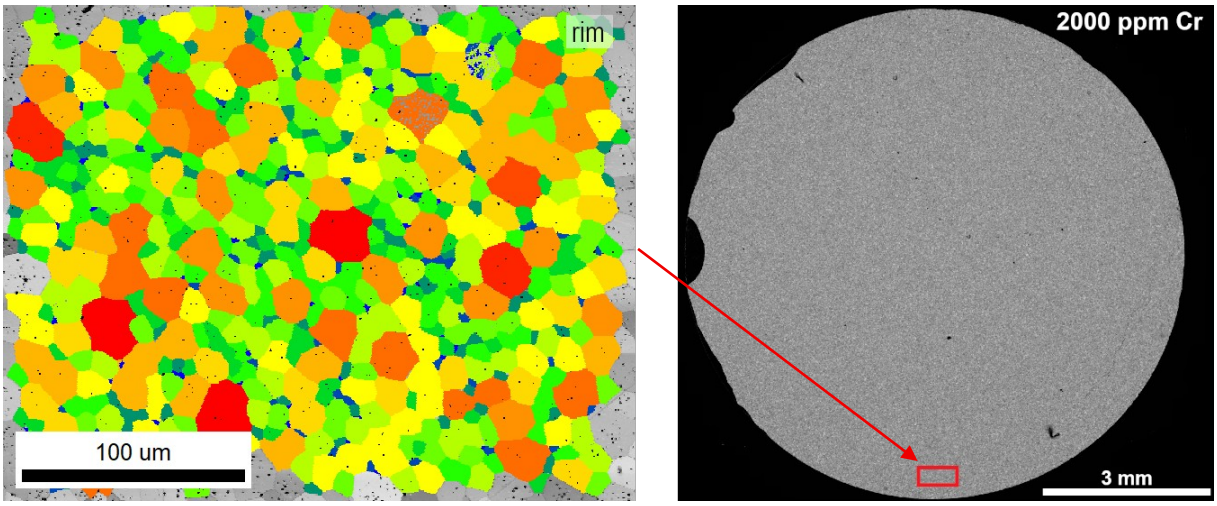

Figure 41 – EBSD map of 2000 ppm Cr-doped UO_2 with colours indicating the size of grains in increasing size from blue, green, yellow, orange and red. Grains at the borders were excluded from the count. Generated with OIM Analysis software.

The result of grain size distribution analysis performed with OIM analysis software by binning the results of grain size based on diameter into 15 bins and showing the area fraction for each bin and excluding grains at the edges, is shown in Figure 42. The sample has grains around 10-15 μm of size, larger than what is observed for undoped UO_2.

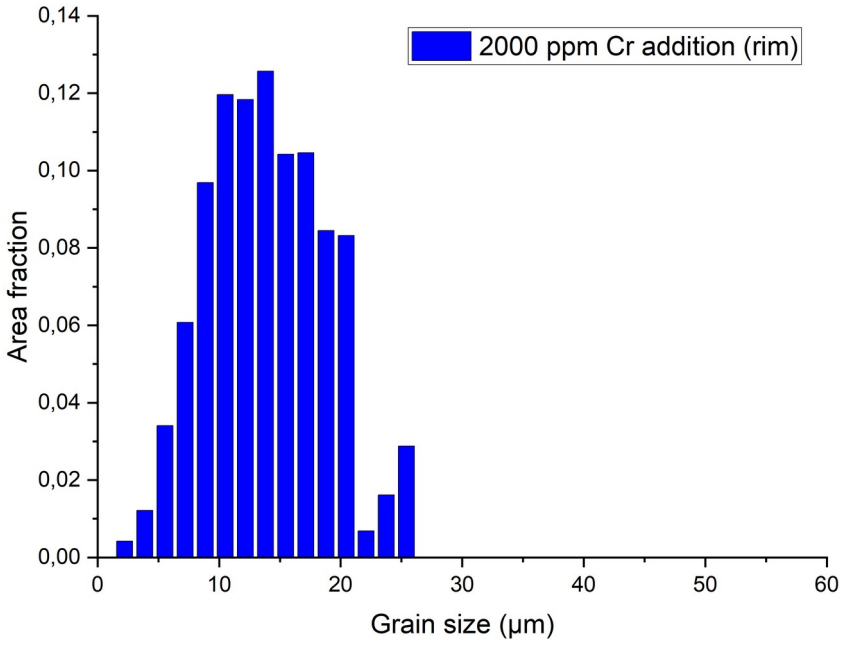

Figure 42 – Grain size distribution histogram for the 2000 ppm Cr-doped UO_2 sample in blue. Area fraction represented by each grain size according to diameter of the grain, binned into 15 bins. Edge grains excluded from the count.

5.3.2. Al-doped UO_2

Again, for this sample, the size of the grains appeared similar irrespective of the position on the pellet, so an EBSD map was made only at the rim. The obtained EBSD map based on crystal orientation for the 1000 ppm Al-doped UO_2 sample, shown in Figure 43, shows smaller grains when compared to the map of the 2000 ppm Al-doped UO_2 sample, shown in Figure 44, which presents bigger grains, especially on the centre of the pellet.

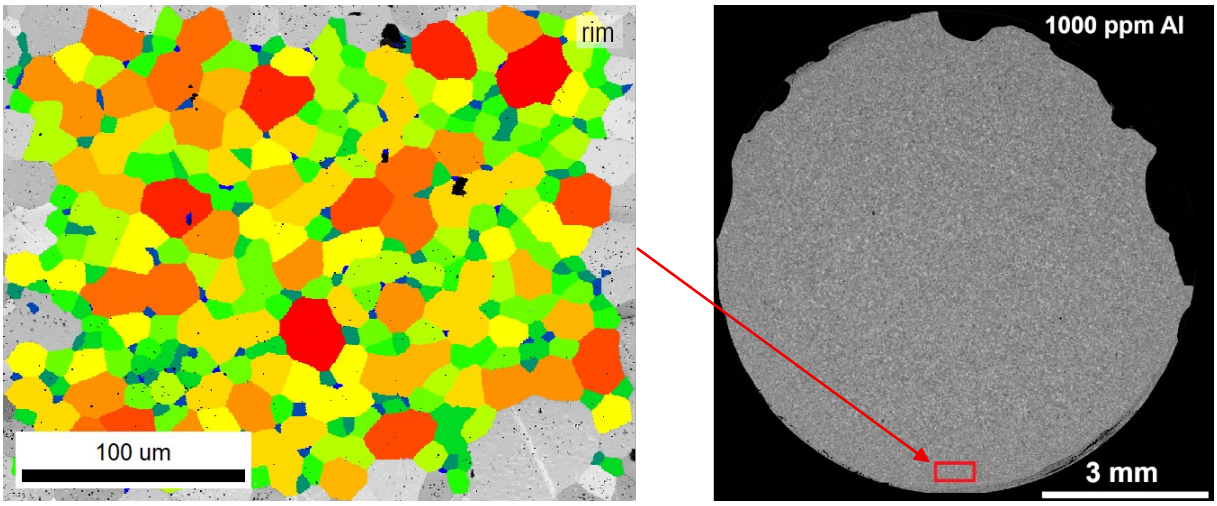

Figure 43 – EBSD map of 1000 ppm Al-doped UO_2 with colours indicating the size of grains in increasing size from blue, green, yellow, orange and red. Grains at the borders were excluded from the count. Generated with OIM Analysis software.

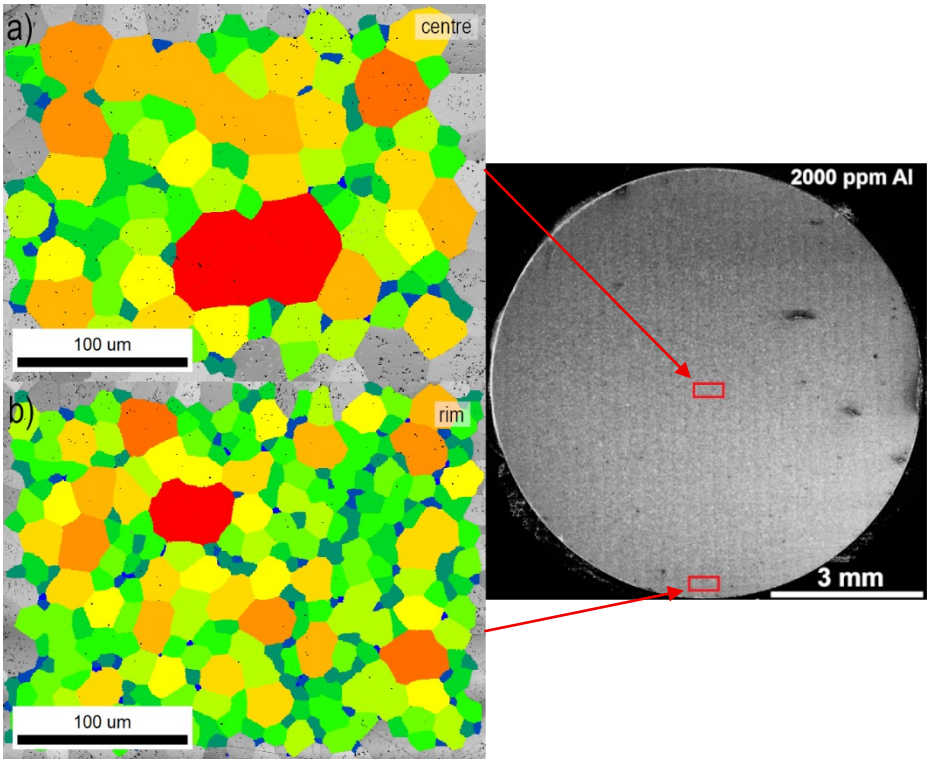

Figure 44 – EBSD map of 2000 ppm Al-doped UO_2 at the (a) centre and (b) rim, with colours indicating the size of grains in increasing size from blue, green, yellow, orange and red. Grains at the borders were excluded from the count. Generated with OIM Analysis software.

The results of grain distribution analysis performed as explained before, for the 1000 ppm Al-doped UO_2 in Figure 45 and for the 2000 ppm Al-doped UO_2 in Figure 46, show the larger grains for the sample with a higher dopant content, demonstrating its effect on grain growth. A clear decrease in grain size to around 15 µm is noticeable at the rim of the 2000 ppm Al-doped UO_2 consistent with the previous qualitative observations.

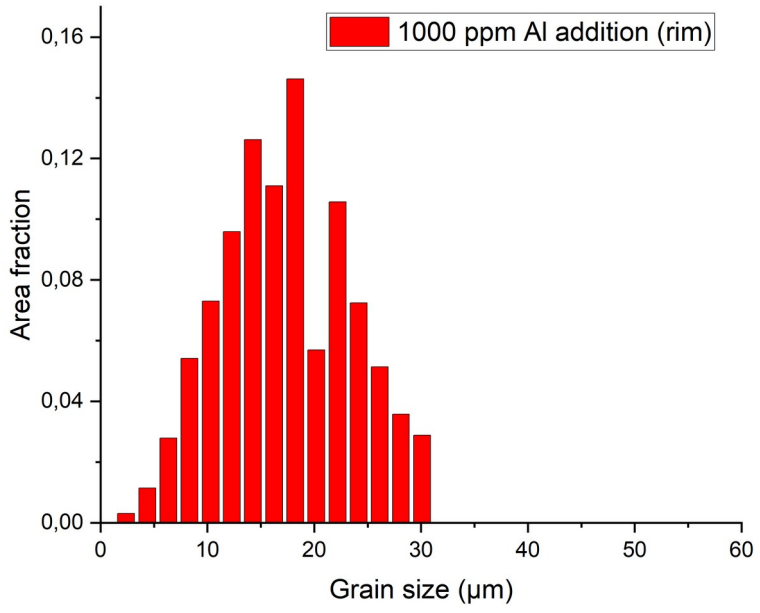

Figure 45 – Grain size distribution histogram for the 1000 ppm Al-doped UO_2 sample. Area fraction represented by each grain size according to diameter of the grain, binned into 15 bins. Edge grains excluded from the count.

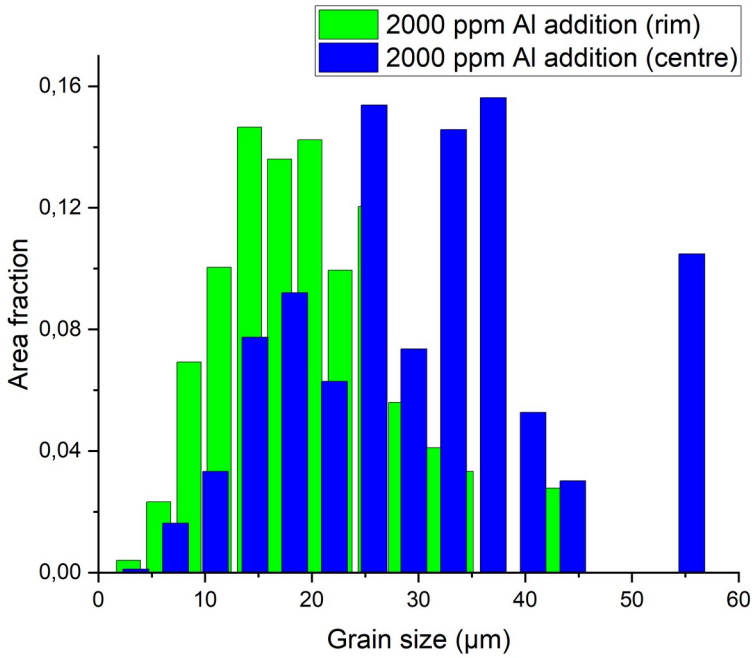

Figure 46 – Grain size distribution histogram for the 2000 ppm Al-doped UO_2 sample at the rim (green) and centre (blue). Area fraction represented by each grain size according to diameter of the grain, binned into 15 bins. Edge grains excluded from the count.

5.3.3. Al/Cr-doped UO_2

The obtained EBSD map based on crystal orientation for the 500 ppm Al/Cr-doped UO_2 pellet, shown in Figure 47, also shows a sample with smaller grains. The map of the 1000 ppm Al/Cr-doped UO_2 sample, shown in Figure 48, reveals slightly larger grains and also the same trend of smaller grains at the rim. Finally, the map of the 2000 ppm Al/Cr-doped UO_2 sample, shown in Figure 49, presents larger grains in the centre and mid-radius, but quite small grains at the rim.

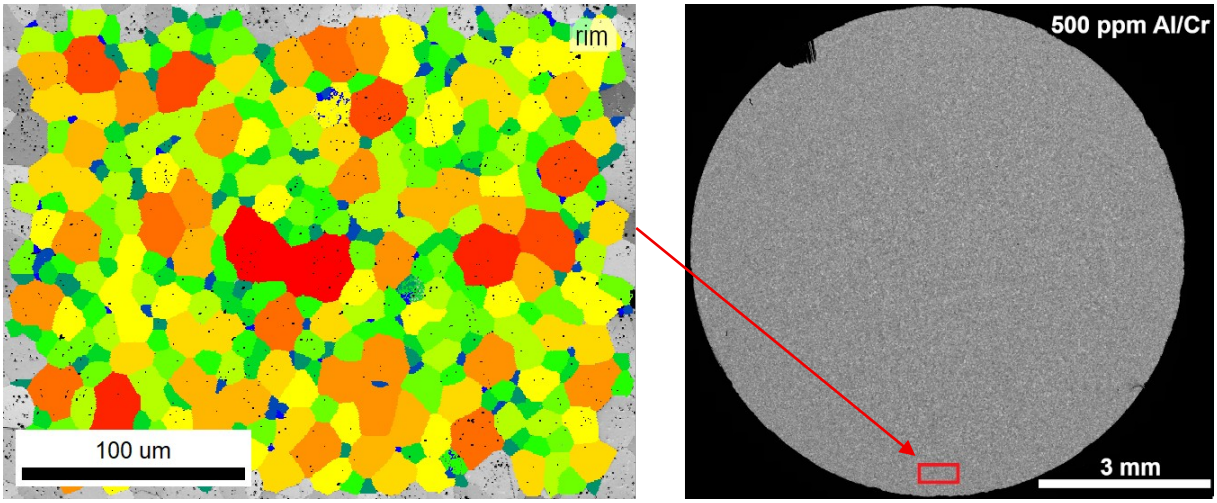

Figure 47 – EBSD map of 500 ppm Al/Cr-doped UO_2 with colours indicating the size of grains in increasing size from blue, green, yellow, orange and red. Grains at the borders were excluded from the count. Generated with OIM Analysis software.

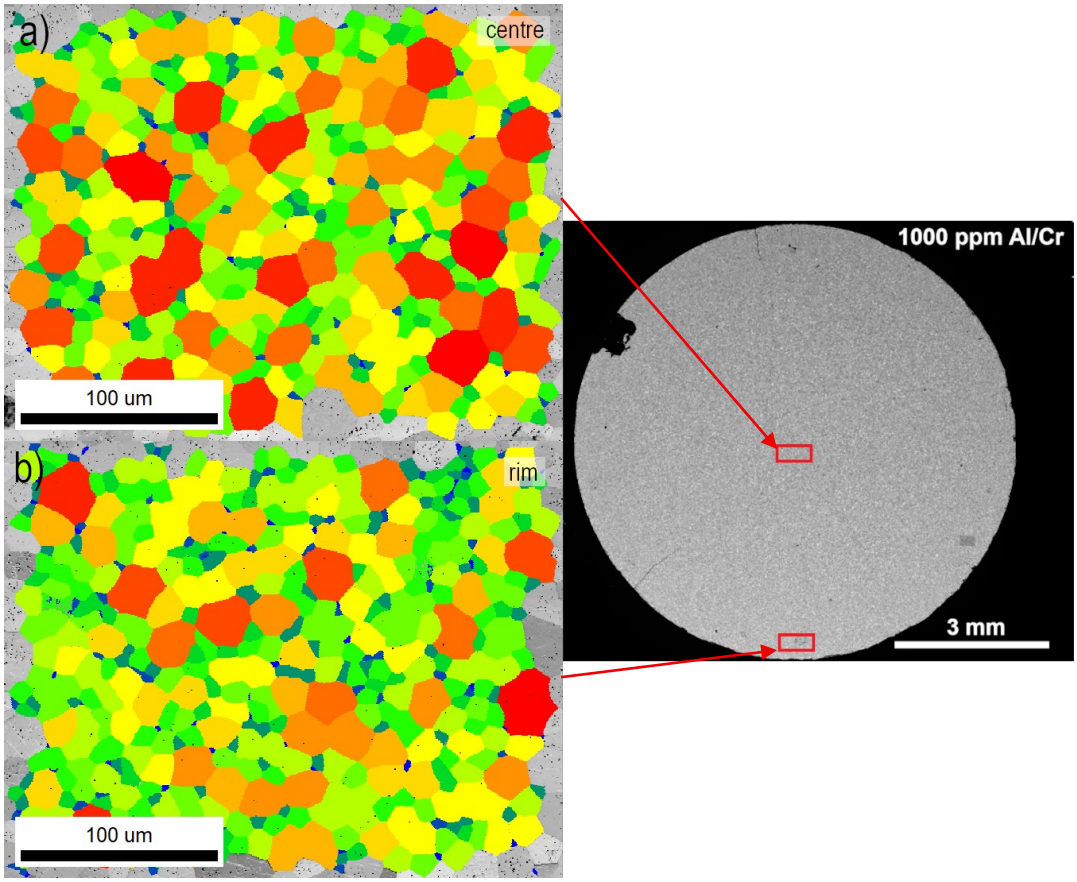

Figure 48 – EBSD map of 1000 ppm Al/Cr-doped UO_2 at the (a) centre and (b) rim, with colours indicating the size of grains in increasing size from blue, green, yellow, orange and red. Grains at the borders were excluded from the count. Generated with OIM Analysis software.

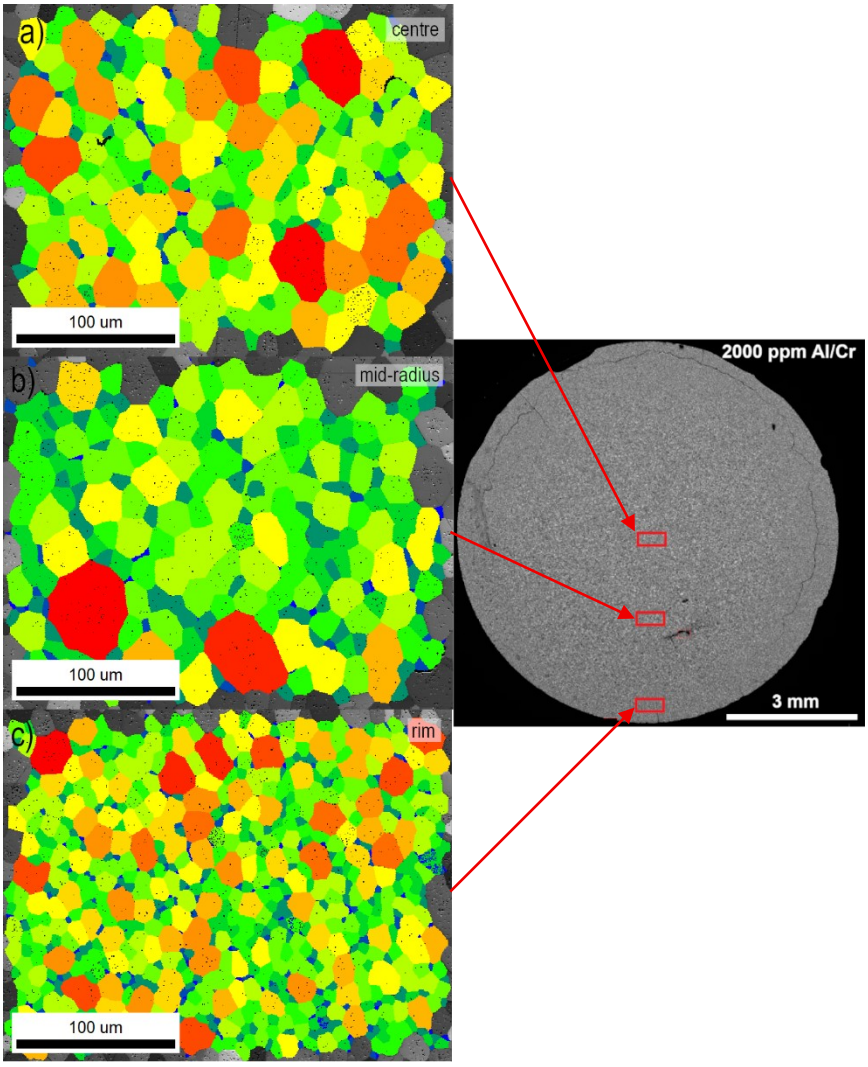

Figure 49 – EBSD map of 2000 ppm Al/Cr-doped UO_2 at the (a) centre, (b) mid-radius and (c) rim, with colours indicating the size of grains in increasing size from blue, green, yellow, orange and red. Grains at the borders were excluded from the count. Generated with OIM Analysis software.

The results of grain size distribution analysis performed as described before, shown for the 500 ppm Al/Cr-doped UO_2 in Figure 47 and for the 1000 ppm Al/Cr-doped UO_2 in Figure 48, show a similar result for 500 ppm and 1000 ppm of Al/Cr-doping with grains of an average size around 15 µm. For the 2000 ppm Al/Cr-doped UO_2 in Figure 49, we see that at the centre and mid-radius of the pellet even larger grains are obtained, with an average size of 20 µm. However, at its rim grains with only an average size of 10 µm are present.

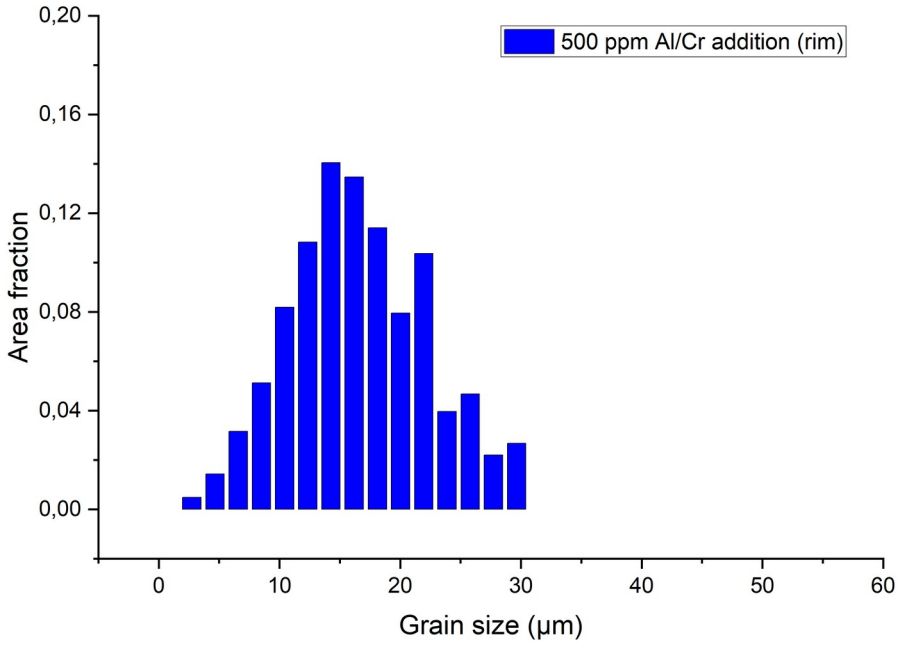

Figure 50 – Grain size distribution histogram for the 500 ppm Al/Cr-doped UO_2 sample. Area fraction represented by each grain size according to diameter of the grain, binned into 15 bins. Edge grains excluded from the count.

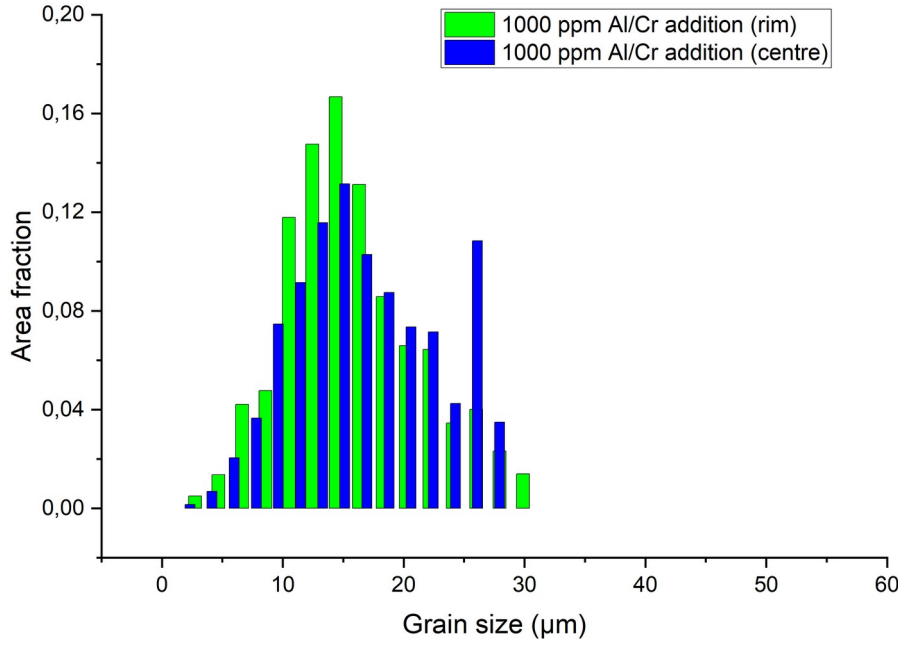

Figure 51 – Grain size distribution histogram for the 1000 ppm Al/Cr-doped UO_2 sample at the rim (green) and centre (blue). Area fraction represented by each grain size according to diameter of the grain, binned into 15 bins. Edge grains excluded from the count.

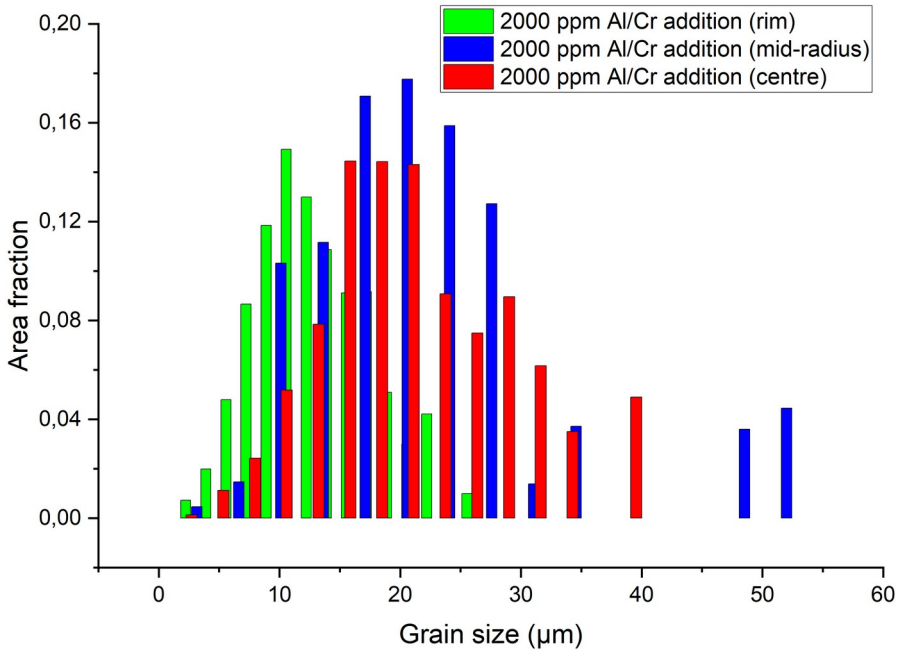

Figure 52 – Grain size distribution histogram for the 2000 ppm Al/Cr-doped UO_2 sample at the rim (green), mid-radius (blue and centre (red). Area fraction represented by each grain size according to diameter of the grain, binned into 15 bins. Edge grains excluded from the count.

The summary of the results of grain size distribution for all samples is shown in Table 5, at the centre of the UO_2 pellet with 2000 ppm Al-doping the highest average grain size was found. For the UO_2 pellet with 2000 ppm Al/Cr-doping the second highest average grain size was observed at the centre and mid-radius, however at its rim the lowest average grain size was observed. It is surprising that the Cr-doped UO_2 sample did not have the largest grain size, however it might be that in this case not enough Cr was added to achieve the formation of a eutectic phase and further increase grain sizes. Other studies use higher amounts of Cr and achieve even larger grain sizes. On the other hand, for the Al-doped UO_2 samples the 2000 ppm addition already seems to reach the saturation incorporation.

Table 5 – Area weighted average grain size distribution for all samples which underwent EBSD analysis. The results of the samples with 2000 ppm doping of Al, Al/Cr and Cr are highlighted. In addition, the grain size for a reference undoped UO_2 pellet is presented on the last line.

Sample	Position	Grain size Area average (μm)
1000 ppm Al-doped	rim*	17.33 ± 6.02
2000 ppm Al-doped	centre	31.07 ± 12.46
2000 ppm Al-doped	rim	19.60 ± 8.03
500 ppm Al/Cr-doped	rim*	16.55 ± 5.80
1000 ppm Al/Cr-doped	centre	17.07 ± 5.90
1000 ppm Al/Cr-doped	rim	15.67 ± 5.64
2000 ppm Al/Cr-doped	centre	21.73 ± 7.90
2000 ppm Al/Cr-doped	mid-radius	22.42 ± 10.67
2000 ppm Al/Cr-doped	rim	12.89 ± 4.88
2000 ppm Cr-doped	rim*	13.96 ± 4.92
undoped UO_2 [49]	-	5.0

*rim, centre and mid-radius all present equally from SEM observation

5.4. Discussion

The grain growth effect of Al, Al/Cr and Cr doping on UO_2 pellets was quantified. For Al-doping, an increase in grain size was observed, but this effect was lessened at the rim. A similar effect was observed in the Al/Cr-doped UO_2 pellets, an increase in the dopant amount resulted in increased grain size, but this effect was noticeably decreased at the rim. This reduced grain size effect at the rim was not observed for the Cr-doped UO_2 pellet.

These differences can be explained by the lower solubility of Al in the UO_2 matrix compared to Cr [59, 67], which means the solubility limit is exceeded for Al and Al/Cr in the samples with higher doping, as discussed in Chapter 4. This allows eutectics and the formation of incongruent melting between grains in the case of Al/Cr as shown in Figure 10 and precipitates to form in the grain boundaries to activate the mechanism for grain growth. In contrast, in the Cr-doped sample, the addition is below the solubility limit meaning that there is not enough chromium to form a eutectic and promote grain growth. Another factor is the lower melting point of Al_2O_3 compared to Cr_2O_3 [88], which means it is more susceptible to volatilization during sintering. This effect is even stronger for Al/Cr-doped UO_2 pellets, with a stronger decrease in grain size and cracks at the rim.

This can be explained by the fact that the more soluble and stable Cr^{3+} ions could displace the Al^{3+} ions from the UO_2 matrix, making them more available to volatize.

Volatilization depends on the diffusion of Al to the surface of the pellet in sintering conditions, so it follows that this effect is more pronounced on the rim of the pellet as the polishing removes enough material that the inner surface of the pellet is revealed.

These effects are important for the application of nuclear fuels such the Al/Cr-doped ADOPT fuels and their handling as SNF. A concentration of smaller grains due to volatilization of Al on the rim of pellets could mean that the beneficial effect that increased grain size has of reducing fission gas release is reduced on the region of the pellet where the majority of the fission happens. The presence of smaller grains means an increased surface area, which is detrimental in case the fuel gets in contact with water due to dissolution and increased reaction surface in SNF conditions or breaching of cladding.

With respect to literature, where in most studies inhomogeneous grain sizes in materials are not considered, this appears to be the first study that has systematically examined Al, Al/Cr and Cr doping of UO_2 and demonstrates the need for detailed studies on these materials especially considering how impactful the radial difference in grain size appears in Al-doped UO_2 pellets. Although the eutectic dopant additions of Al to UO_2 can bring beneficial properties, they can also be detrimental by creating a region of smaller grains at the rim with a higher surface area for chemical attack.

6. Mechanical Properties

6.1. Introduction

The mechanical properties of nuclear fuel play in important role in reactor operation because of pellet-cladding interaction effects and also in SNF conditions [26]. A comparative study of these properties for Al, Al/Cr and Cr-doped UO_2 pellets produced with an established technique is not present in literature. In this chapter, the results of density measurements by the Archimedes method and the evaluation of mechanical properties (microhardness, H_v and fracture toughness K_{1C}) by Vicker's indentation of UO_2 samples doped with Al, Al/Cr and Cr are presented. The implications of these properties on nuclear fuel and SNF behaviour and their relation to the microstructural properties are discussed.

6.2. Pellet Density

6.2.1. Green Density

The green density of the pellets was calculated using the geometrical method, as explained in 2.4. A similar trend is observed in the green density of pellets with both dopant types, where there is a decrease in it with the addition of the dopant. For the Al-doped UO_2 pellets, shown in Figure 53, a stable value around 61% of the TD is reached after the first 500 ppm addition. For the Al/Cr-doped UO_2 pellets, shown in Figure 54, the decrease is more gradual and a stable value around 61% of the TD is reached only at an addition of 1500 ppm. This decrease in green density with the addition of dopants is consistent with literature [46].

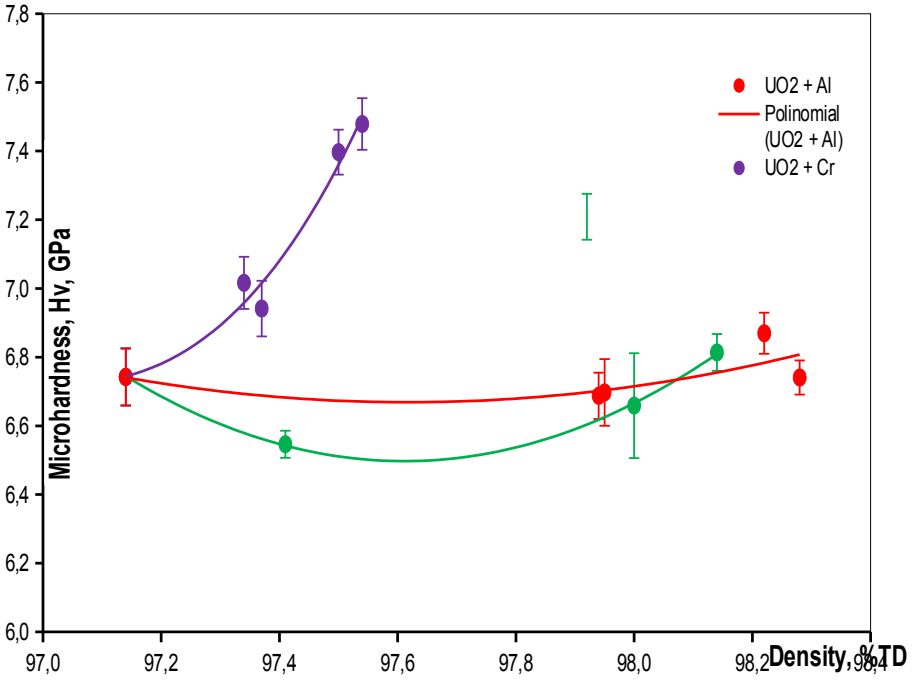

Figure 53 – Green density of Al-doped UO_2 pellets as a function of dopant content. A second order polynomial was added to better show the trend in the data.

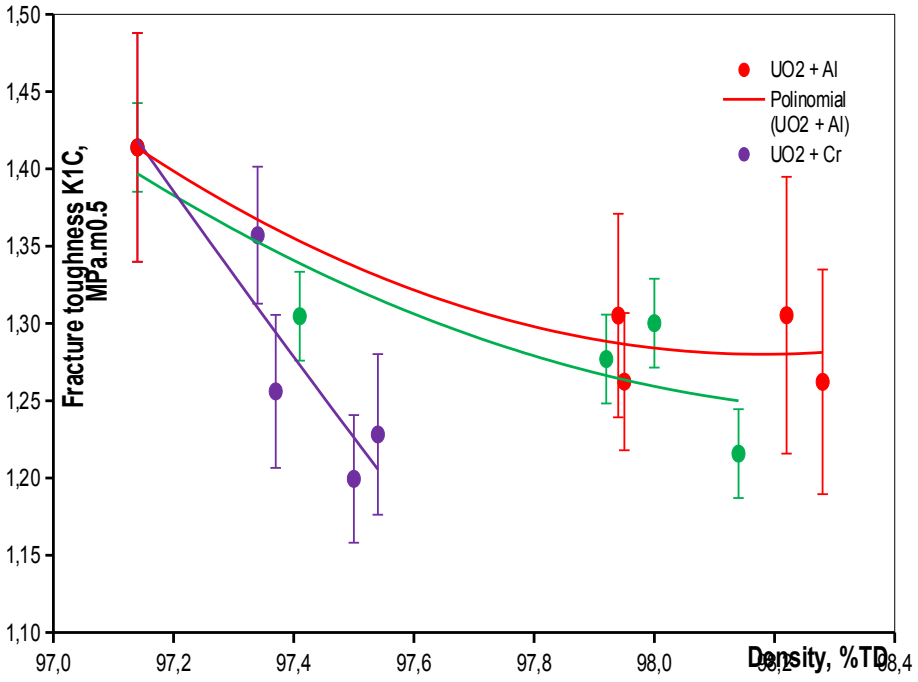

Figure 54 – Green density of Al/Cr-doped UO_2 pellets as a function of dopant content. A second order polynomial was added to better show the trend in the data.

A study of the green pellets for Cr-doped UO_2 was not possible as those pellets were fabricated before the start of this master thesis. Only their sintered properties were analysed here.

6.2.2. Sintered Densities

With the measured masses of each pellet from the modified Archimedes method, explained in the Materials and Methods chapter, the density of the sintered pellets considering closed porosity, ρ_{s1}, and total porosity, ρ_{s2}, are calculated.

Observing the obtained densities, considering total porosity, shown in Figure 55, for the Al-doped UO_2 pellets the addition of the dopant resulted in increased densities up to 98.3% of the TD with 1500 ppm addition and stabilizing on that value. For the Al/Cr-doped UO_2 pellets no increase is observed up to 500 ppm addition, then their density increases to around 98.1% of the TD at 1000 ppm addition, lower than the Al-doped pellets, and stays constant. The Cr-doped UO_2 pellets show the lowest densities, with a maximum around 1000 to 1500 ppm addition of 97.5% of the TD and then a lower density for the 2000 ppm addition.

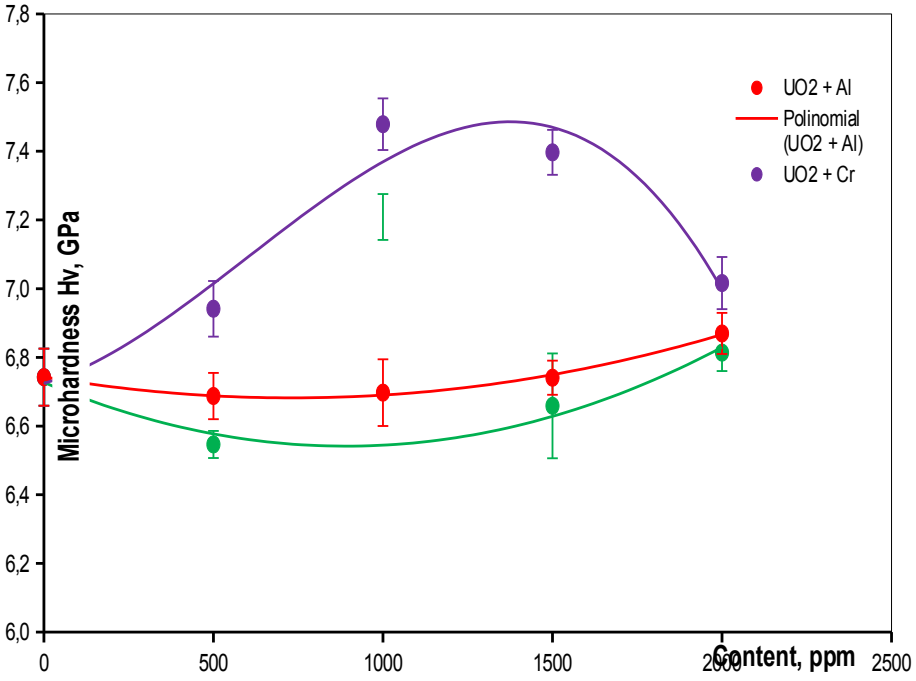

Figure 55 – Sintered density, considering total porosity, of Al-doped UO_2 pellets (blue), Al/Cr-doped UO_2 pellets (red) and Cr-doped UO_2 pellets (green) as a function of the dopant content. A second order polynomial was added to better show the trend in the data.

By analysing the fraction of open and closed porosity, the samples have a constant low value of open porosity of 0.23(5)% for Al-doped UO_2 pellets, shown in Figure 56, of 0.28(5)% for Al/Cr-doped UO_2 pellets, shown in Figure 57, and of 0.24(3)% for Cr-doped UO_2 pellets, shown in Figure 58. In most cases the dopant addition resulted in a reduction of the fraction of closed porosity, except for the 2000 ppm Cr addition which led to an increase in porosity. In general, all pellets present a low amount of open porosity.

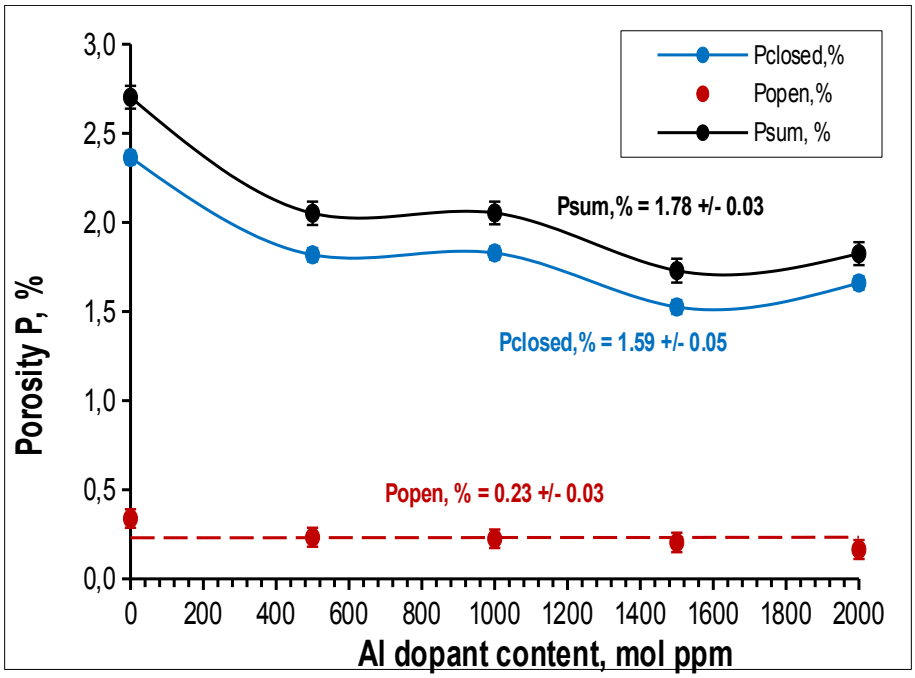

Figure 56 – Evolution of the fraction of total porosity (black), closed porosity (blue) and open porosity (red) as a function of dopant content for Al-doped UO_2 pellets. The dashed red line represents the average value of open porosity.

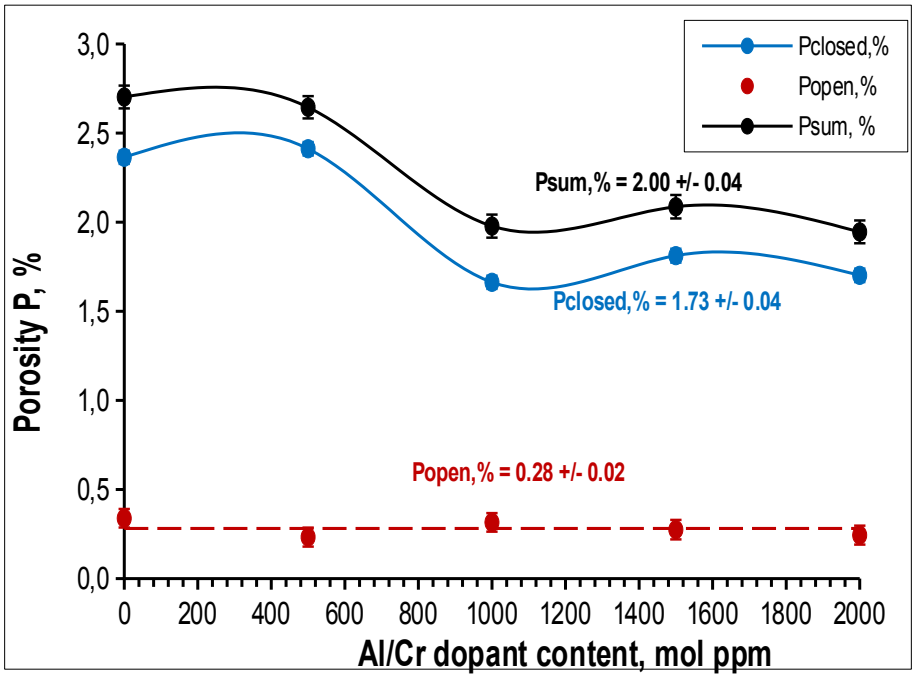

Figure 57 – Evolution of the fraction of total porosity (black), closed porosity (blue) and open porosity (red) as a function of dopant content for Al/Cr-doped UO_2 pellets. The dashed red line represents the average value of open porosity.

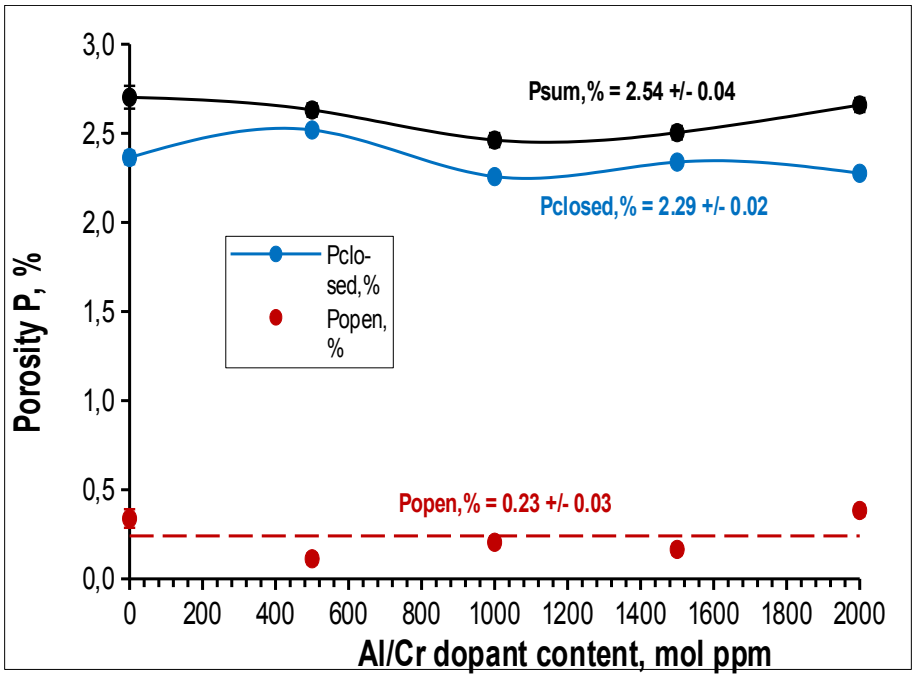

Figure 58 – Evolution of the fraction of total porosity (black), closed porosity (blue) and open porosity (red) as a function of dopant content for Cr-doped UO_2 pellets. The dashed red line represents the average value of open porosity.

The obtained experimental values for each Al-doped, Al/Cr-doped and Cr-doped UO_2 pellets can be found in Table 6, Table 7 and Table 8, respectively.

Table 6 – Experimental values of green density, sintered density with total porosity and the open and closed porosity of Al-doped UO_2 pellets.

Al, mol ppm	ρ_g, %TD	ρ_{s1}, %TD	ρ_{s2}, %TD	P_{sum}, %	P_{open}, %	P_{closed}, %
0	64.16(43)	97.64(4)	97.30(4)	2.70(6)	0.34(5)	2.36(4)
500	61.44(4)	98.18(4)	97.95(4)	2.05(7)	0.23(5)	1.82(4)
1000	61.67(10)	98.17(4)	97.95(4)	2.05(6)	0.22(5)	1.83(4)
1500	60.54(27)	98.47(4)	98.27(4)	1.73(7)	0.20(5)	1.53(4)
2000	60.97(13)	98.34(4)	98.18(4)	1.82(6)	0.16(5)	1.66(4)

Table 7 – Experimental values of green density, sintered density with total porosity and the open and closed porosity of Al/Cr-doped UO_2 pellets.

Al/Cr, mol ppm	ρ_g, %TD	ρ_{s1}, %TD	ρ_{s2}, %TD	P_{sum}, %	P_{open}, %	P_{closed}, %
0	64.16(43)	97.64(4)	97.30(4)	2.70(6)	0.34(5)	2.36(4)
500	62.87(9)	97.59(4)	97.36(4)	2.64(6)	0.23(5)	2.41(4)
1000	61.53(6)	98.34(4)	98.02(4)	1.98(6)	0.32(5)	1.66(4)
1500	60.90(9)	98.19(4)	97.91(4)	2.09(7)	0.27(5)	1.81(4)
2000	61.01(2)	98.30(4)	98.05(4)	1.95(6)	0.24(5)	1.70(4)

Table 8 – Experimental values of sintered density with total porosity and the open and closed porosity of Cr-doped UO_2 pellets.

Cr, mol ppm	ρ_g, %TD	ρ_{s1}, %TD	ρ_{s2}, %TD	P_{sum}, %	P_{open}, %	P_{closed}, %
0	-	97.64(4)	97.30(4)	2.70(6)	0.34(5)	2.36(4)
500	-	97.48(2)	97.37(2)	2.63(4)	0.11(3)	2.52(2)
1000	-	97.74(2)	97.54(2)	2.46(4)	0.20(3)	2.26(2)
1500	-	97.66(2)	97.50(2)	2.50(4)	0.16(3)	2.34(2)
2000	-	97.72(2)	97.34(2)	2.66(4)	0.38(3)	2.28(2)

6.3. Microhardness and Fracture Toughness

6.3.1. Crack Formation Mechanisms

Microhardness and fracture toughness are important strength characteristics of ceramics, as they relate to the behaviour of the material under stress. Microhardness is the reaction of the material to the indentation of a special indenter. In our case, this is a Vicker's Indentation with a diamond pyramid, the microhardness is calculated using equation (20), where *P* is the indentation load and *d* is the size of the indent. The type of indent produced, which can be seen in Figure 59, is then analysed in image treatment software to measure the size of the indent and the length of the cracks according to Figure 60. Their size on the digital image is then compared to a standard to calculate the actual size.

$$H_v = \frac{0.1891 \cdot P}{d^2} \tag{20}$$

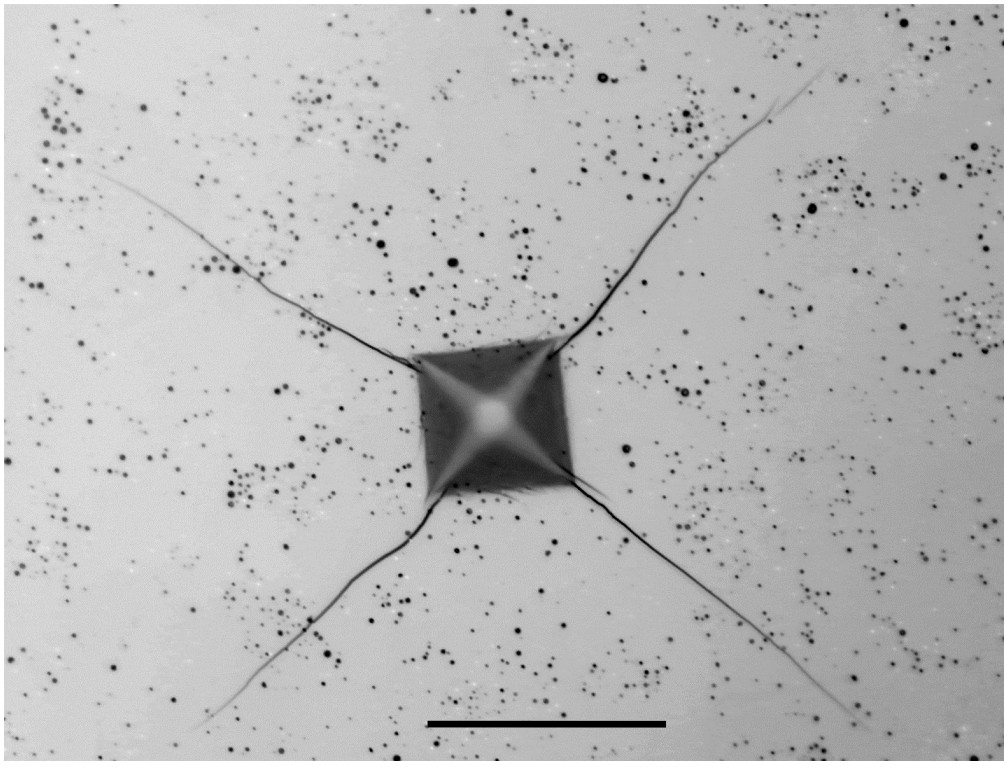

Figure 59 – Representative photograph of a Vicker's indent on a 1500 ppm Al-doped UO_2 sample using an optical microscope at 500x magnification. A square indenter mark can be seen in the middle of the picture and cracks extend outwards starting at the indentation's diagonals.

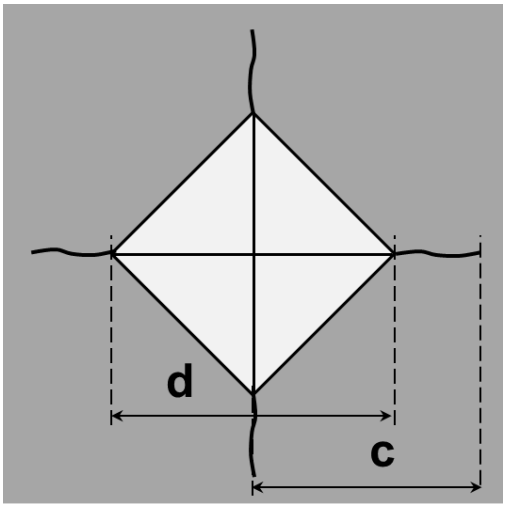

Figure 60 – Schematic representation of the measurements taken from the indentation image.

Evaluation of the fracture toughness is an important parameter for the prediction of mechanical performance of materials. Hardness indentation can be used to obtain Mode I critical stress intensity factor K_{1C}. This method is based on the measurement of the length of cracks formed around the indent when a critical load for the formation of cracks is exceeded. The most adequate equation to be used depends on the type of crack that is formed. For median or half-penny cracks, shown in Figure 61, which completely surround the indentation, the Evans and Charles equation (21) provides a good fit. However, for low crack to indent ratios in reasonably tough materials, only Palmqvist cracks which are formed at the end of the diagonals of the indentation are present, the two types of cracks are shown in Figure 61.

$$K_{1C} = 0.067\, H_V \sqrt{0.5\,d} \left(\frac{E}{H_V}\right)^{0.4} \left(\frac{c}{0.5\,d}\right)^{-1.5} \quad (21)$$

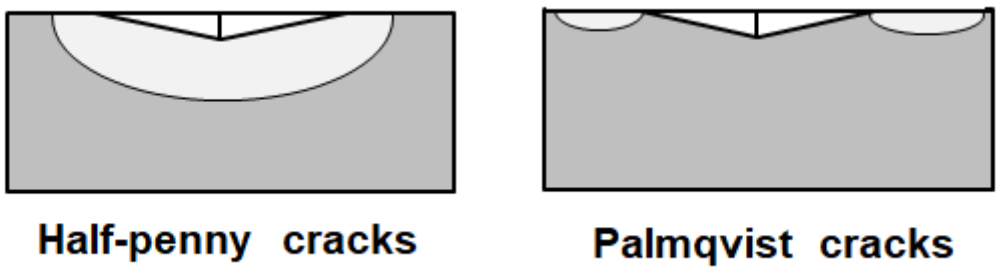

Figure 61 – Schematic representation of half-penny and Palmqvist cracks.

Observing the type of crack produced in the samples, shown in Figure 62, it is clear that Palmqvist cracks are formed. The cracks start precisely at the corner of the indenter, indicated by the red arrow and the type of material damage of chipping between the cracks is also typical of this type of crack. The fracture toughness is then, better

described by the Niihara equation (22), where *E* is Young's Module which for UO_2 a value of 223 GPa was used and *c* is the crack length [89, 90].

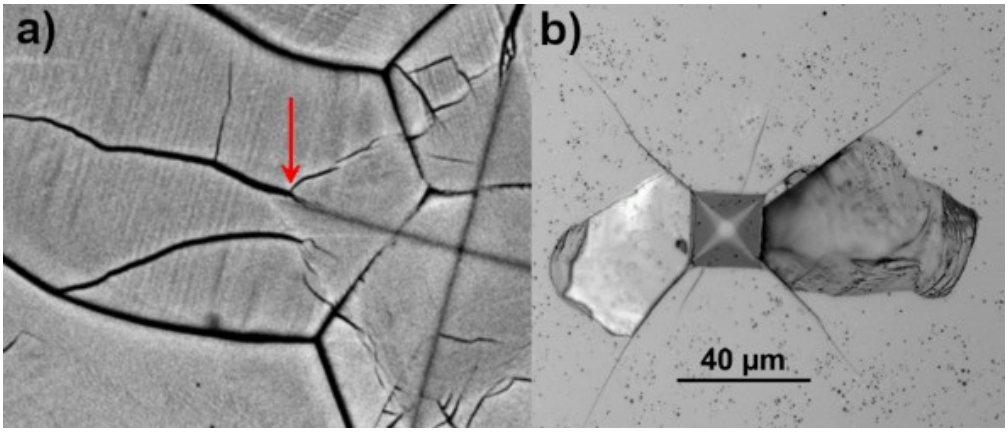

Figure 62 – (a) SEM image of an indent of an undoped UO_2 pellet showing the crack formation originating from the corner at the diagonal of the indenter. (b) Optical microscope image of an indent of a 1000 ppm Al/Cr-doped UO_2 pellet showing chipping originating from the corners of the indent. Both phenomena are typical of Palmqvist cracks.

$$K_{1C} = 0.018\, H_V \sqrt{0.5\,d} \left(\frac{E}{H_V} \right)^{2/5} \left(\frac{c}{0.5\,d} - 1 \right)^{3/2} \tag{22}$$

6.3.2. Loading Force Dependence

However, when measuring microhardness deviations are observed depending on the load applied. At very low loads stray maxima in hardness may be observed and at very high loads crack formation and subsurface chipping can occur [91]. Evaluation of the microhardness was first analysed for a single sample using increasing indentation pressures to determine the ideal indentation load as can be seen in Figure 63. With increasing load, both the indenter size and the crack length increases.

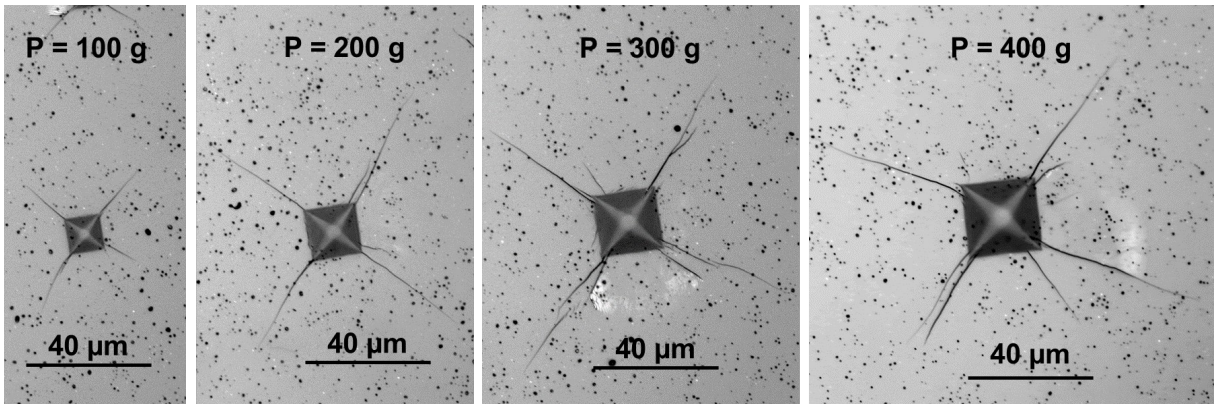

Figure 63 – Indentation of a 1000 ppm Cr-doped UO_2 pellet with increasing loads. As the load increases the indentation size increases, more cracks are formed, and chipping starts to occur.

By analysing the results of the calculated microhardness as a function of the loading force, shown in Figure 64, a tendency towards stabilization can be observed at higher loads. Moreover, observing the evolution of the standard deviation of the microhardness as a function of the loading force, calculated based on the seven indentations made at

each loading force, shown in Figure 65, lower values are obtained for higher loads. Finally, the calculated fracture toughness as a function of the loading force, shown in Figure 66, also shows stabilization at higher loads. Therefore, the loading force of 400 gf was chosen for this work.

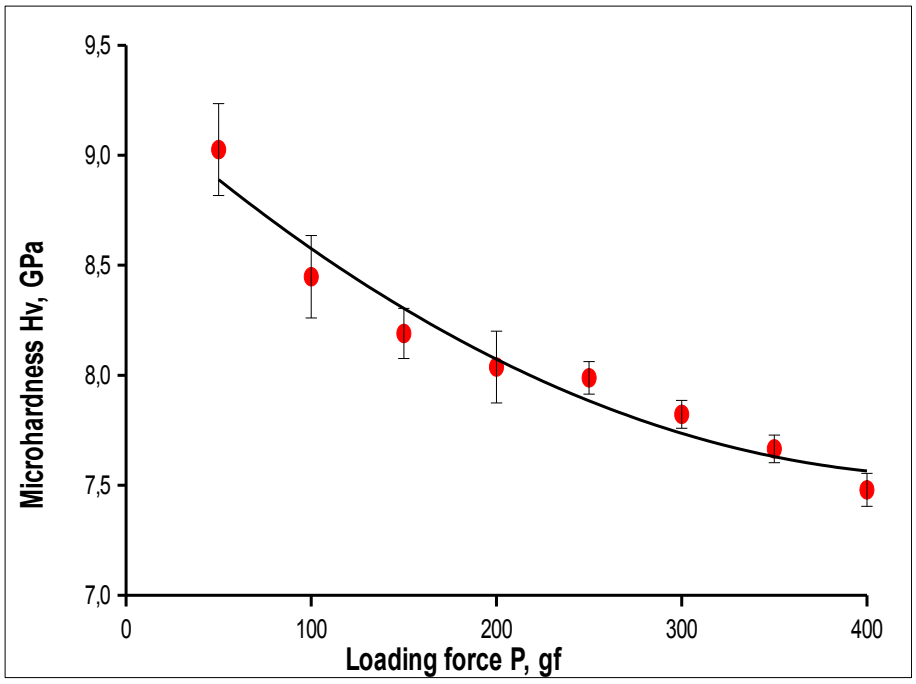

Figure 64 – Graph of the microhardness as a function of the loading force for the 1000 ppm Cr-doped UO_2. A polynomial fit of the second order was added to the data points.

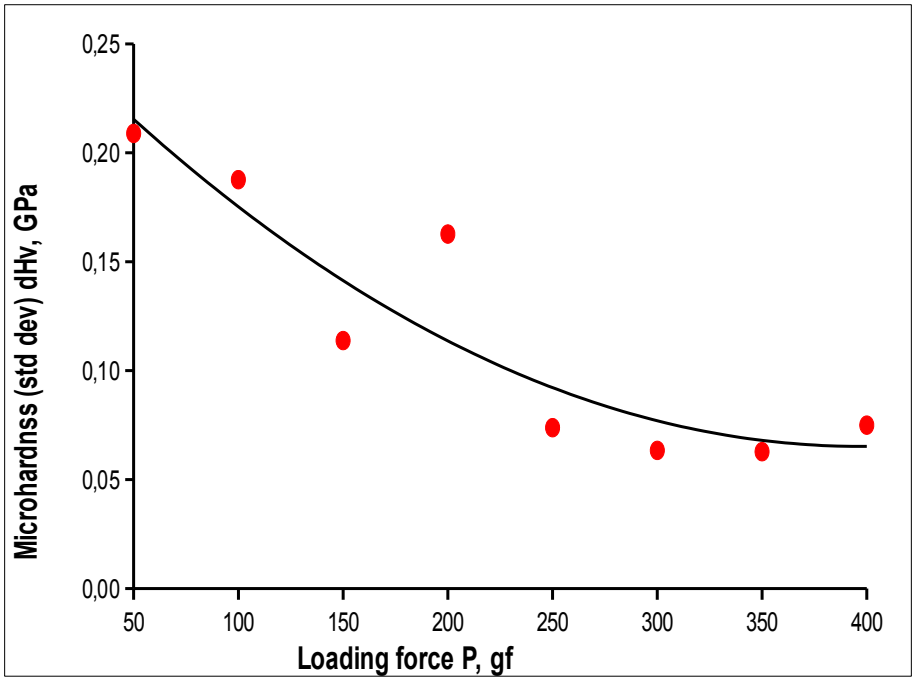

Figure 65 – Graph of the standard deviation of the microhardness value as a function of the loading force for the 1000 ppm Cr-doped UO_2. A polynomial fit of the second order was added to the data points.

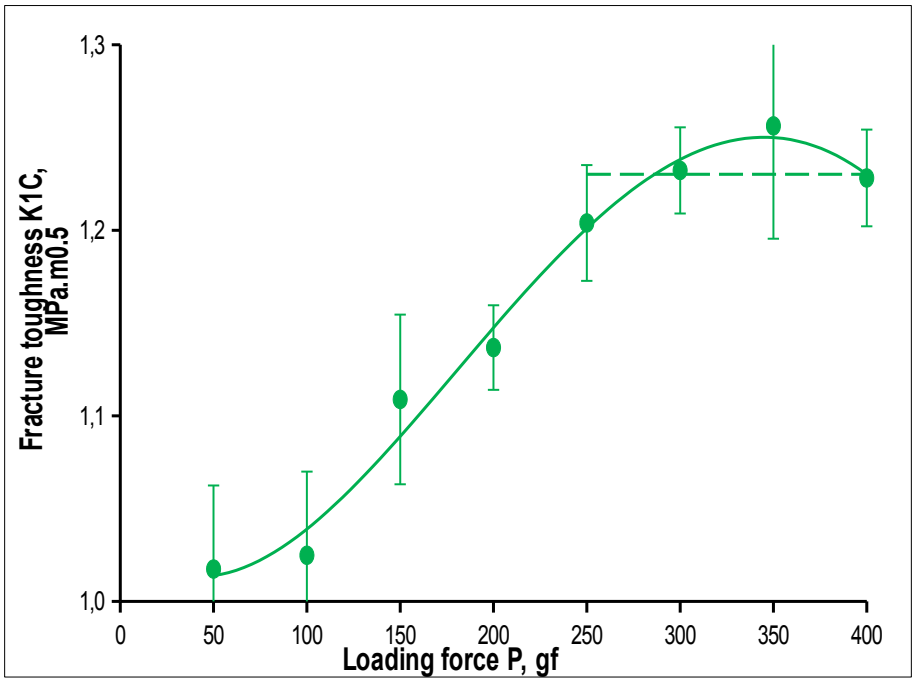

Figure 66 – Graph of the fracture toughness as a function of the loading force for the 1000 ppm Cr-doped UO_2. A polynomial fit of the fourth order (solid green line) was added to the data points. The green dashed line is the average fracture toughness value for the last four data points.

6.3.3. Comparison to Standard UO_2

In order to assess the quality of the synthesis method and compare it to a standard material, the microhardness and fracture toughness for the undoped UO_2 pellet was calculated. The results of the seven indentations are shown in Figure 67. The obtained microhardness of 6.74(8) GPa and fracture toughness of 1.41(7) $MPa.m^{0.5}$ are comparable to those of undoped UO_2 pellets made before in this research institute with a microhardness of 6.7(2) GPa and fracture toughness of 1.37(4) $MPa.m^{0.5}$ before annealing, and a microhardness of 6.1(1) GPa after annealing. The results from literature are comparable to the values after annealing of the institute's UO_2, while values before annealing are not presented [75, 92].

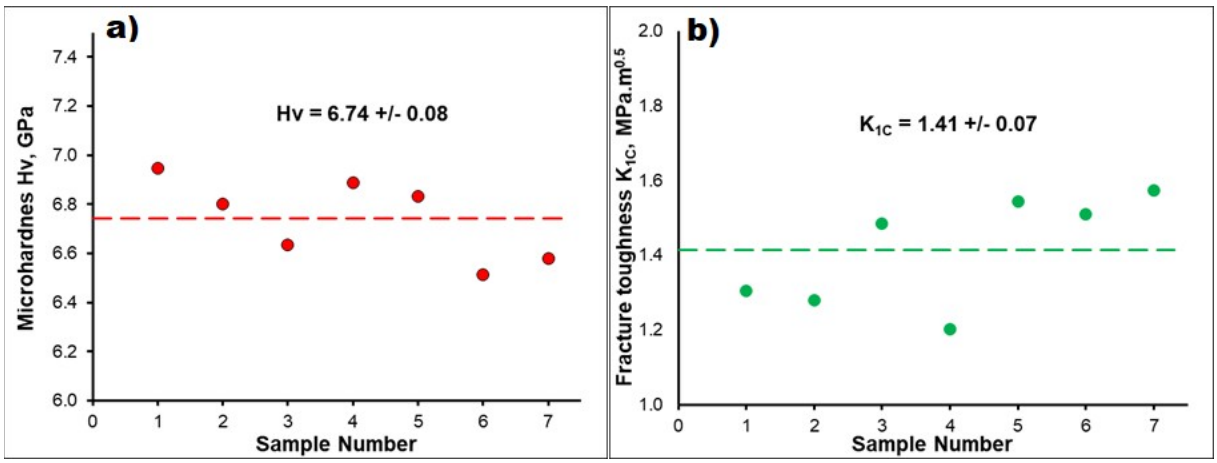

Figure 67 – Graph of the results of (a) microhardness and (b) fracture toughness measurements on seven points of the undoped UO_2 pellet. The dashed lines in both images represent the average value of the property.

6.3.4. Study of sample results

Looking at the results of microhardness measurements as a function of pellet density, shown in Figure 68, the Cr-doped UO_2 pellets reach a higher microhardness up to around 7.5 GPa but comparably lower densities. For the Al-doped UO_2 pellets all four data points are in a similar region, indicating that the effect of the aluminium addition is beyond a saturation point and despite the increase in density, microhardness is unaffected. For the Al/Cr-doped UO_2 pellets, microhardness is not increased, but a higher density is achieved. The point for the 1000 ppm Al/Cr-doped UO_2 pellets stands as an outlier, with a microhardness comparable to the Cr-doped UO_2 pellets.

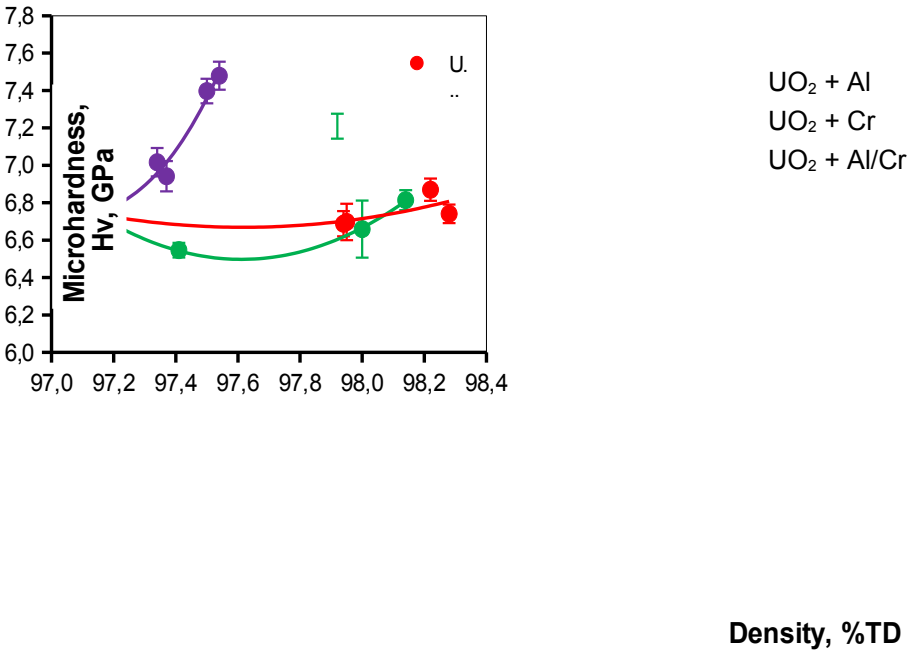

Figure 68 – Graph of the microhardness of Al-doped (red), Al/Cr-doped (green) and Cr-doped (purple) UO_2 as a function of pellet density. Second order polynomial fits were added to show the overall tendency. The empty green dot was an outlier value for the 1000 ppm Al/Cr-doped UO_2 with a very high value of microhardness.

Looking at the results of fracture toughness measurements as a function of pellet density, shown in Figure 69, with increasing density of the Cr-doped UO_2 pellets a decreasing value of fracture toughness is observed, which is correlated with the formation of longer cracks in the material under stress. For the Al-doped UO_2 pellets all four data points are in a similar region, indicating that the effect of the aluminium addition is beyond a saturation point. A reduction of the fracture toughness is observed compared to the undoped UO_2, but it less pronounced than for the Cr-doped UO_2 pellets. For the Al/Cr-doped UO_2 pellets the fracture toughness is lower than for the Al-doped UO_2 pellets, but higher than for the Cr-doped UO_2 pellets.

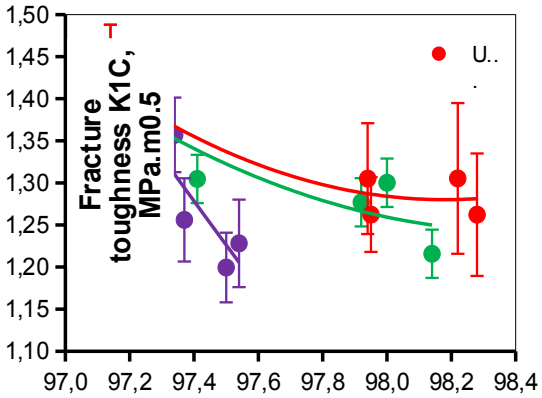

Figure 69 – Graph of the fracture toughness of Al-doped (red), Al/Cr-doped (green) and Cr-doped (purple) UO_2 as a function of pellet density. Second order polynomial fits were added to show the overall tendency.

Looking at the results of the microhardness measurements as a function of the amount of added dopant, shown in Figure 70, for the Cr-doped UO_2 pellets the microhardness increases up to the 1500 ppm added dopant, but decreases for the 2000 ppm addition. For the Al-doped UO_2 pellets practically no increase in microhardness is observed. For the Al/Cr-doped UO_2 pellets no increase in microhardness is observed, except for the 1000 ppm addition which shows a microhardness similar to the Cr-doped UO_2 pellets.

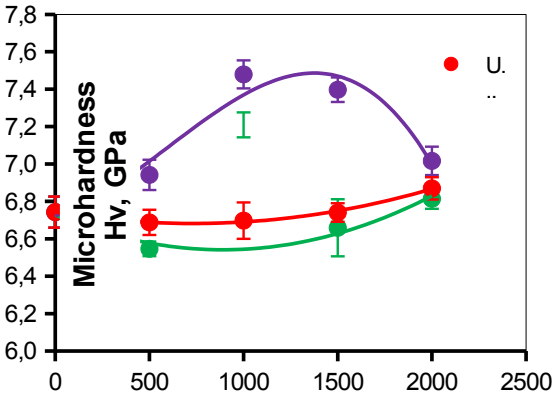

Figure 70 – Graph of the microhardness of Al-doped (red), Al/Cr-doped (green) and Cr-doped (purple) UO_2 as a function of dopant content in molar ppm. Second order polynomial fits were added to show the overall tendency. The empty green dot is an outlier value for the 1000 ppm Al/Cr-doped UO_2 with a very high value of microhardness.

Looking at the results of the fracture toughness measurements as a function of the amount of added dopant, shown in Figure 71, for the Cr-doped UO_2 pellets a decrease of the fracture toughness is observed up to the 1500 ppm addition, but this effect is reversed for the 2000 ppm addition. For the Al-doped UO_2 pellets the fracture toughness is lower than for the undoped UO_2 but does not change significantly with further addition of aluminium. For the Al/Cr-doped UO_2 pellets a similar reduction in the fracture toughness is observed up to the 1500 ppm addition, compared to the Al-doped UO_2 pellets. However, for the 2000 ppm Al/Cr addition a further drop in the fracture toughness is observed, indicating higher brittleness.

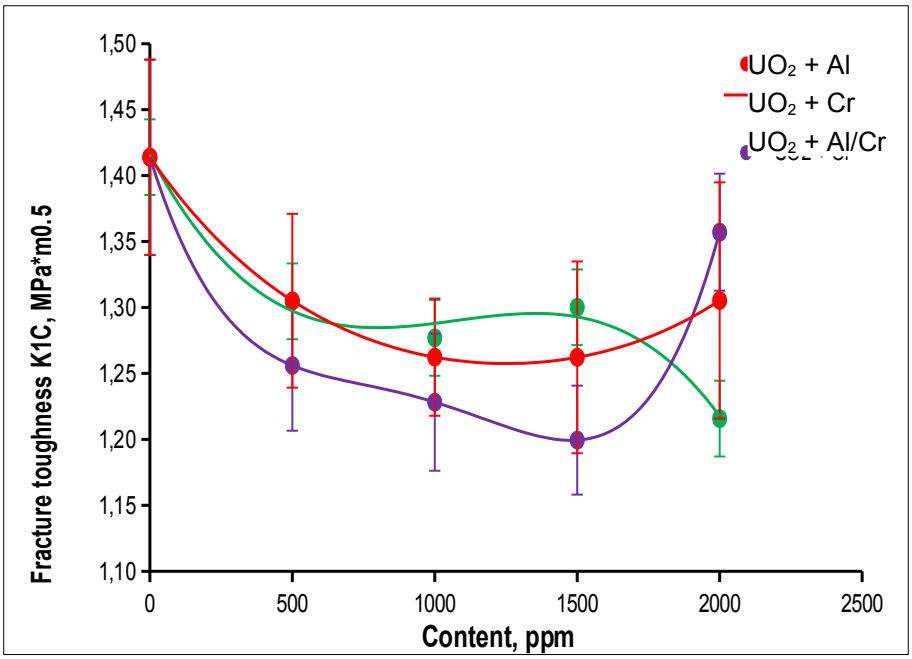

Figure 71 – Graph of the fracture toughness of Al-doped (red), Al/Cr-doped (green) and Cr-doped (purple) UO_2 as a function of dopant content in molar ppm. Second order polynomial fits were added to show the overall tendency.

6.4. Discussion

The addition of Al-doping to UO_2 pellets yielded densities up to 98.3% of the TD, however this effect seems to be limited to an addition of 1500 molar ppm which is consistent with its low solubility in the UO_2 matrix [67], showing a saturation effect where addition of more Al does not bring additional benefits. The addition of Al/Cr-doping to UO_2 pellets yielded densities up to 98.1% of the TD with the maximum effect at the 1000 ppm and 2000 ppm addition. Al/Cr can form a eutectic which can aid grain growth, for this an addition above the solubility limit and accounting for losses due to volatilization is needed [63]. Finally, for the Cr-doped UO_2 pellets a density maximum of 97.5% of the TD is achieved in the 1000-1500 ppm region and then for the 2000 ppm addition the density goes down to 97.3%, that is in agreement with literature that states the optimal additions of Cr are either around 700 wt. ppm or above 2000 wt. ppm of Cr_2O_3, our 2000

molar ppm Cr-doped UO_2 is equivalent to 564 wt. ppm and is below the solubility limit [64].

The evolution of the mechanical properties of the Al-doped UO_2 pellets with increasing dopant show that at 500 ppm the effects achieve saturation. Further addition of aluminium does not affect the final mechanical properties, which is consistent with literature and the absence of an eutectic phase for pure Al [67]. They have similar microhardness to the undoped UO_2, but lower fracture toughness indicating a more brittle material. The Al/Cr-doped UO_2 pellets show some surprising results, the 1000 ppm addition of Al/Cr presents the highest microhardness of any Al-doped pellet in this study, similar to the 1000 ppm Cr-doped pellet; while the 2000 ppm addition of Al/Cr presents a much lower fracture toughness than the Al-doped UO_2 pellets, indicating a more brittle material. Finally, the Cr-doped UO_2 pellets' microhardness and fracture toughness follow a similar trend to the results of the density, at 1000 ppm and 1500 ppm of addition of Cr we have a higher microhardness and lower fracture toughness, but then at 2000 ppm the trend is reversed and its properties are closer to that of undoped UO_2 with lower microhardness and higher fracture toughness. The pellets with Cr-doping here are below the solubility limit, which explains this behaviour with more variation, these findings are also in agreement with the results of microstructural analysis of the previous chapter. The effects of the addition of dopants above or below saturation is critical for the final properties of UO_2 based fuels and for the planning for the final disposal of SNF. Being above saturation confers the fuel the beneficial effect of the addition of dopants [93].

7. Conclusion and Outlook

To conclude, the accelerated transition towards carbon neutral economies with the need for base-load certain sovereign-controlled energy has reinvigorated interest in nuclear energy, transpiring in the development of ATF fuels. These fuels possess significant advantages through doping of the UO_2 with elements such as Cr and Al, but a significant paucity of information remains regarding their preparation, chemical properties, microstructure and mechanical properties.

To this end, this Master Thesis research has focused on developing a method for production and on studying Al-, Al/Cr- and Cr-doped UO_2 model materials. In particular, a method for the synthesis and systematic comparison of Al-, Al/Cr- and Cr-doped UO_2 ceramics was developed that could be carried out in laboratory scale and with high yield. The materials were of good quality, high density and with a single UO_2 phase present. Samples with identical molar metal fractions were produced in order to compare the effects of these dopants, concentrations of 500, 1000, 1500 and 2000 molar ppm were used.

The dopant and structural interaction chemistry of the addition of Cr, Al and Al/Cr to the cubic UO_2 $Fm\bar{3}m$ phase was investigated through P-XRD analysis. Quantification of their incorporation through the lattice contraction effect was found through the Rietveld refinement method and the results are consistent with the ionic radius of Al^{3+} and Cr^{3+} as well as with the limited solubility limits due to the small size of these ions compared to U^{4+} [59, 64, 66, 67, 77, 78]. Further investigations with synchrotron XRD could more precisely determine their incorporation in the UO_2 matrix.

The effect of Al, Cr and Al/Cr addition to the microstructure of UO_2 was investigated. Al-doping alone generated impressive results in grain size, despite its limited solubility is limited in the UO_2 matrix. Furthermore, it was shown that at higher doping amounts the higher volatility of Al_2O_3 compared to Cr_2O_3 affected the properties of the pellets at the rim. In particular, Al/Cr-doping presented increased grains in the centre, but an even stronger effect of volatility. The 2000 ppm Al/Cr-doped pellets presented a prominent decrease in grain size and the appearance of cracks at the rim of the pellet. In comparison, the examined 2000 ppm Cr-doped UO_2 pellet showed a modest grain size increase compared to the reference undoped UO_2 material, but no visible difference was observed at the rim. It is likely that higher concentrations of Cr are needed to achieve the enhanced grain sizes found in literature.

The addition of Cr, Al and Al/Cr dopants to UO_2 were shown to impact the final mechanical properties of the pellets. The amounts of added dopant are too small to affect the mechanical properties of the UO_2 directly and their effect here is rather due to

different behaviour during sintering changing grain size, formation of cracks and intergranular

structures like pores. All dopants increased the final sintered density of the pellets, and this effect was accompanied by an increase in brittleness. Al-doped UO_2 materials exhibited consistent microhardness and relatively higher fracture toughness then Al/Cr-doped UO_2. In contrast Cr-doped UO_2 presented variable fracture toughness and microhardness due to the materials not being at or above complete dopant saturation, unlike the Al and Al/Cr. Consequently, the mechanical properties highlight the importance of considering solubility of dopants and their relative amounts for addition to achieve the desired final mechanical properties. These results are of consequence for ADOPT™ and PROtect fuels, the effect of Al-doping being diminished at the rim of pellets due to higher volatility, leading to smaller grains on the rim of pellets. These smaller grains at the rim provide a short diffusion path contributing greatly to FGR, as the rim is where most of the fission occurs, it also increases the specific surface available for reaction and dissolution by water in SNF conditions. It also of note the higher amounts of Cr doping needed to achieve enhanced grain growth effects by eutectic phase formation.

To sum up, the chemical, microstructural and mechanical properties of Cr, Al and Al/Cr doped UO_2 materials were investigated leading to an enhanced understanding of their performance as ATF fuels and eventually SNF.

8. References

1. NEA, *Technical and Economic Aspects of Load Following with Nuclear Power Plants*. 2011, OECD Publishing: Paris.
2. Loisel, R., et al., *Load-following with nuclear power: Market effects and welfare implications.* Progress in Nuclear Energy, 2018. **109**: p. 280-292.
3. Commission, U.S.A.E., *The first reactor*. Understanding the atom. 1967, [Oak Ridge, Tennessee]: U.S. Atomic Energy Commission, Division of Technical Information.
4. Association, W.N. *RBMK Reactors – Appendix to Nuclear Power Reactors*. 2022; Available from: https://world-nuclear.org/information-library/appendices/rbmk-reactors.
5. Holbert, K.E. *A Review of Maritime Nuclear Reactor Systems*. Journal of Nuclear Engineering, 2025. **6**, DOI: 10.3390/jne6010005.
6. Meredith, S., *Spain's unprecedented power outage sparks a blackout blame game over green energy*, in *CNBC*. 2025: Internet.
7. *Nuclear Share of Electricity Generation - 2024*, IAEA, Editor. 2024.
8. IEA, *World Energy Outlook 2023*. 2023, IEA: Paris.
9. Association, W.N., *World Nuclear Performance Report 2023: Report No. 2023/001*. 2023, World Nuclear Association.
10. Annika Breidthardt, A.R.a.H.-E.B., *German govt wants nuclear exit by 2022 at latest*, in *Reuters*. 2011: Internet.
11. *Switzerland moves to remove ban on new reactors*, in *World Nuclear News*. 2024: Internet.
12. *Belgium reverses nuclear phase-out plans*, in *Nuclear Engineering International*. 2025: Internet.
13. Broomby, R., *France struggles to cut down on nuclear power*, in *BBC*. 2014: Internet.
14. Tiezzi, S., *Why China Will Go All-In on Nuclear Power*, in *The Diplomat*. 2014: Internet.
15. IAEA, *IAEA Action Plan on Nuclear Safety*. 2011.
16. Evdokimov, I.A., et al., *Detection of fuel washout from leaking fuel rods during operation of WWER power units.* Journal of Nuclear Materials, 2020. **538**: p. 152205.
17. Rest, J., et al., *Fission gas release from UO_2 nuclear fuel: A review.* Journal of Nuclear Materials, 2019. **513**: p. 310-345.
18. Qi, F., et al., *Pellet-cladding mechanical interaction analysis of Cr-coated Zircaloy cladding.* Nuclear Engineering and Design, 2020. **367**: p. 110792.

19. Johnson, J., et al., *The Technology of Uranium Dioxide--A Reactor Material*. 1956, Oak Ridge National Lab.(ORNL), Oak Ridge, TN (United States).
20. Brandberg, S.G., *The Conversion of Uranium Hexafluoride to Uranium Dioxide.* Nuclear Technology, 1973. **18**(2): p. 177-184.
21. Momma, K. and F. Izumi, *VESTA 3 for three-dimensional visualization of crystal, volumetric and morphology data.* Journal of Applied Crystallography, 2011. **44**(6): p. 1272-1276.
22. NRC, U., *The Nuclear Fuel Cycle*. 2019.
23. Plöger, F. and H. Vietzke, *Gewinnung von Kernbrennstoffen. Teil 2: Angereichertes Uran.* Chemie Ingenieur Technik, 1965. **37**(7): p. 692–699.
24. Knudsen, I.E., H.E. Hootman, and N.M. Levitz, *A Fluid-Bed Process for the Direct Conversion of Uranium Hexafluoride to Uranium Dioxide.* Nuclear Science and Engineering, 1964. **20**(3): p. 259–265.
25. Nishijima, T., T. Kawada, and H. Kitagawa, *An improved process for fabricating UO_2 pellets.* Journal of Nuclear Materials, 1965. **16**(2): p. 184-189.
26. Radford, K.C., *Effect of fabrication parameters and microstructure on the mechanical strength of UO_2 fuel pellets.* Journal of Nuclear Materials, 1979. **84**(1): p. 222-236.
27. Bukaemskiy, A.A., D. Barrier, and G. Modolo, *Compressibility and sinterability of CeO_2–8YSZ powders synthesized by a wet chemical method.* Journal of the European Ceramic Society, 2009. **29**(10): p. 1947–1954.
28. Center, N.D., *Graph of Fission Product Yields*, J.A.E. Agency, Editor. 2023.
29. Billard, I., *Spent fuel composition*. Internet. p. Distribution (in kg per ton of fuel) and mass produced by the principal radioactive elements present in fuel unloaded from an pressurised water reactor core.
30. Shigeaki Okajima, T.K., Takamasa Mori, *Nuclear Reactor Physics*. 2024: Springer Tokyo. X, 316.
31. Oudinet, G., et al., *Characterization of plutonium distribution in MIMAS MOX by image analysis.* Journal of Nuclear Materials, 2008. **375**(1): p. 86-94.
32. Bairiot, H. and P. Deramaix, *MOX fuel development: yesterday, today and tomorrow.* Journal of Nuclear Materials, 1992. **188**: p. 10-18.
33. Bernard-Granger, G., et al., *Comparative sintering behaviour of MOX powders synthesized through the freeze granulation or dry-cogrinding routes.* Journal of the European Ceramic Society, 2024. **44**(12): p. 7224-7235.
34. Serrano, J.A., et al., *Influence of low temperature air oxidation on the dissolution behaviour of UO_2 and MOX spent fuel.* Journal of Alloys and Compounds, 1998. **271-273**: p. 573-576.
35. *Das Forschungsprogramm der BGZ*. 2023: BGZ Gesellschaft für Zwischenlagerung mbH.

36. Tsvekov, P.V., *Nuclear Power - Deployment, Operation and Sustainability*. 2011, Rijeka, Croatia: InTech.
37. Powers, J.J. and B.D. Wirth, *A review of TRISO fuel performance models.* Journal of Nuclear Materials, 2010. **405**(1): p. 74-82.
38. Pohl, P. and J.G. AVR GmbH, *The Importance of the AVR Pebble-Bed Reactor For the Future of Nuclear Power*. 2007.
39. Bruna, G., et al., *Overview of Generation IV (Gen IV) Reactor Designs - Safety and Radiological Protection Considerations*. 2012.
40. Mistarihi, Q., et al., *Fabrication and thermal conductivity of UN-UB2 composites fabricated by spark plasma sintering.* Journal of Nuclear Materials, 2023. **587**: p. 154738.
41. Harding, J.H. and D.G. Martin, *A recommendation for the thermal conductivity of UO_2.* Journal of Nuclear Materials, 1989. **166**(3): p. 223-226.
42. Setyadji, M. and A. Fitrotun, *Characteristics of Uranium Dioxide (UO_2) Kernel Produced by Sintering Process using Modified Sintering Reactor.* IOP Conference Series: Materials Science and Engineering, 2019. **553**(1): p. 012040.
43. Ekberg, C., et al., *Nitride fuel for Gen IV nuclear power systems.* Journal of Radioanalytical and Nuclear Chemistry, 2018. **318**(3): p. 1713-1725.
44. Ding, X.-C., et al., *High enrichment of ^{15}N isotope by ion exchange for nitride fuel development.* Progress in Nuclear Energy, 2008. **50**(2): p. 504-509.
45. Yun, D., et al., *Current state and prospect on the development of advanced nuclear fuel system materials: A review.* Materials Reports: Energy, 2021. **1**(1): p. 100007.
46. Kegler, P., et al., *Chromium Doped UO_2-Based Ceramics: Synthesis and Characterization of Model Materials for Modern Nuclear Fuels.* Materials (Basel, Switzerland), 2021. **14**(20).
47. Paulson, W.A., Springborn, Roy H., *Estimate of Fission-Product Gas Pressure in Uranium Dioxide Ceramic Fuel Elements*, L.R. Center, Editor. 1968: Washington, D.C.
48. Ge, Z., et al. *A Comprehensive Review of High Burn-Up Structure Formation in UO_2: Mechanisms, Interactions, and Future Directions*. Nanomaterials, 2025. **15**, DOI: 10.3390/nano15050325.
49. Murphy, G.L., et al., *Deconvoluting Cr states in Cr-doped UO2 nuclear fuels via bulk and single crystal spectroscopic studies.* Nature Communications, 2023. **14**(1): p. 2455.
50. *These Accident Tolerant Fuels Could Boost the Performance of Today's Reactors: Three of the largest U.S. nuclear suppliers are working with the Energy Department to develop new accident tolerant fuels for the nation's reactors*. Office of Nuclear Energy.

51. Crede, T.M., et al., *Advanced Doped Pellet Technology (ADOPT) Fuel*. 2022, Westinghouse.
52. *Westinghouse Produces First Batch of Higher Enriched Fuel Pellets: Westinghouse Electric Company has produced new fuel pellets that contain higher enrichment levels than what is currently used in commercial reactors*. Office of Nuclear Energy.
53. Framatome, *Framatome's PROtect Accident Tolerant Fuel reaches New Operational Milestone at Gösgen Nuclear Power Plant in Switzerland*. 2024, Framatome.
54. Killeen, J.C., *Fission gas release and swelling in UO_2 doped with Cr_2O_3.* Journal of Nuclear Materials, 1980. **88**(2): p. 177-184.
55. Matzke, H., *On uranium self-diffusion in UO_2 and UO_{2+x}.* Journal of Nuclear Materials, 1969. **30**(1): p. 26-35.
56. ARBORELIUS, J., et al., *Advanced Doped UO_2 Pellets in LWR Applications.* Journal of Nuclear Science and Technology, 2006. **43**(9): p. 967–976.
57. *The U.S. Accident Tolerant Fuels Program — Update on a National Initiative*. 2021. United States.
58. Murphy, G.L., et al., *The role of redox and structure on grain growth in Mn-doped UO_2.* Communications Materials, 2024. **5**(1).
59. Bourgeois, L., et al., *Factors governing microstructure development of Cr_2O_3-doped UO_2 during sintering.* Journal of Nuclear Materials, 2001. **297**(3): p. 313–326.
60. Cardinaels, T., et al., *Chromia Doped Uo_2 Fuel: Investigation Of The Lattice Parameter.* Journal of Nuclear Materials, 2012. **424**(1): p. 252-260.
61. Riglet-Martial, C., et al., *Thermodynamics of chromium in UO_2 fuel: A solubility model.* Journal of Nuclear Materials, 2014. **447**(1-3): p. 63–72.
62. Guthrie, F., *LII. On eutexia.* The London, Edinburgh, and Dublin Philosophical Magazine and Journal of Science, 1884. **17**(108): p. 462–482.
63. Degterov, S. and A.D. Pelton, *Critical evaluation and optimization of the thermodynamic properties and phase diagrams of the CrO-Cr_2O_3, CrO-Cr_2O_3-Al_2O_3, and CrO-Cr_2O_3-CaO systems.* Journal of Phase Equilibria, 1996. **17**(6): p. 476-487.
64. Leenaers, A., et al., *On The Solubility Of Chromium Sesquioxide In Uranium Dioxide Fuel.* Journal of Nuclear Materials, 2003. **317**(1): p. 62-68.
65. Peres, V., et al., *High temperature chromium volatilization from Cr_2O_3 powder and Cr_2O_3-doped UO_2 pellets in reducing atmospheres.* Journal of Nuclear Materials, 2012. **423**(1-3): p. 93–101.
66. Bourgeois, L., *Contribution à l'étude du rôle de dopants dans la densification et la croissance cristalline du dioxyde d'uranium*. 1992. p. 1 volume (144 pages).

67. Kim, D., et al., *Effect of small amounts of aluminium doping on the grain growth of a UO_2 pellet.* Trans. Korean Nucl. Soc. Spring Meet., 2006.
68. Murphy, G.L., et al., *A synchrotron X-ray diffraction and electron microscopy study of vanadium-doped UO2.* MRS Advances, 2025.
69. Vegard, L., *Die Konstitution der Mischkristalle und die Raumfüllung der Atome.* Zeitschrift für Physik, 1921. **5**(1): p. 17-26.
70. Cullity, B.D., *Elements of X-Ray Diffraction*. 1978, London: Addison-Wesley Publishing Company, Inc.
71. Hewat, A., W.I.F. David, and L. van Eijck, *Hugo Rietveld (1932-2016).* Journal of Applied Crystallography, 2016. **49**(4): p. 1394-1395.
72. Rietveld, H., *A profile refinement method for nuclear and magnetic structures.* Journal of Applied Crystallography, 1969. **2**(2): p. 65-71.
73. Toby, B.H., & Von Dreele, R. B., *GSAS-II: the genesis of a modern open-source all purpose crystallography software package.* Journal of Applied Crystallography, 2013. **46(2)**: p. 544-549.
74. Claudionico~commonswiki, *Electron Interaction with Matter*, E.I.w. Matter.svg, Editor. 2013: Wikimedia Commons.
75. Novikov, V.V., et al., *Fracture Toughness of VVER and PWR Uranium-Dioxide Fuel Pellets with Different Grain Size.* Atomic Energy, 2015. **118**(2): p. 117-123.
76. Murphy, G.L., et al., *The lattice contraction of UO2 from Cr doping as determined via high resolution synchrotron X-ray powder diffraction.* Journal of Nuclear Materials, 2024. **595**: p. 155046.
77. Shannon, R.D. and C.T. Prewitt, *Effective ionic radii and crystal chemistry.* Journal of Inorganic and Nuclear Chemistry, 1970. **32**(5): p. 1427-1441.
78. Shannon, R.t. and C. Prewitt, *Revised values of effective ionic radii.* Structural Science, 1970. **26**(7): p. 1046-1048.
79. Leinders, G., et al., *Accurate lattice parameter measurements of stoichiometric uranium dioxide.* Journal of Nuclear Materials, 2015. **459**: p. 135-142.
80. Desgranges, L., et al., *Refinement of the α-U_4O_9 Crystalline Structure: New Insight into the U_4O_9 → U_3O_8 Transformation.* Inorganic Chemistry, 2011. **50**(13): p. 6146-6151.
81. Willis, B., *The defect structure of hyper-stoichiometric uranium dioxide.* Acta Crystallographica Section A, 1978. **34**(1): p. 88-90.
82. Zhang, L., et al., *A combined calorimetric and computational study of the energetics of rare earth substituted UO2 systems.* Acta Materialia, 2015. **97**: p. 191-198.
83. Solomon, J.M., et al., *Computational study of the energetics and defect clustering tendencies for Y- and La-doped UO_2.* Acta Materialia, 2014. **78**: p. 282-289.

84. Butorin, S.M., et al., *Characteristics of chemical bonding of pentavalent uranium in La-doped UO_2.* Chemical Communications, 2016. **53**(1): p. 115-118.

85. Prieur, D., et al., *Aliovalent Cation Substitution in UO_2: Electronic and Local Structures of $U_{1-y}La_yO_{2\pm x}$ Solid Solutions.* Inorganic Chemistry, 2018. **57**(3): p. 1535-1544.

86. Shannon, R.D. and C.T. Prewitt, *Effective ionic radii in oxides and fluorides.* Acta Crystallographica Section B, 1969. **25**(5): p. 925-946.

87. Ohmichi, T., et al., *On the relation between lattice parameter and O/M ratio for uranium dioxide-trivalent rare earth oxide solid solution.* Journal of Nuclear Materials, 1981. **102**(1): p. 40-46.

88. Patnaik, P., *Handbook of inorganic chemicals*. Vol. 529. 2003: McGraw-Hill New York.

89. Niihara, K., R. Morena, and D.P.H. Hasselman, *Evaluation of K_{IC} of brittle solids by the indentation method with low crack-to-indent ratios.* Journal of Materials Science Letters, 1982. **1**(1): p. 13-16.

90. Yamada, K., et al., *Study of the thermodynamic properties of (U, Ce)O_2.* Journal of Nuclear Materials, 1997. **247**: p. 289-292.

91. Sangwal, K., *Review: Indentation size effect, indentation cracks and microhardness measurement of brittle crystalline solids – some basic concepts and trends.* Crystal Research and Technology, 2009. **44**(10): p. 1019-1037.

92. Yamada, K., S. Yamanaka, and M. Katsura, *Mechanical properties of (U,Ce)O_2.* Journal of Alloys and Compounds, 1998. **271-273**: p. 697-701.

93. Zacharie-Aubrun, I., et al., *Effects of irradiation on mechanical properties of nuclear UO_2 fuels evaluated by Vickers indentation at room temperature.* Journal of Nuclear Materials, 2021. **547**: p. 152821.